2010

Research Experience for Undergraduates Program, 2010

University of Arkansas, Fayetteville. Dept. of Chemistry and Biochemistry

Research Experience for Undergraduates 2010

Department of Chemistry and Biochemistry
University of Arkansas

David W. Paul – Julie Stenken
Program Co-Directors

Supported by the National Science Foundation

Table of Contents

Research Experience for Undergraduates
University of Arkansas

The University of Arkansas Department of Chemistry and Biochemistry hosted a National Science Foundation sponsored Research Experience for Undergraduates (REU) summer program for the 21st year. The department first hosted an REU in 1959. The 10-week summer program, funded by the National Science Foundation, allowed students an opportunity to gain hands-on experience in a chosen research area while introducing them to careers in scientific research in areas including analytical chemistry and sensor technology, biochemistry and protein dynamics, inorganic chemistry and nanotechnology, organic chemistry, and physical and theoretical chemistry.

Undergraduate chemistry majors, who were sophomores or juniors in fall 2009, applied to the program, which took place in the Ozark Mountain Plateau.

Outside the lab, students met each week to hear presentations from campus experts about topics ranging from how to get into graduate school and test-taking skills to ethics, and how to make a poster presentation. A number of social activities took place throughout the summer to give students a chance to interact.

Selected students received a scholarship to pay for room and board and an allowance to attend a regional or national chemical conference in the 2010-2011 academic year. Students involved in the program were enrolled as students at the U of A and received one hour of research credit. The program was conducted from May 16, 2009 to July 23, 2009.

Tony Jude Award

Arkansas native Vernon (D.J.) Crowell was the recipient of the Tony Jude Award for his summer research. He is a student at Lyon College. The Tony Judy Award was created in 2002 to recognize a student for outstanding research. It is awarded in memory of a former REU student who returned to the University of Arkansas and obtained a doctorate degree.

D.J., under the direction of Distinguished Professor Peter Pulay, presented a poster entitled “Computer Modeling of the Thermal Rearrangement of 2-aryl-2H-azirines to Indoles.”

He is pictured below with Distinguished Professor Peter Pulay and Program Co-Director Professor David Paul.

2010 REU Participants

Eric Berget
Minnesota State University
Hometown: Detroit Lakes, Minn.
Mentor – Charles Wilkins

Jean-Marie Charles
Cameron University
Hometown: Roseau, Dominica
Mentor – Nan Zheng

D.J. Crowell
Lyon College
Hometown: Wynne
Mentor – Peter Pulay

Anna Fielder
University of Arkansas
Hometown: Fayetteville
Mentor – Bob Gawley

Rebecca Foos
John Brown University
Hometown: Fort Collins, Colo.
Mentor – Matt McIntosh

Amanda Hicks
John Brown University
Hometown: Manitou Springs, Colo.
Mentor – Ingrid Fritsch

Jared Kafader
Elmhurst College
Hometown: Mt. Prospect, Ill.
Mentor – Roger Koeppe

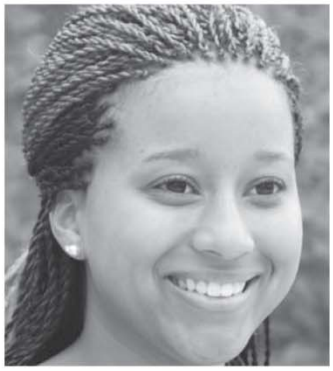

Erika Russell
Bethune-Cookman University
Hometown: Grand Rapids, Mich.
Mentor – Paul Adams

Maria Williams
Texas Southern University
Hometown: Baton Rouge, La.
Mentor – Frank Millett
** George Washington Carver intern*

Faculty Project List

Paul Adams *Assistant Professor*	Biophysical Characterization of Proteins Associated with Signal Transduction
Neil Allison *Associate Professor and Vice-Chair*	Synthesis and Chemistry of Potential Organometallic Anticancer Drugs
Dan Davis *Professor*	Protein-Protein Interactions in Phogosynthesis: Structure-Function Relationships in Electron Transfer Proteins
Ingrid Fritsch *Professor*	Microelectrochemical Detection and Microfluidics for Lab-on-a-chip Applications: Protein, DNA, and Microorganism Analysis
Bob Gawley *Distinguished Professor*	Synthetic and Mechanistic Organ(ometall)ic Chemistry
Denise Greathouse *Research Assistant Professor*	Characterization of Structure and Peptide-Lipid Interactions of Membrane Active Antimicrobial Peptides
Colin Heyes *Assistant Professor*	Development of Nanocrystals for Biophysical Applications
Roger Koeppe *University Professor*	Biophysical Studies of Single-Span Transmembrane Proteins and Membrane Channel Gating
T.K.S. Kumar *Assistant Professor*	Structure, Dynamics, Folding and Interactions of Proteins
Matt McIntosh *Associate Professor*	Total Synthesis of Biomedically Significant Complex Natural Products
Frank Millett *Distinguished Professor*	Biological Electron Transfer
David Paul *Associate Professor*	Development of chemical Sensors for Clinical and Environmental Applications
Peter Pulay *Distinguished Professor*	Ab initio Calculation of the Vibrational and NMR Spectra of Protein Models
Joshua Sakon *Associate Professor*	Structure and Function of Drug-Targets
Derek Sears *University Professor*	Cosmochemistry

Julie Stenken *Professor*	Measurement of chemical Communication (Signaling) Molecules, e.g., Cytokines, Neuropeptides, etc., Biosensors, or In Vivo Chemical Analysis
Wesley Stites *Professor*	Exploring the Influence of the Denatured State upon Protein Stability, -or- Isolation, Characterization, and Impact upon Blood Clotting of Human Thrombomodulin in Disease
Z. Ryan Tian *Assistant Professor*	Syntheses and Applications of Ordered and Complex Nanostructures
Charles Wilkins *Distinguished Professor*	Matrix-assisted Laser Desorption Fourier Transform Mass Spectrometry for Whole-cell Bacteria and Polymer Analysis
Nan Zheng *Assistant Professor*	Natural Product Synthesis, Metod Development, and Organometallics

UNIVERSITY OF ARKANSAS
NSF – CHEMISTRY – REU - SUMMER 2010
Activities and Events

Sunday, May 16

1:00 p.m. – 4:00 p.m. **Arrival, Check-In & Registration**
Maple Hill West (front desk: (479)718-2590)

6:00 p.m. – 9:00 p.m. **Welcome Dinner**
University House, Whole Hog Barbeque

Monday, May 17

7:00 a.m. – 8:30 a.m. **Breakfast**
Quad Dining Room

8:45 a.m. Meet in quad lobby to go to university together

9:00 a.m. – 10:00 a.m. **Group Photo**
Front of Library

9:45 a.m. – 11:45 a.m. **Campus Logistics** (Concurrent Sessions)

RED	**Session I:**	**9:45-10:30 a.m.**	**Session II:**	**10:45-11:30 a.m.**	**(Carver & MEEG)**
YELLOW	**Session II:**	**9:45-10:30 a.m.**	**Session I:**	**10:45-11:30 a.m.**	**(CHEM, Phys, & Food Sci)**

Session I: **Cash Checks, ID Cards Issued**
Arkansas Union
Parking and Transit available: $21.57 per parking tag.
May park in lot 41 (near Reid Hall) Monday. Tag needs to be displayed by Tuesday to avoid ticketing.

Session II: **Library Orientation**
University of Arkansas Mullins Library

12:00 p.m. - 1:30 p.m. **Opening Luncheon**
Place: Student Union Ballroom
Speaker: Dr. Donald Pederson, Vice Chancellor, Professor of Physics

1:30 p.m. – 2:30 p.m. **Campus Tour**
Meet in Ballroom with campus ambassadors

2:30 p.m. – 4:30 p.m. **Departmental Logistics**
Place: Chemistry Building Room 105
Meet your Mentor: Refreshments will be served
Get Keys, Take Photos

Tuesday, May 18

8:00 a.m. – 10:00 a.m. **Safety Briefing:** Bill Durham, Department Chair
CHEM 105

11:00 a.m. – 12:00 a.m. **CHEMISTRY Library Tour**
Place: MULLINS 102, moving to CHEM Library
Librarian: Luti Salisbury

12:00 noon **Go to Your Lab and Get Started!**

Wednesday, May 19

8:00 a.m. **Report to your lab**

5:30 p.m. – 7:00 p.m. **Dinner & Dialogue**
Place: Alumni House
Speaker: Dr. Dennis Brewer, Assoc. Vice Provost for Research
Topic: Research and Ethics

Friday, May 21 **REU Meeting**
1:00 p.m.
CHEM 105
Speaker: Professor Julie Stenken
Topic: Why is in vivo Glucose Sensing so Challenging?

Wednesday, May 26 **Dinner & Dialogue**
5:30 p.m. – 7:00 p.m.
Place: Donald W. Reynolds Center, Seminar Room A
Speaker: Dr. Collis Geren, Dean of the Graduate School
Topic: Little Brown Spider

Thursday, May 27 **Evening Entertainment**
6:00 p.m. – 9:00 p.m.
Host: Chemistry
Location: Devil's Den State Park (bring swim suit!)

Friday, May 28 **REU Meeting**
1:00 p.m.
CHEM 105
Speaker: Dr. Robert Gawley
Title: Why did Alice say to Kitty: "Perhaps looking glass milk isn't good to drink." A guided tour from Lineland to Spaceland.

Saturday, May 29– Monday May 31 Free for Memorial Day Weekend

Wednesday, June 2 **Dinner & Dialogue**
5:30 p.m. – 7:00 p.m.
Location: Alumni House
Speaker: Lynn Meade
Topic: How to Give an Effective Presentation

Thursday, June 3 — **Evening Entertainment**
6:00 p.m. – 9:00 p.m. **Host:** Carver
Location: Starlight Skatium

Friday, June 4 — **REU Meeting**
1:00 p.m. CHEM 105
Speaker: Dr. Paul Adams
Title: Protein Purification

Wednesday, June 9 — **Dinner & Dialogue**
5:30 p.m. – 7:00 p.m. **Place:** Donald W. Reynolds Center, Seminar Room A
Speaker: Dr. Alex Lostetter
Topic: Science Careers

Thursday, June 10 — **Evening Entertainment**
Host: Physics
Location: Movie Night

Friday, June 11 — **REU Meeting**
1:00 p.m. CHEM 105
Speaker: Professor Lothar Schäfer
Title: Science and Divine Reality

Monday, June 14 — **Canoe Trip**

Wednesday, June 16 — **Dinner & Dialogue**
5:30 p.m. – 7:00 p.m. **Place:** Donald W. Reynolds Center, Seminar Room A
Speaker: Shani Farr & Vicky Hartwell
Topic: Applying to Grad School and Funding your Graduate Degree

Thursday, June 17 — **Evening Entertainment**
6:00 p.m. – 9:00 p.m. **Host:** Mechanical Engineering
Location: Ozark Lanes

Friday, June 18 — **REU Meeting**
1:00 p.m. CHEM 105
Speaker: Prof. Jack Lay
Topic: Mass Spectrometry and Biomarkers

Saturday, June 19 — **Practice GRE and GMAT test offered**
10 a.m. Testing is FREE
Participation requires pre-registration
Location: Maple Hill South, Room 145

Thursday, June 24 **Evening Entertainment**
Host: Micro EP
Location: Veteran's Park, Lake Fayetteville

Friday, June 25 **REU Meeting**
1:00 p.m. CHEM 105
Half-way Progress Report Presentation
Progress Reports Due

Monday-Tuesday, June 28-29
NCTR Tour
Jefferson, AR
Overnight stay in Little Rock, Dinner w/ INBRE students

Friday, July 2 **REU Meeting**
1:00 p.m. CHEM 105
Speaker: Professor T.K.S. Kumar
Topic: The Biochemistry of Molecules that Sustain Life

Saturday, July 3 – Monday, July 5 **Free for Independence Day Weekend**
You **must** return to Fayetteville by 8:00 a.m., July 6

Wednesday, July 7 **Final Carver Presentations**
3:00p.m. – 7:00 p.m.

Friday, July 9 **REU Meeting**
1:00 p.m. CHEM 105
Speaker: Dr. Colin Heyes
Topic: Nanochemistry and biochemistry at the single molecule level

Friday, July 16 **REU Meeting**
1:00 p.m. Chem 105
How to Make a Poster
David Paul

Thursday, July 22 **Meeting in Miniature, Lunch Served**
10:00 a.m. CHEM 105

Friday, July 23 **End of Program**
5:00 p.m. Final reports due
Dorm check-out

Saturday, July 24 **End of Program**
By 11:00 a.m. Get out of the Dorm, last check-out

Analysis of [6,6]-phenyl C_{61} butyric acid methyl ester (PCBM) by FTMS

Eric Berget, Minnesota State University Moorhead
Moorhead, MN

Abstract

An analysis of [6,6]-phenyl C_{61} butyric acid methyl ester (PCBM) was conducted to determine the optimal characteristics for obtaining reference spectra with the least amount of fragmentation. The characteristics varied were matrix to analyte ratios, laser power influence, sample deposition methodology, and solvents used. The analysis of PCBM was also compared between two different ionization process, laser desorption ionization (LDI) and matrix assisted laser desorption ionization (MALDI). Following ionization the ions were analyzed by Fourier Transform Mass Spectrometry (FTMS). Electron transfer matrices dithranol and 9-nitranthracene were used in the analysis, in combination with the solvents chlorobenzene and toluene.

Introduction

The purpose of experimentation:

The fullerene PCBM is most notably used in combination with poly(3-hexylthiophene) (P3HT) for use in organic heterojuction photovoltaic cells (*1*,*2*). Due to the rising demand for energy, organic heterojuction photovoltaic cells are being explored as an alternative to the current silicon based solar cells. However, the PCBM/P3HT heterojuction cells undergo degradation when in service. Mass spectrometry could be used at set intervals of the degradation process to study the mass and ascertain the type of chemical reactions that are occurring and the resulting product. However, reference spectra must be obtained of the starting materials; so that the differences noticed in the degraded solar cells can be linked to the degradation process. The focus of this experiment is to obtain reference spectra for PCBM and determine the optimal parameters for its analysis by MALDI.

The ionization processes MALDI and LDI:

The analysis on PCBM was conducted using LDI and MALDI as the ionization process in combination with FTMS as the analyzer. The ionization process LDI consists of a laser striking an analyte on a target plate and causing ionization by departing energy on to it. The direct transfer of energy to the analyte and subsequent reactions in the ion plume cause ionization and fragmentation (*3*,*4*). The target plate is responsible for housing the sample to be studied and can be made of anything from stainless steel to Teflon (*5*). The ion plume is an area or “cloud” where ionization processes occur and other various reactions (*6*,*4*). The ion plume is an area of intense research and to date there are various theories, but no clear understanding of it (*6*).

The implementation of matrix in MALDI causes reduced fragmentation and an increased parent ion concentration in relation to LDI. MADLI is similar to LDI in that a laser strikes the analyte, but with a certain ratio of matrix mixed in. MALDI is the optimal soft ionization process for larger molecules due to large amounts of fragmentation with LDI. Smaller molecules, however, can be studied for the most part effectively using LDI which is considerably less time consuming in comparison to MALDI. The reason is because MADLI has many variables to

consider and to date no default matrix or solvent has been found (*7*). Therefore, several trail experiments must be done to obtain the best possible result. The known variables that can affect MALDI are the matrix to analyte ratio, solvent used, target plate material, laser type/power, and type of application process to the target plate (*5,3,4*).

However, unlike in LDI, the analyte does not receive all the blunt force of the transferred energy from the striking laser beam, and instead the energy is transferred to the matrix and subsequently to the analyte by a series of reactions. The type of ionization process that the analyte undergoes depends on the type of matrix that is employed (*3*). The analyte can be ionized by the addition of hydrogen, the removal of an electron, or the addition of an electron. The ionization process can happen at the surface by contact with the laser beam or through reactions in the ion plume.

Fourier Transform Mass Spectrometry:

Once the ionization process is complete the ions must be transferred to the mass analyzer which in this case is the FTMS. The ions can are transferred by means of ion guides (*3*). The ions are detected in the FTMS in what is called an ion cyclotron resonance (ICR) cell. The ions generate a cyclotron frequency as they orbit about the cell, which causes an image current to be generated (*3*). The image current is fleeting at one location and moves around the cell as the ions orbit inside (*3*). However, the image current can be detected and through a mathematical process called the Fourier Transform a mass spectrum can be generated that reflects that ion. Therefore, a typical mass spectrum that contains several different types of ions is actually the detection of several image currents and subsequent Fourier transforms. The lower detection limit of FTMS, however, still requires several thousand ions to hundreds of thousands of ions present to be detected and give an associated ion peak.

Choice of Matrices and Optimization of MALDI for PCBM Analysis:

The matrices used in the analysis of PCBM by MALDI-FTMS are dithranol and 9-nitroanthracene. Dithranol is a very commonly used matrix for the analysis of various compounds. However, 9-nitroanthracene is noted in the literature to be a highly effective matrix for use in the MALDI ionization process; for the analysis of fullerene compounds such as PCBM (*8,9,10*). The matrices and analyte were made in toluene and chlorobenzene at the following molar matrix to analyte ratios: 5000:1, 2000:1, 1000:1, 750:1, 500:1, and 250:1. Dithranol and 9-nitroanthracene were compared and contrasted amongst the varying molar matrix to analyte ratios and against the application process of the sample to the target plate. Two application processes were used, the dry droplet technique and the aerospray technique. In addition, LDI spectra of PCBM in toluene and chlorobenzene were also acquired and compared against spectra acquired by MALDI. The relative laser power was varied and the influence of the laser was optimized for obtaining the best possible spectra.

Experimental

Materials:

9.4T Bruker Ultraflex FTMS
Nd:YAG Laser (355nm)
9-nitroanthracene, 95%, Aldrich, CAS# 602-60-8
1,8,9-trihydroxyantracene (dithranol), 97%, Alfa Aesar, CAS# 1143-38-0

α-cyano-4-hydroxycinnamic acid (CHCA), CAS# 28166-41-8
Standard Peptide Mix II: Angio 21 (MW: 1045.533900m/z), Angio 1 (MW: 1296.684400m/z, SubsP (MW: 1347.736100m/z)

Sample Preparation Method:

The matrices 9-nitroanthracene ($5*10^{-02}$M) and dithranol ($5*10^{-02}$M) were used in combination with the solvents chlorobenzene and toluene to make several different molar matrix to analyte combinations for PCBM ($2*10^{-04}$M) analysis. The following molar matrix to analyte ratios of 5000:1, 2000:1, 1000:1, 750:1, 500:1, and 250:1 were prepared in toluene for both matrices. The molar matrix to analyte ratios of 5000:1, 2000:1, 1000:1, and 500:1 were prepared in chlorobenzene for both matrices. The prepared samples were all applied to a stainless steel target plate by the dry droplet technique for FTMS analysis. However, only the 1000:1, 750:1, 500:1, and 250:1 molar matrix to analyte ratios composed in toluene for both matrices was applied using the aerospray technique.

The dry droplet technique consisted of using a small aliquot of each sample and applying it to the target plate where it was left out to evaporate—each sample was plated with approximately three 1μl aliquots of sample. The aerospray technique consisted of aerosol particles being spewed from the end of a needle after being conveyed from the sample container by a controlled flow of nitrogen—each application consisting approximately of 50-100μl of sample.

Instrumentation of FTMS:

The samples were analyzed using a 9.4T Bruker Ultraflex FTMS with external ionization source, and a stainless steel target plate while varying the Nd:YAG (355nm) laser power. The laser power was varied relative to its maximum potential at the following percentages, 30, 40, 50, 65, 80, and 100. At each relative laser power three or more mass spectra were obtained and each spectrum was generated from 35 scans each consisting of 30 laser shots. The instrument was calibrated externally using a standard II peptide mix, and referenced against the peptides Angio 1, Angio 21, and SubsP.

Results & Discussion

Preliminary findings suggest toluene and dithranol as optimal matrix and solvent for MALDI:

The preliminary findings consisting of the molar matrix to analyte ratios of 5000:1, 2000:1, 1000:1, and 500:1 composed in all possible forms of matrix and solvent; found that toluene was a more preferred solvent than chlorobenzene as it resulted in an order of magnitude higher for the PCBM signal intensity. Of the matrices dithranol and 9-nitroanthracene, the preliminary results showed that dithranol gave an order of magnitude higher than 9-nitroanthracne for PCBM signal intensity. Also it was noted that 9-nitroanthracene gave no signal intensity for the analyte PCBM at a molar matrix to analyte ratio of 5000:1 for both solvents, and it failed to give a signal at 2000:1 when the solvent chlorobenzene was used.

Spectral Interpretation as they pertain to the matrices and solvents for optimization in MALDI:

Therefore, further analysis of PCBM was conducted using only toluene as the solvent with dithranol and 9-nitroanthracene as the matrices. Spectra where obtained at molar matrix to analyte ratios of: 5000:1, 2000:1, 1000:1, 750:1, 500:1, and 250:1. The aerospray technique was

found to be superior to the dry droplet technique in all the obtained spectra. The use of dithranol at a molar matrix to analyte ratio of 250:1 resulted in the best spectra (figure 1 & figure 2) when it was deposited in by the aerospray technique—see figure 3 for possible reactions that lead to the observed species in figure 2. The best spectra (figure 4) of the 9-nitroanthracene matrix was significantly improved when it was applied using the aerospray technique, however, the signal intensity and signal to noise ratio were an order of magnitude less than those obtained by dithranol—by the same process. The resolution obtained for dithranol and 9-nitroanthracene was very similar in nature, and allowed for isotope peaks to be clearly resolved as a result of the high resolving power of FTMS. The best spectra noted above were found to occur at a relative laser power of 50%.

Influence of Relative laser power on varying molar matrix to analyte ratios:

The relative laser power at various molar matrix to analyte ratios was used to generate bar graphs of the absolute signal intensity of PCBM and the associated signal to noise—which are displayed in figure 5 & 6, respectfully. The higher the relative laser power the more fragmentation that resulted and the relative laser power that was set too low resulted in no obtainable spectra. The relative laser power was found to peak at around 40-50% for both matrices, but 50% gave the best spectra.

Formation of oxidized and hydrated species of PCBM:

The spectra of PCBM obtained using MALDI as the ionization process shows several oxidation and hydration species present. The spectrum shown in figure 3 shows the location of the hydration and oxidative species of PCBM—which can be clearly seen up to the addition of the fifth oxygen and hydrogen. The best spectra (figure 7) obtained using LDI as the ionization process shows the oxidation and hydration of PCBM, but to a much lessened extent. However, the peak at 719.9m/z, identified as the fullerene bulky ball $[C_{60}]^{+\bullet}$, has varying signal intensities between both matrices and ionization processes as shown in figures 1, 2, 4, and figure 7.

LDI and MALDI in relation to Fragmentation and absolute PCBM signal intensity:

In LDI the bulky ball peak dwarfs the PCBM peak which is the opposite in comparison to the MALDI ionization process. However, this is to be expected due to the radiation energy from the laser, which is transferred solely to the analyte in LDI. As a result of the analyte receiving all the energy from the laser it fragments into its next smallest segments, a bulky ball and a methyl ester side group.

The MALDI ionization process also differs in this peak between matrices, dithranol has a higher bulky ball peak than does 9-nitroanthracene, while the same is true for the corresponding PCBM peak intensities. The signal intensities are related to the amount of ions present in the detector, which explains why dithranol has higher peak at 719.9m/z. Dithranol is causing more ionization and therefore more ions than 9-nitroanthraene, and this large increase in ions leads to more fragmentation, and therefore, a higher peak intensity for dithranol at 719.9m/z. However, the cause for this difference is still not completely answered, figure 3 shows a spectrum of 9-nitroanthracene, and it can be seen that the amount of fragmentation is much more expansive with several smaller ion fragment peaks evident than that seen using dithranol as a matrix. Therefore, 9-notranthracene suffers from higher fragmentation than does dithranol.

Figure 1: Spectrum of PCBM (matrix-dithranol, toluene, 250:1, aerospray technique).

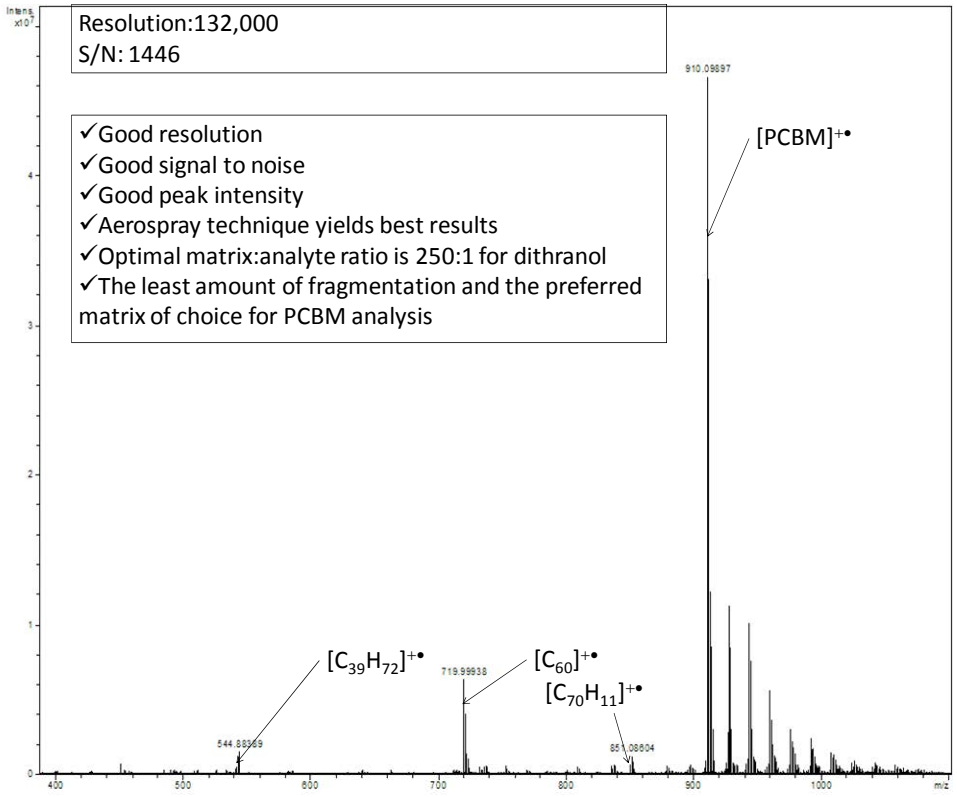

Figure 2: Spectrum of PCBM, expanded section of the above spectrum.

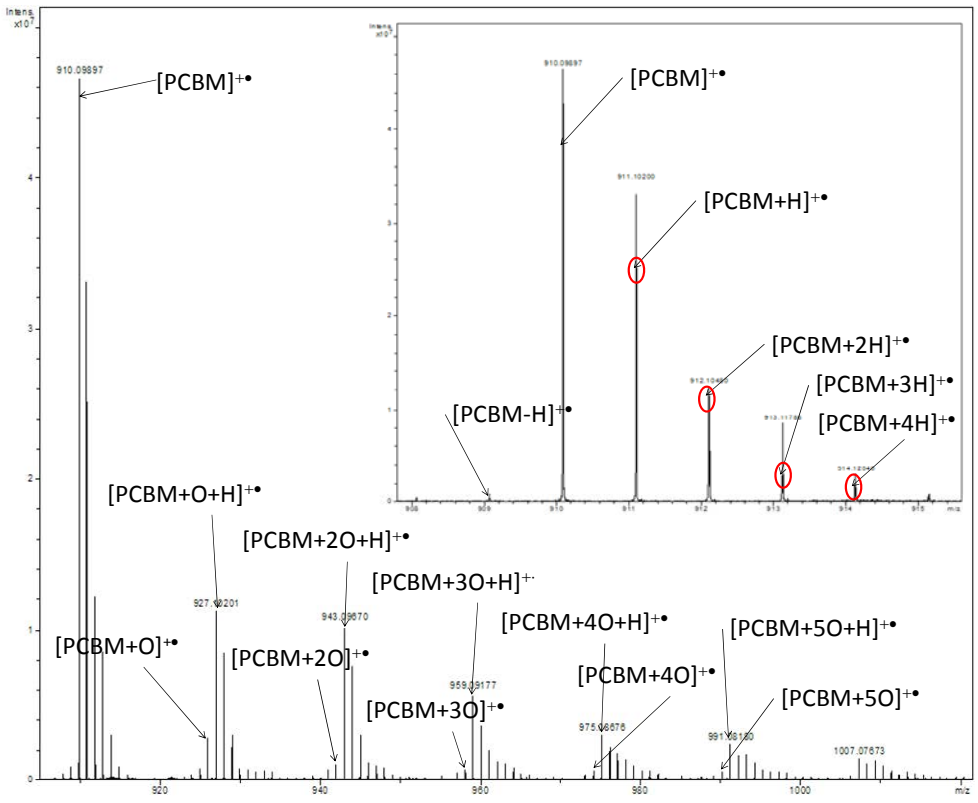

Figure 3: Possible reactions that lead to oxidized and hydrated PCBM species in the above mass spectrum.

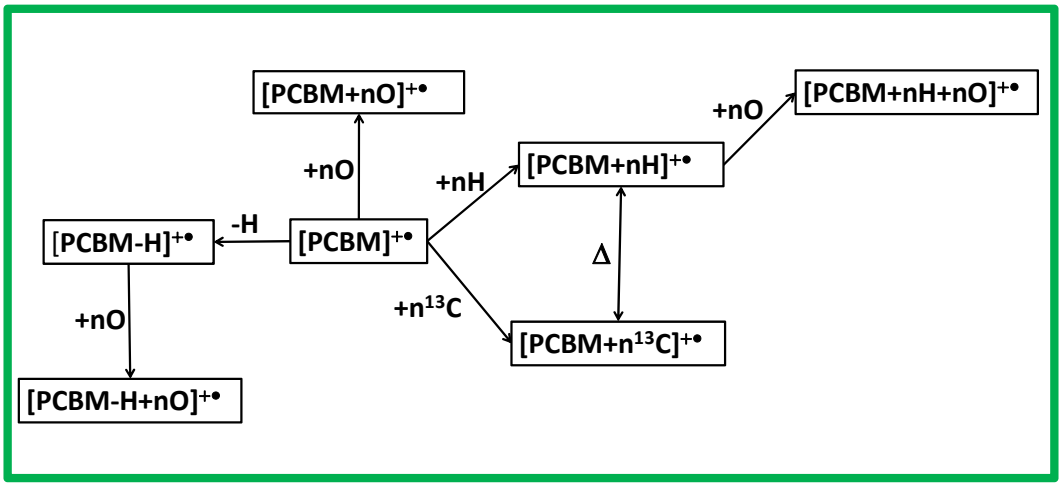

Figure 4: Spectrum of PCBM (matrix-9-nitroanthracene, toluene, 750:1, aerospray technique).

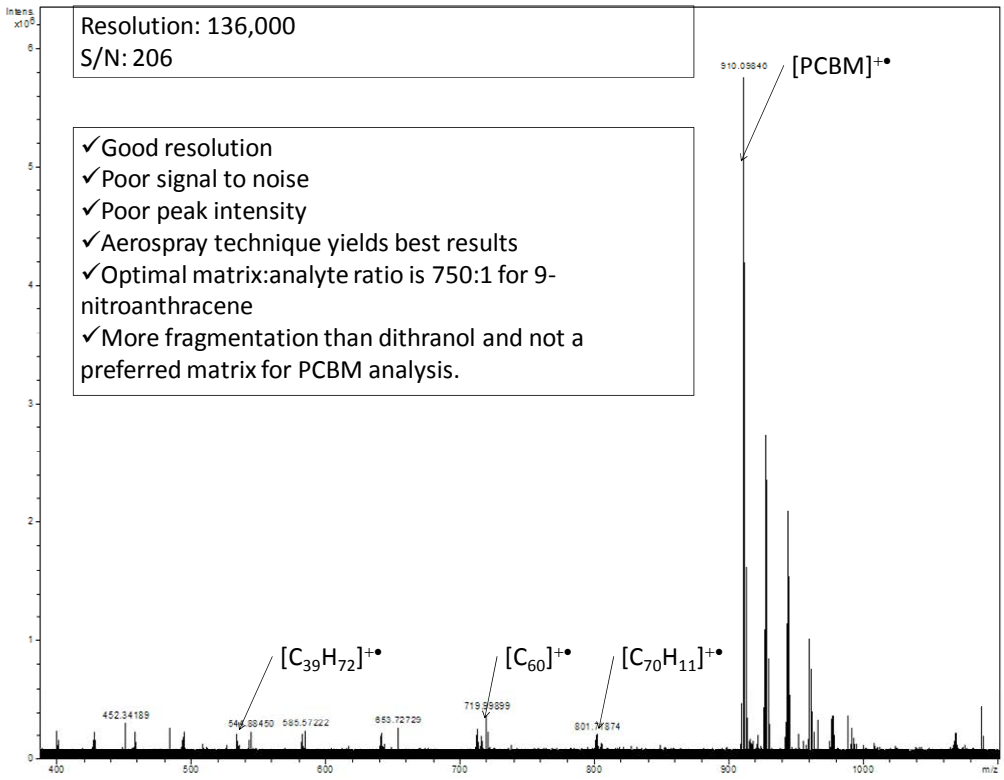

Figure 5: Comparison of absolute peak intensity across several molar matrix to analyte ratios, composed in toluene, and deposited by various techniques.

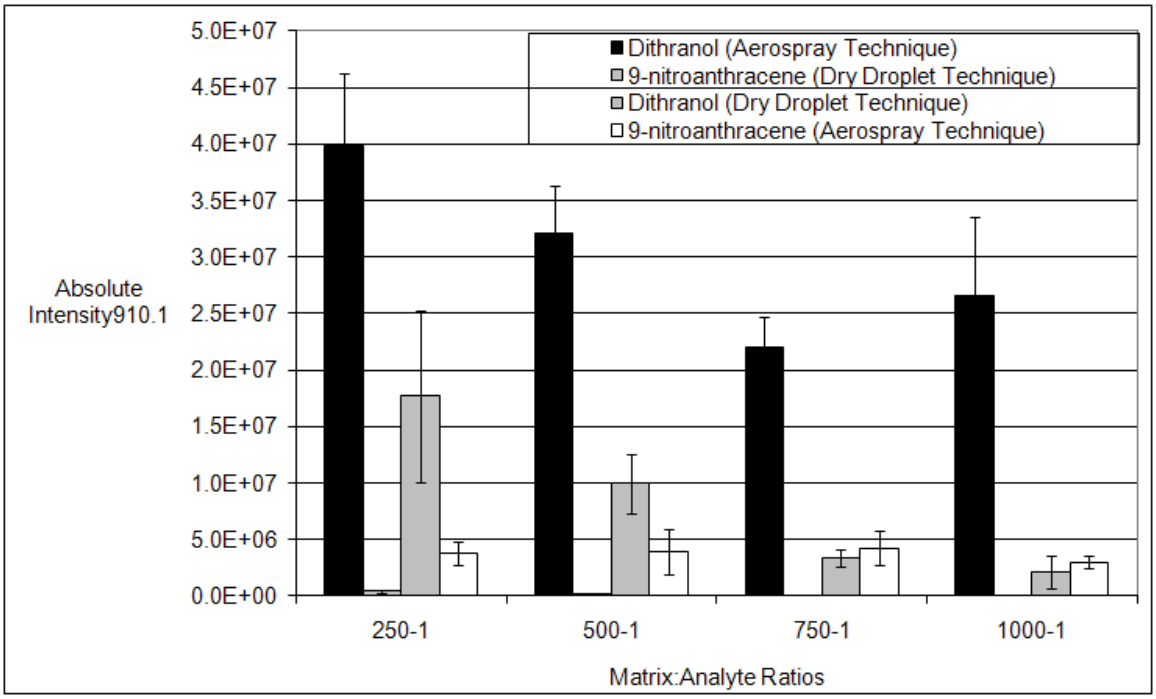

Figure 6: Comparison of signal to noise ratios for various molar matrix to analyte ratios, composed in toluene, and deposited by various techniques.

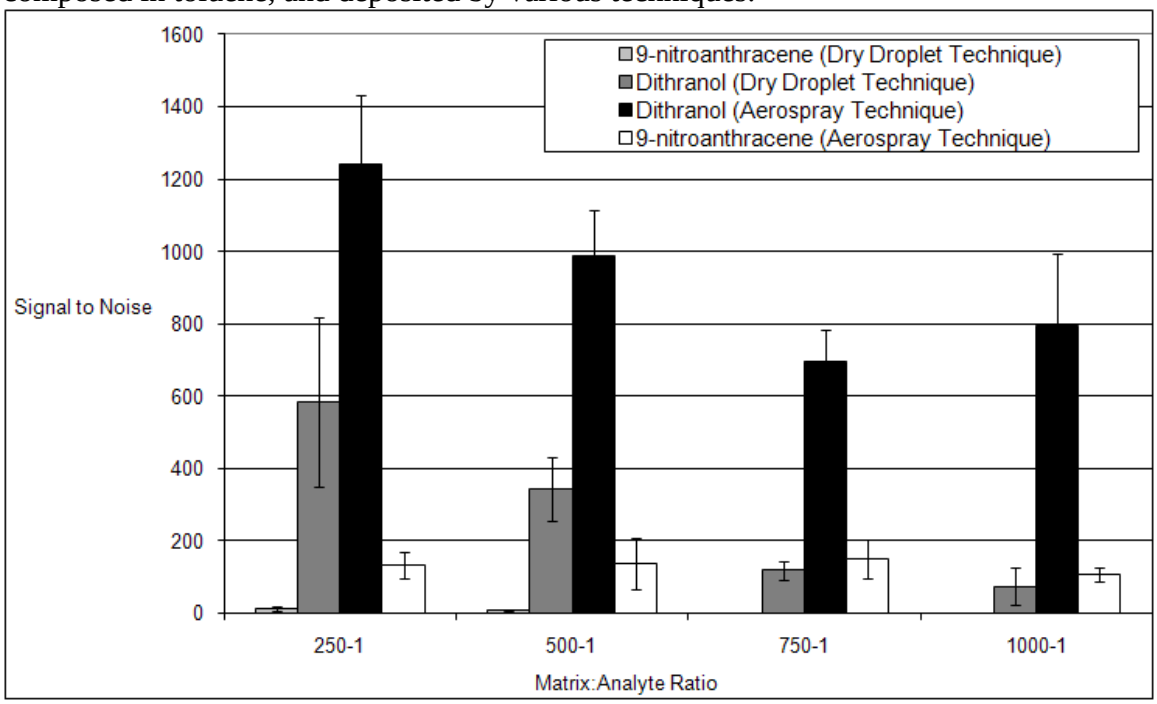

Figure 7: LDI spectrum of PCBM in toluene @ a relative laser power of 50%.

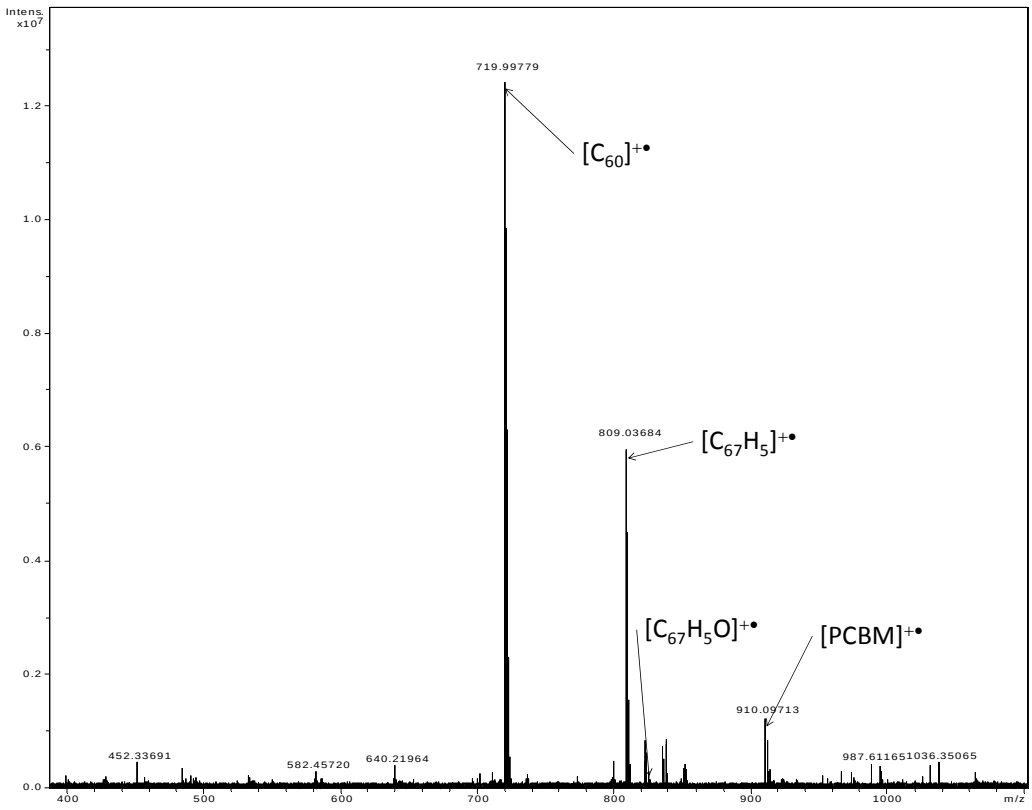

Conclusion

In conclusion reference spectra were obtained, and a peak at 910.1m/z which corresponds to PCBM was observed. Various fragmentation patterns resulted in correspondence to the intensity of the laser, the matrix/solvent, the molar matrix to analyte ratio, and the technique (aerospray or dry droplet) used in the application of the prepared sample. Due to the known problematic reproducibility of MALDI, the error associated with our experiment in measuring signal intensity was significant, but allowed for a more directional analysis of the accurate FTMS reference spectra.

Future Considerations

Future considerations should include NMR analysis of the PCBM sample for prior oxidation and hydration reactions. Also the maximum potential power of the Nd:YAG laser should be measured to bring significant meaning to the obtained laser percentages gathered to date. Another consideration for the future is the use of 2-[(2E)-3-(4-tert-butylphenyl)-2-methylprop-2-enylidene]malononitrile (DCTB) as a matrix for PCBM to be studied via MALDI-FTMS (*10,11*).

Acknowledgements

The following parties should receive recognition for their involvement in the project: The National Science Foundation CHE-0851505/REU, Evgenia Akhmetova, Matthias Knust, and Charles L. Wilkins.

References

1. Roncali, J. *Accounts of Chemical Research*. **2009**, 42, 1719-1730.
2. Hiorns, R.; Cloutet, E.; Ibarboure, E.; Vignau, L.; Lemaitre, N.; Guillerez, S.; Absalon, C.; Cramail, H. *Macromolecules*. **2009**, 42, 3549-3558.
3. Watson, J. T.; Sparkman, O. D. *Introduction to Mass Spectrometry*, 4th Ed.; John Wiley & Sons: West Sussex, 2007, 56-60, 122-127, 519-542.
4. Zenobi, R.; Knochenmuss, R. *Mass Spectrometry Reviews*. **1998**, 17, 337-366.
5. Frankevich, V. E.; Zhang J.; Friess, S. D.; Dashtiev, M.; Zenobi, R. *Anal. Chem*. **2003**, 75, 6063-6067.
6. Knochenmuss, R.; Zenobi, R. *Chem Rev*. **2003**, 103, 441-452.
7. Batoy, S. M. A. B.; Akhmetova, E.; Miladinovic, S.; Smeal, J.; Wilkins, C. L. *Applied Spectroscopy Reviews*. **2008**, 43, 485-550.
8. *Rapid Commun. Mass Spectrom*. **2004**, 18, 360-362.
9. Brown, T.; Clipston, N. L.; Simjee, N.; Luftmann, H.; Hungerbühler H.; Drewello, T. *International J. of Mass Spectrometry*. **2001**, 210/211, 249-263.
10. Zhou, L.; Deng, H.; Deng, Q.; Zheng, L.; Cao, Y. *Rapid Commun. Mass Spectrom*. **2005**, 19, 3523-3530.
11. Vasil'ev, Y. V.; Khvostenko, O. G.; Streletskii, A. V.; Boltalina, O. V.; Kotsiris, S. G.; Drewello, T. *J. Phys. Chem*. A. **2006**, 110, 5967-5972.

Exploring New Reactivity of 2*H*-Azirines in Organocatalysis and Metal Catalysis

Jean-Marie Charles, Cameron University
Lawton, Oklahoma

Abstract

The chemistry of 2*H*-azirines is dominated by ring strain and therefore highly favors the processes in which the strain is relieved[1]. Thus, this study focuses on exploring organocatalyzed opening of 2*H*-azirines to synthesize pyrrolidines with up to four continuous stereocenters. It is proposed that nucleophilic attack of 2*H*-azirines on the acrolein will be activated by a secondary amine and subsequent ring-opening of 2*H*-azirines by the resulting enamine would provide a highly substituted pyrrolidine after reduction.

A new $FeCl_2$ catalyzed method for the synthesis of indoles from 2*H*-azirines has recently been developed in Zheng's lab. This study also focuses on increasing the efficiency of this method by synthesizing the indoles directly from the pentafluorobenzoates of oximes hence bypassing 2*H*-azirines as the intermediate.

Introduction

Carbon-nitrogen(C-N) bond formation has been shown to play an important role in drug discovery. A recent survey of GMP (Good Manufacturing Practice) reactions ran in Pfizer's pilot plants showed that it accounted for 15% of the reactions during the period between 1985 and 2002[2]. It is steadily rising due to the increasing use of nitrogen-containing compounds as pharmaceuticals and biological probes. Though there are various methods available for C-N bond formation, many of them depend on functional group interconversion and form only one bond[3] and are not very efficient or environmentally sustainable. For this reason, the focus of my REU studies at the University of Arkansas was to explore 2*H*-azirine chemistry in the synthesis of pyrrolidines and indoles. This is a part of the Zheng group's long term goal to create economical, efficient, environmentally sustainable methods centered on C-H functionalization and cascade reactions.

2*H*-azirines are the smallest unsaturated nitrogen-containing heterocycles. Two isomers of azirines are known to exist: 1*H*-azirines containing a carbon-carbon double bond, and 2*H*-azirines having a carbon-nitrogen double bond in the three-membered ring. 1*H*-azirines, which are anti-aromatic, are much less stable than 2*H*-azirines and tautomerize into 2*H*-azirines. 2*H*-azirines possess a highly reactive nature that is influenced by their ring strain, making them useful precursors to synthesize more elaborate heterocycles[4]. Although this class of compounds has been used as building blocks to synthesize other heterocycles, they have been seldom studied in organocatalysis and hence influenced our interest in doing so.

Interests in synthesizing indole derivatives have been flared since they have been shown to be useful in pharmaceutical compounds and bioactive natural products[5]. Recently, a new catalytic method for the synthesis of indoles using substantially cheaper and environmentally responsible iron salts was developed in Zheng's lab. Although there are many procedures available for the preparation of indoles, it is still a challenge to synthesize indoles bearing

various substituents from readily available starting materials[6]. Thus, the aim was to increase the efficiency of this new method by synthesizing indoles directly from the pentafluorobenzoates of oximes hence bypassing 2*H*-azirines as the intermediate.

Synthesis of 2*H*-Azirines

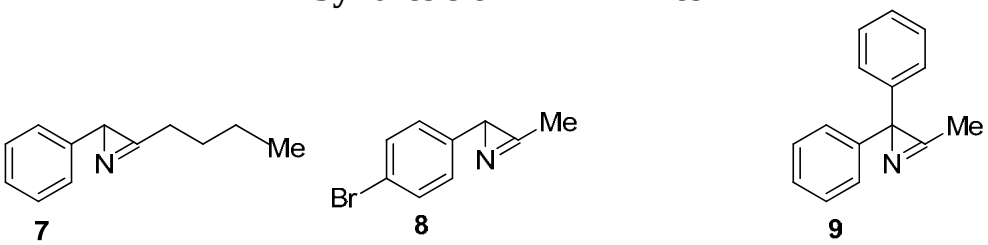

7 **8** **9**

Three 2*H*-azirines were used in the study. Azirines **7** and **8** were synthesized using sequence I and azirine **9** was synthesized via sequence II. Sequence I was developed by Douglass F. Taber. In this sequence, ketone **1** was converted to oxime **2**, which was subsequently converted to 2*H*-azirine **4** via mesylate intermediate **3**.

The conversion of ketone **1** to oxime **2** was accomplished by adding hydroxylamine hydrochloride and sodium acetate to ketone **1** in methanol/water (20:1), providing **2** as a racemic mixture of *E* and *Z* isomers in 86% combined yield. It was assumed that only one of the isomers would form 2*H*-azirine **4** if the vinyl nitrene intermediate was not involved in the ring formation. Therefore, the two isomers were separated using silica gel chromatography and parallel reactions were set up to test this assumption. Indeed, it was observed that after the addition of triethylamine and methanesulfonyl chloride followed by 1, 8-Diazabicyclo[5.4.0]undec-7-ene (DBU) only the major isomer, presumably the *E* isomer, was converted to azirine in 40% yield.

Sequence I

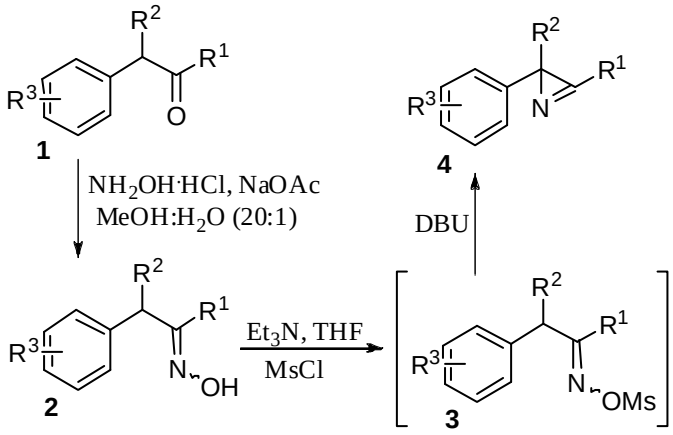

Taber D.F.; Tian, W. *J. Am. Chem. Soc*. **2006**, *128*, 1058-1059.

Scheme 1. Sequence for Synthesis of 2*H*-Azirines 7 and 8

The synthesis of 2*H*-azirine **9** was accomplished using sequence II developed by Padwa and Carlsen. In this sequence, treatment of oxime **1** with dimethylhydrazine in the presence of sodium acetate and acetic acid afforded dimethylhydrazone **5**, which was then converted to

quaternary ammonium salt **6** via a reaction with methyl iodide and then finally cyclized into azirine **4** by the treatment of sodium hydride.

Sequence II

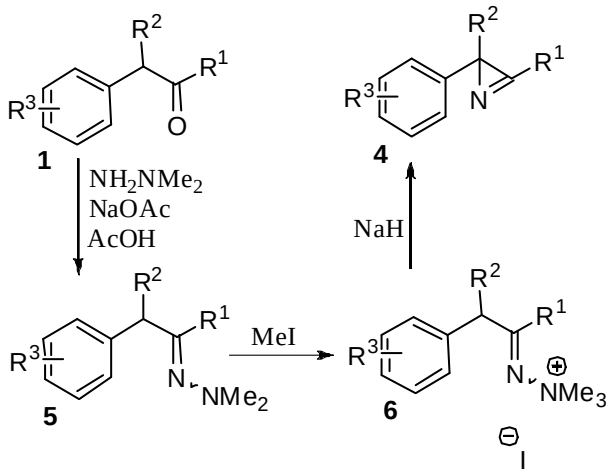

Padwa, A.; Carlsen, P.H.J. *J. Org. Chem.* **1978**, *43*, 2029-2037.

Scheme 2. Sequence for Synthesis of 2*H*-Azirine 9

Results and Discussion

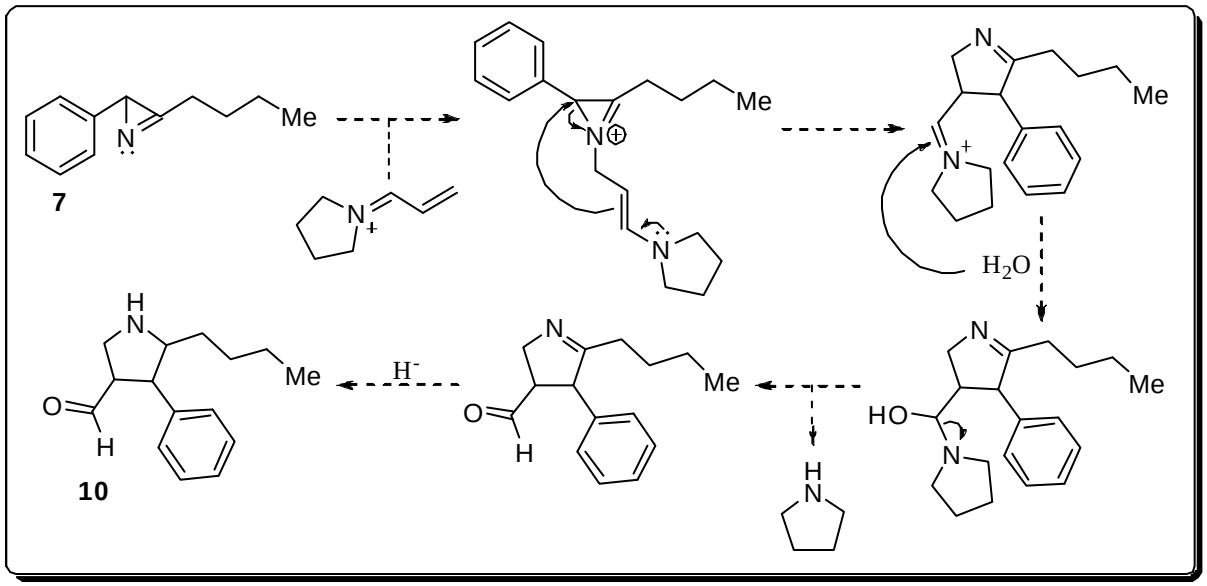

Scheme 3. Proposed Synthetic Route for Pyrrolidine Derivative

Scheme 3 shows our proposed synthesis of a pyrrolidine derivative starting from 2*H*-azirine **7**. In this scheme, it was proposed that the secondary amine would undergo 1, 2-addition to acrolein converting the carbonyl group to an iminium ion and thereby making the C_4 carbon

more electrophilic. Since the 2*H*-azirine nitrogen atom is reasonably nucleophilic, it was expected that it would attack the C_4 carbon of the iminium ion to generate an enamine. Then subsequent ring-opening of 2*H*-azirines by the resulting enamine would form an intermediate that would convert to an aldehyde by exposure to water, the byproduct from the formation of the iminium ion, and regenerate the secondary amine thus completing the catalytic cycle. Finally after reduction, the highly substituted pyrrolidine would be obtained.

Azirine **7** and acrolein were combined in THF with two different amines separately: first pyrrolidine, then L-proline. However, in each experiment no reactions were observed, with 2*H*-azirine **7** being completely recovered.

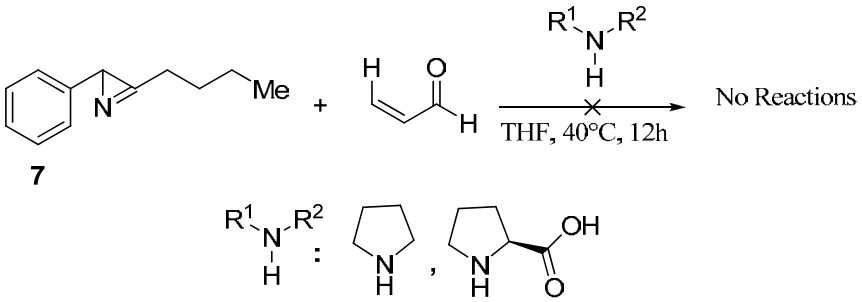

Then separately, in the presence of L-proline, 2*H*-azirine **9** was treated with acrolein, methyl vinyl ketone and cyclopentenone respectively. However, no reactions were observed in these experiments either. It is proposed that the nitrogen atom in these 2*H*-azirines were not as nucleophilic as had been anticipated and thus the reactions did not follow the synthetic scheme.

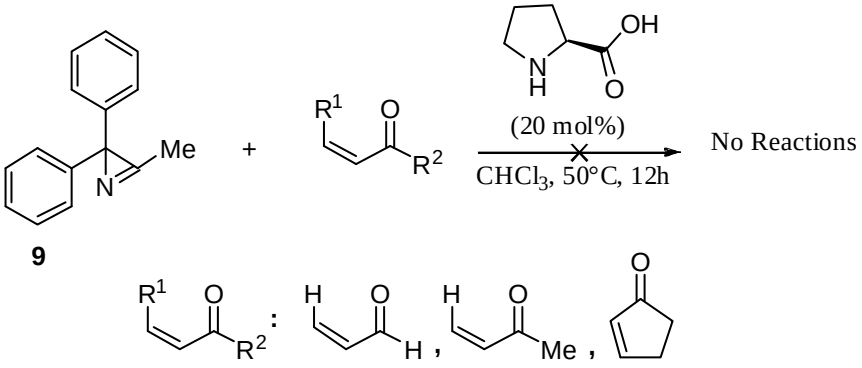

The proposed synthetic scheme for indole derivative **13** is depicted in scheme 4. It was assumed that treatment of pentafluorobenzoate **12** with a metal catalyst in THF would provide the indole derivative via an imine radical, which would undergo cyclization onto the benzene ring.

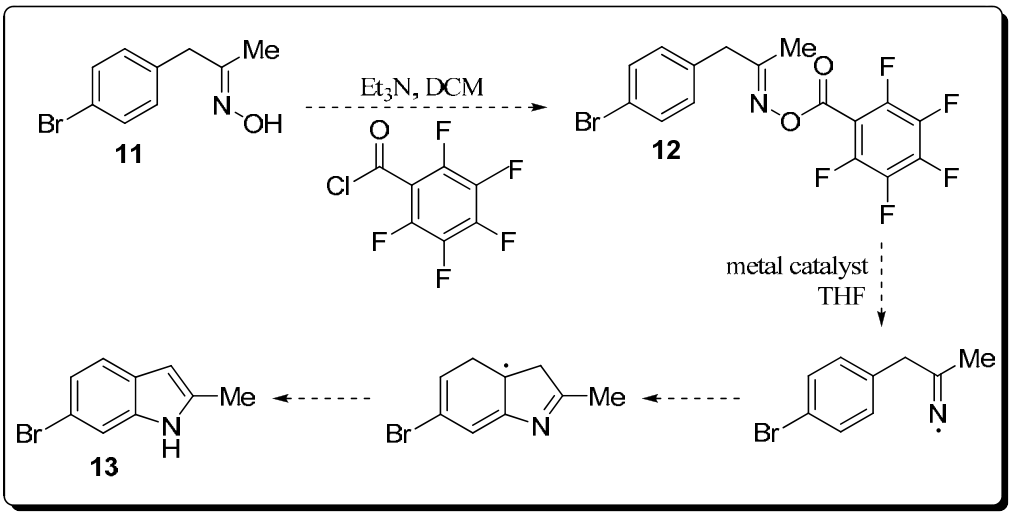

Scheme 4. Proposed Synthetic Route for Indole Derivative

As shown in Table 1, several reaction conditions were set up using pentafluorobenzoate **12** with some transition metal catalysts in THF. Indole **13** was not isolated in any of the reactions. Instead there were several byproducts observed, one of which was identified as 4-bromophenylacetone **14**. We thought that we were not able to obtain the desired indole derivative because the imine radical did not cyclize onto the benzene ring as expected.

Table 1. Catalyst Screening

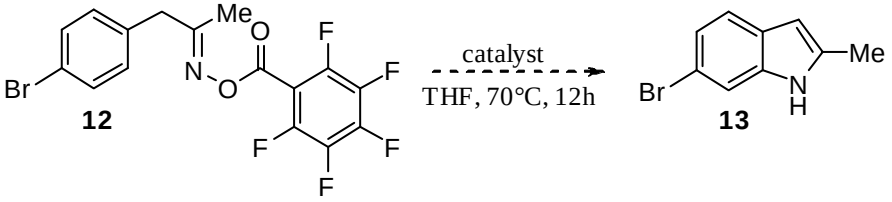

entry	catalyst (mol %)	**13**, yield (%)
1	CuCl (50)	0[a]
2	$CuCl_2$ (50)	0
3	CuTC (50)	0
4	$[CF_3SO_3Cu]_2 \cdot C_6H_5CH_3$ (10)	0
5	$FeCl_2$ (50)	0
6	$FeCl_3$ (50)	0[a]

[a] 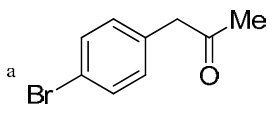 was obtained.

14

Conclusion

In conclusion, in this study we have examined the reactivity of 2*H*-azirines with enals and ketones. We observed that 2*H*-azirines were completely recovered in the experiments and the desired pyrrolidine derivative was not formed. We were not able to obtain the indoles directly from the pentafluorobenzoates of oximes either. We did, however, observe several byproducts in the screening experiments, one of which was identified as ketone **14**.

Acknowledgements

This work was supported by funding from University of Arkansas, Arkansas Bioscience Institute and the National Science Foundation CHE-0851505/ REU. I would also like to thank Daniel Rackl for synthesizing **9** and Dr. Nan Zheng, Dr. Samaresh Jana, Dr. Mingzhao Zhu and Mack D. Clements (University of Arkansas, Department of Chemistry and Biochemistry) for their contributions to the study.

References

(1) Pinho e Melo T. M. V. D.; Rocha Gonsalves A. M. Exploiting 2-Halo-2H-Azirine Chemistry. *Curr. Org. Synth.* **2004,** *1* (3), 275-292.

(2) Dugger, R. W.; Ragan, J. A.; Brown Ripin, D. H. *Org. Process Res. Dev.* **2005,** *9*, 253-258.

(3) *Modern Amination Methods*; Ricci, A., Ed.; Wiley-VCH: Weinheim, **2000**.

(4) Palacios, F.; de Retana, A. M. O.; de Marigorta E. M.; de los Santos, J. M. *Org. Prep. Proced. Int.* **2002,** *34* (3), 219-275.

(5) Kawasaki, T.; Higuchi, K. *Nat. Prod. Rep.* **2007**, *24*, 843-868.

(6) Chiba, S.; Zhang, L.; Sanjaya, S.; Ang, G. Y. Pd(II)-catalyzed Synthesis of Indoles from α-aryloxime O-pentafluorobenzoates via Intramolecular Aromatic C-H Amination. *Tetrahedron.* **2010,** *66* (30), 5692-5700.

Computer Modeling of the Thermal Rearrangement of 2-aryl-2H-azirines to Indoles

Vernon D. Crowell Jr., Lyon College
Batesville, AR

Introduction

Indoles are aromatic bicyclic nitrogenous compounds, and consist of a benzene ring fused to a five-membered pyrrole ring.[1] These compounds see wide use in the pharmaceutical industry and are commonly found in nature. This has inspired synthetic chemists to devise practical methods to produce indoles, methods that should tolerate a wide range of functional groups.[2] Current experimental work by Zheng et. al seeks to investigate a process that has been known since the 1970s: the thermal rearrangement of 2-aryl-2H-azirines to indoles. This method allows for the simultaneous introduction of substituents onto carbons 2 and 3 of the indole heterocycle. Also, 2H-azirines are easily prepared from common ketone precursors.[3] Prior investigations of this reaction were catalyzed by either $Pd(PhCN)_2Cl_2$ or $Rh_2[OC(O)CF_3]_4$. These catalysts are expensive, so Zheng et. al sought cheaper alternative catalysts. In an attempt to optimize catalytic conditions, a number of Fe(II), Fe(III), Cu(I), and Cu(II) compounds were allowed the opportunity to react with the 2H-azirine in a variety of solvents. It was determined that $FeCl_2$ in THF provided the highest yield of the indole product. In fact, THF was the only solvent that allowed the Fe(II) rearrangement to go to completion, suggesting the formation of a iron(II)-THF complex. This information and the previous discovery that 2H-azirines rearrange to indoles via vinyl nitrene intermediates led to the proposal of a catalytic cycle involving Fe(II).[4]

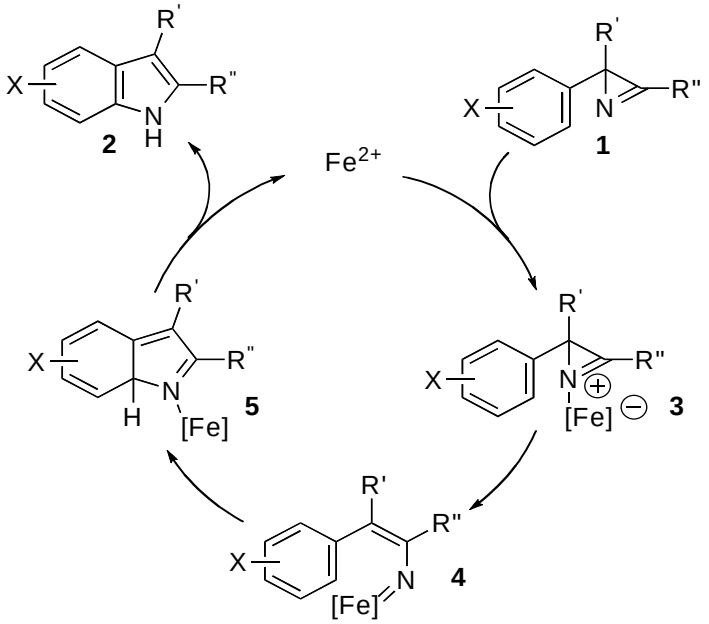

Figure1. The catalytic cycle proposed by Zheng et al.

In the above cycle, R can be phenyl, alkyl, or a hydrogen. R′ can only be phenyl or methyl. If R′ is a hydrogen, the reaction doesn't proceed within 24 hours.

Computational Details

The catalytic cycle proposed by Zheng et al. was modeled using density functional theory(DFT) with the PQS program package. Calculations were peformed using the B3LYP hybrid functional with the m6-31g-d basis set. DFT is able to provide quite accurate results for many systems at a lower computational cost than post-Hartree-Fock methodologies. In the present context, it is important that DFT works well for transition metals where a number of other methods have difficulties.[5] There are many variants of DFT, depending on the choices of the exchange-correlation functional that is used to mimic the effect of electron correlation. B3LYP is perhaps the most widely used exchange correlation functional, and has been thoroughly tested for transition metal compounds. Another important question is the choice of the atomic basis set used to describe the molecular orbitals. This should be large enough to allow accurate predictions but not so large that the calculations become too expensive. The 6-31g(d) basis is generally accepted as a reasonable compromise. However, for late transition metals, it has a deficiency that has been corrected in the m6-31g(d) basis.

Full geometry optimizations were performed on the initial reactants, the product indole, and the intermediates. The use of optimized scans allowed the discovery of approximate transition state geometry. These approximate geometries were then used to perform transition state optimizations.

The initial catalyst was assumed to be the high spin tetra-coordinated $Fe(THF)_2Cl_2$. Since it was found that $FeCl_2$ only catalyzed the rearrangement in THF solvent, it is likely that a complex forms between the iron(II) chloride and the THF. Due to the low dielectric constant of the THF solvent, it is unlikely that a chloride ligand is displaced by either THF or the 2H-azirine. Also, a complex with more than two THF ligands is likely less stable due to steric effects. Because both the chloride and the THF ligands are weak-field ligands, the iron(II) complex should be high-spin. It has been noted[6] that four coordinate complexes with large ligands and small metal ions prefer a tetrahedral structure. With a d^6 ion in a high-spin tetrahedral ligand field, the complex should be most stable in the quintet state.

Initial calculations were for species with methyl groups attached to C2 and C3 of the azirine ring. Some calculations were later performed with hydrogen replacing the methyl group as the substituent on C2. In the first step of the reaction, the 2H-azirine displaces a THF from the $Fe(THF)_2Cl_2$ complex. After obtaining the optimized geometry of the azirine iron complex, the unusually long C-N single bond (1.546 Å) was scanned in an attempt to find an approximate transition state in the vinyl nitrene formation step. However, when the C-N bond length approached 2.0 Å, a region of triplet instability resulted in the inability of the SCF to converge. Instead of starting the scan with the iron(II)-azirine complex, we reversed the direction of the scan, and scanned the C-N distance from 2.4 Å (a little longer than the C-N distance in the optimized nitrene) to 1.5 Å, a little shorter than the C-N distance in the azirine ring. Initially, the distance was incremented by .05 Å, but this led to an inaccurate approximation of the transition state, due to not having a well defined local maximum along the reaction path. By running smaller scans in the area of the maximum, a better approximation was obtained. This approximate transition state was then optimized. After optimization, a frequency calculation was performed to verify that the optimized structure was a true transition state. Transition states must have only one imaginary frequency, since a transition state is only a maximum along the reaction path and a minimum along all other paths. The frequency is imaginary at a maximum due to the negative force constant. The vibrational frequency can be expressed classically as

$$f=\frac{1}{2\pi}\sqrt{\frac{k}{\mu}}$$

where k is the force constant and μ is the reduced mass of the system. Since at a maximum the energy of the system can only go down along the reaction path, the force constant corresponding to the reaction coordinate is negative, which formally results in an imaginary frequency. Even after affirming that the geometry is a transition state, it is necessary to verify that it is the correct transition state. In a large system such as the azirine complex, there are many possibilities for conformational changes, which correspond formally to transition states but are of little interest. In order to verify that the transition state corresponded to the breaking of the C-N bond, vectors of the imaginary frequency were viewed. The vectors with the highest magnitude corresponded to the breaking of the C-N bond.

Another optimized scan was performed to locate the approximate transition state in the formation of the indole tautomer. The coordinate scanned this time was the distance between the nitrogen and the benzene carbon ortho to the initial azirine ring. Scanning from 2.9 to 1.35 Å with steps of .05 Å, an approximate transition state geometry was found. The transition state was verified with a frequencies calculation and by checking the vectors of the imaginary frequency.

The next reaction step involved the migration of the hydrogen on the bridgehead carbon bound to the nitrogen to the nitrogen. This migration also led to the aromatization of the system and significantly lengthened the N-Fe bond. A scan was performed that incremented the H-N distance by .025 Å from 2.10 to .975 Å. The approximate transition state geometry was optimized and verified. After the H-migration the iron(II) complex breaks off, reforming the initial catalyst.

Results/Discussion

After obtaining all the transition state geometries along the catalytic cycle, the barrier heights of each reaction step were calculated.

Reaction Step	Barrier Height (kcal/mol)
IM1-IM2	8.06
IM2-IM3	15.27
IM3-IM4	24.07

Table 1 : Barrier heights for various steps in the catalytic cycle.

Compounds	Energy(kcal/mol) Relative to R + C
IM1 + THF	1.48
TS1 + THF	9.54
IM2 + THF	2.60
TS2 + THF	17.87
IM3 + THF	-14.66
TS3 + THF	9.41
IM4 +THF	-36.19
PDT +C	-44.96

Table 2: Energies relative to the reactant are shown.

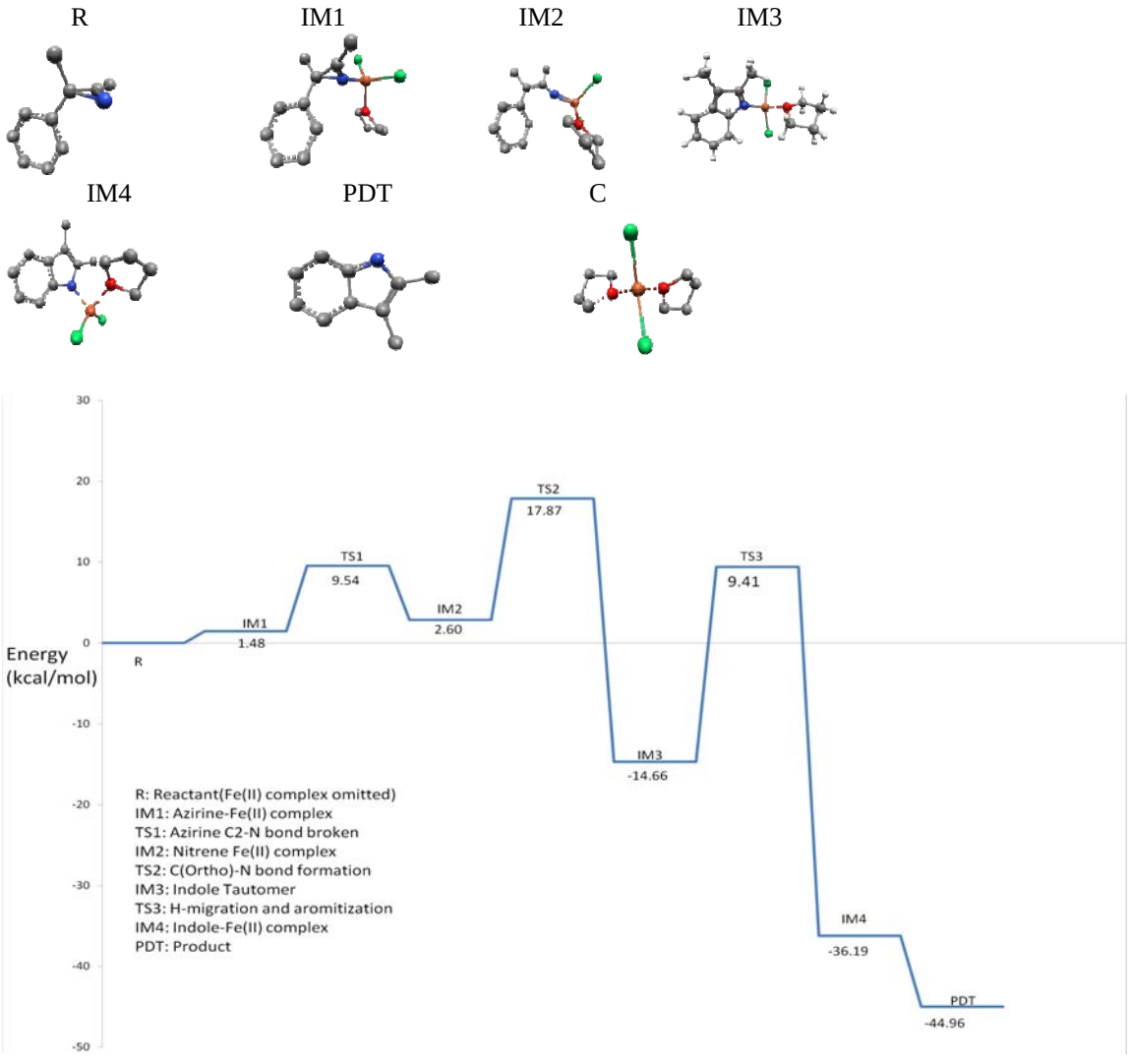

The highest barrier between intermediates is TS3 which is 24 kcal/mol above IM3. This would imply that the hydrogen migration step is the rate determining step. However, this would be the case only if IM3 reaches thermal equilibrium with the surroundings before it reacts

further, which is not likely. At the moment of its formation, IM3 is hot (it is more than 30 kcal/mol below TS2), and this energy is deposited in the immediate vicinity of the migrating hydrogen atom, giving it ample energy to overcome the TS3 barrier. Moreover, hydrogen migration is known to occur through tunneling, meaning that the full activation energy wouldn't be needed for the reaction to proceed. It is much more likely that the formation of the indole tautomer in the preceding reaction step determines the reaction rate. This transition state (TS2) is calculated to be significantly higher relative to the reactants than TS3. It is interesting to note that for the H substituted azirine, the barrier to the formation of the indole tautomer is 18.81 kcal/mol, which is 3.54 kcal/mol higher than the methyl substituted system. Using the Arrhenius equation, the relative reaction rate of indole tautomer formation between the differently substituted systems can be determined. The tautomer formation step is estimated to be 180 times slower in the H substituted molecule than in the methyl substituted system. However, this reasoning omits the role of the quasi-equilibrium between the reactants and IM2. In the hydrogen form, IM2 is lower relative to the reactants than in the methyl form. In the quasi-equilibrium picture, the relative reaction rates are determined by the energy of TS2 relative to the reactants. The hydrogen form is still estimated to react more slowly than the methyl form but the ratio is only about 1:6.

Conclusion

The proposed catalytic cycle of Zheng et al. seems to be plausible. The rearrangement begins when the azirine displaces a THF from the iron(II) catalyst. The long C-N bond of the azirine ring is broken to form a vinyl nitrene complex. Then, in the probable rate determining step, an indole tautomer is formed after a barrier of around 15 kcal/mol is overcome. After the formation of the tautomer, the hydrogen migrates and the iron(II) complex is expelled, forming the indole product.

Future Plans

In the future, the geometries of important points of the reaction path will be reoptimized using a larger basis set. Also, different exchange-correlation functional will be used.

Acknowledgements

The author wishes to acknowledge the National Science Foundation CHE-081505/REU. The Pulay group and Dr. Zheng provided vital support to this research.

References

1. Joule, J.A., Mills, K. *Heterocyclic Chemistry*, 5th edition; Blackwell Publishing: 2003.

2. Humphrey, G.R.; Kuethe, J.T. *Chem. Rev*. 2006, 106, 2875-2911.

3. Padwa, A.; Rosenthal, R.J.; Dent, W.; Filho, P. J. Org. Chem. 1984, 49, 3174-3180.

4. Jana, Samaresh; Clements, Mack D.; Sharp, Barry K.; Zheng, Nan. "Fe(II)-Catalyzed Amination of Aromatic C-H bonds via Ring Opening of 2H-Azirines: Synthesis of 2,3-Disubstituted Indoles." Accepted for publication by JACS.

5. Siegbahn, P.E.M.; Borowski, T. *Acc. Chem. Res*. 2006, 39, 729-738.

6. Hawrelak, Eric J.; Bernskoetter, Wesley H.; Lobkovsky, Emil; Yee, Gordon T.; Bill, Eckhard; Chirik, Paul J. *Inorg. Chem*. 2005, 44, 3103-3111.

Progress toward Water Soluble Mono-Functionalized Nano Particles for Biological Sensors

Anna Fielder, University of Arkansas
Fayetteville, Arkansas

Abstract

The specific aims of this project are to synthesize, characterize, and optimize appropriately functionalized dendrons for ligation to nontoxic quantum dots (QD's) in order to increase water solubility via solid phase "click" chemistry. Once completed, addition of a single protein, specifically Cdc42 - a member of the Ras proteins, will attach in one of four locations: the C-terminal his_6-tag, a free cysteine, a free lysine, or a p-AcPhe.

Introduction

Understanding science at the nano level has become increasingly important in today's world. The idea of the applications for tools at the atomic level has been around for many years, as expressed by the Nobel physicist Richard Feynman.[1] Thanks to current research, many diagnostic applications as well as intracellular imaging applications for QD's have been determined, summarized in **Figure 1**. [2]

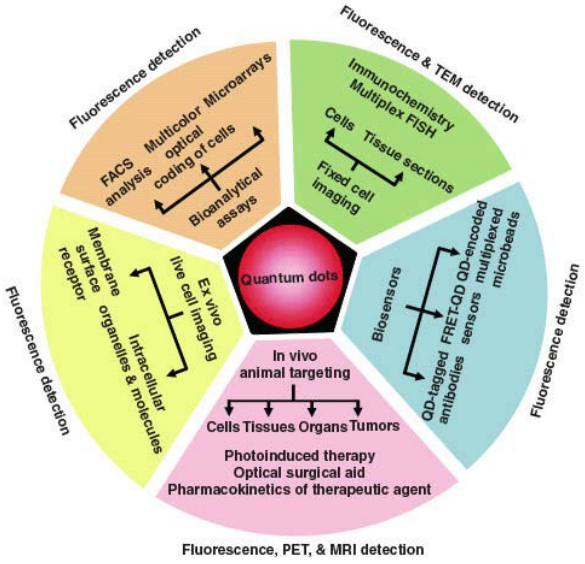

Figure 1

In this project, two classes of newly developed doped quantum dots (d-dots) and NIR-emitting core/shell/shell QD's will be used. As opposed to QD's previously studied, d-dots and core/shell/shell QD's do not contain the toxic compound cadmium, making them safer for biological applications. D-dots have the advantages of large thermal stability and are zero self-quenching. Synthetic techniques of the Peng research group will be employed. [8-12] Currently, literature exists that provides methods for preparing mono-functionalized Au nanocrystals.[3-7] Some of these ideas will be carried over into the research of the mono-functionalized water-soluble d-dots as well.

Once mono-functionalization and water solubility have been achieved, the aim is to attach a single protein to the mono-functionalized location. Cdc42 will be used which a member of the Ras (**Ra**s **S**arcoma) super family of GTP-binding signaling proteins. The Ras proteins were among the 'first' human oncogenic proteins to be identified.[13] 30% of cancer's have shown to contain mutated expressions of the Ras proteins, therefore making it a great protein to attach for bioimaging. The overall goal is summed up in **Figure 2**.

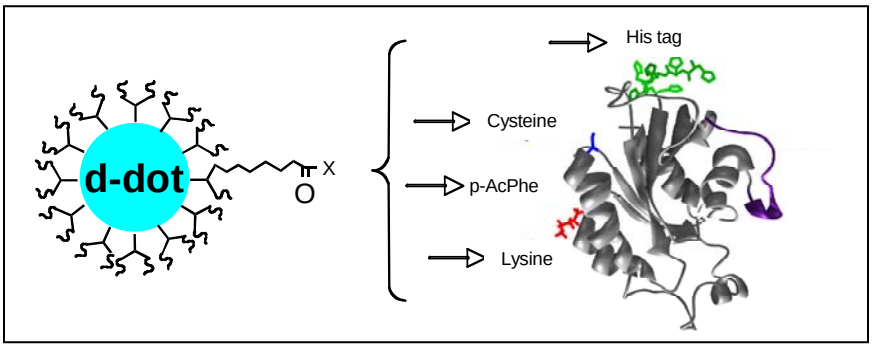

Figure 2

Scheme 1 represents the outline of the chemical target whose synthesis will be outlined in **Scheme's 2** and **3.** Due to insolubility of ligated nanoparticle, solid phase synthesis reactions with click chemistry give rise to a water-soluble ligated nanoparticle.

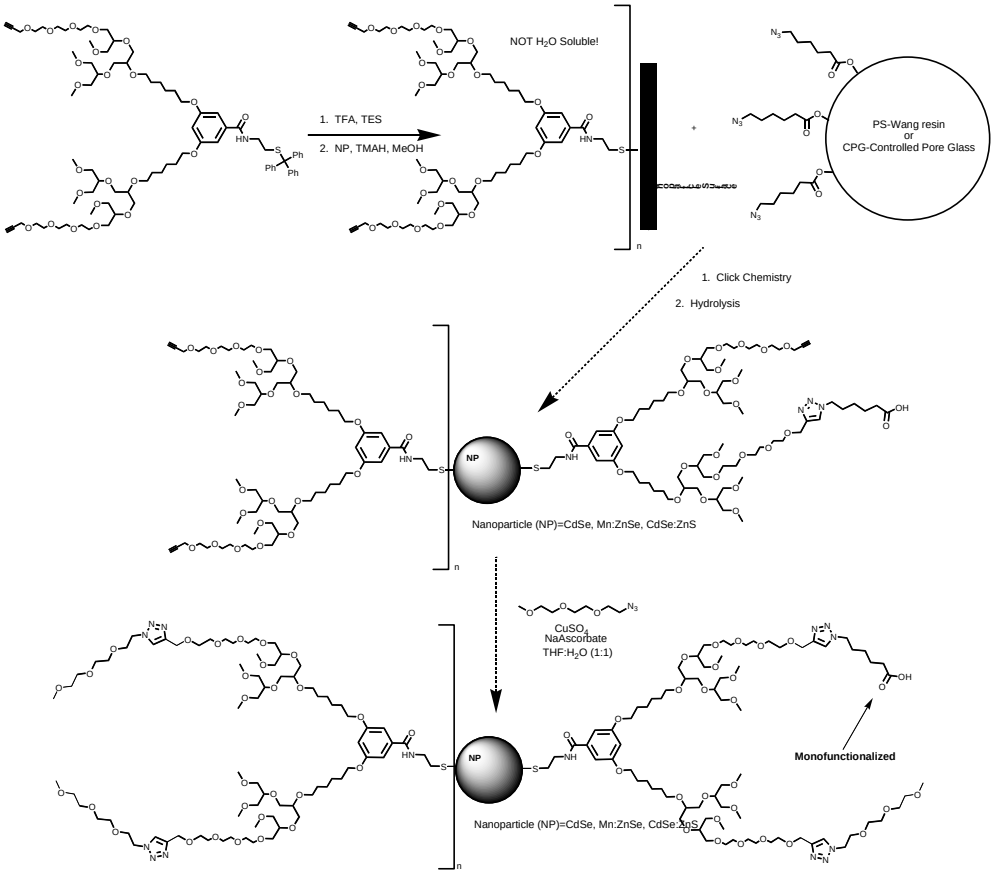

Scheme 1

Results and Discussion

1. Ligand Synthesis

The overall scheme of the ligand synthesis is represented in **Scheme 2**. It proceeds in good yields without need of extensive purification.

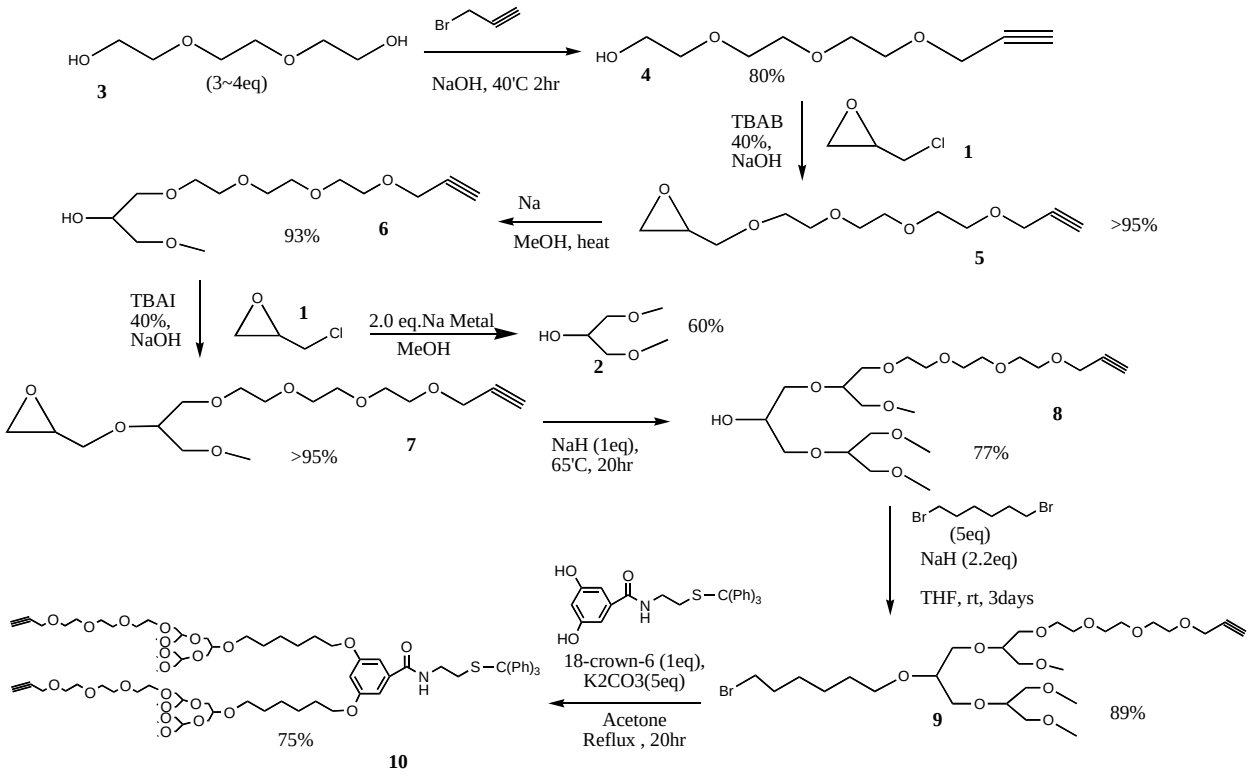

Scheme 2

Triethylene glycol **3** was treated with NaOH and Propargyl bromide at 40'C for 2 hours to give the Polyethylene Gylcol (PEG) alkynl alcohol **4** in 80% yield**.** The remaining 20% was the disubstituted dialkyne. To compound **4,** was added an aqueous solution of 40% w/w NaOH, 10% Tetrabutylammonium bromide (TBAB), and Epichlorohydrine **1**, to give the alkynyl epoxide **5** in >95% yield. To compound **5,** was added a sodium methoxide solution prepared by adding Na metal to MeOH to give the first generation (1G) alcohol **6** in 93% yield. A similar reaction was done between epichlorohydrine and sodium methoxide solution in MeOH to give the dimethoxy alcohol **2** in 60% yield after vacuum distillation. To the 1G was added compound **1**, TBAB, and 40% aq. NaOH to give compound **7** in >95% yield. To compound **2** was added NaH under inert N_2 atmosphere to form the alkoxide followed by addition of **7** to give compound second generation (2G) **8** in 77% yield after chromatography. It is important to note that there was no purification required for the first series of reactions. The only byproduct, the dialkyne from the first step, was an un-reactive intermediate that was carried through to compound **8** where it was removed by column chromatography. Compound **8** was added to a solution of NaH in THF under N_2 followed by 1,6-Dibromohexane and stirred for 3 days to create the second generation

alkyl bromide **9** in 89% yield. Finally, combined with **9** was a trityl (tripheynlmethane) protected thiol, 18-crown-6, K_2CO_3, MeCN and DMF and left to stir for 20 hours at 85'C to obtain the third generation (3G) protected thiol target ligand, compound **10,** in a 75% yield after purification.

2. Optimization of Water Solubility

Due to the insolubility of the nanoparticle after ligand exchange, something had to be added to the ligand to increase solubility. Two separate methods to prepare the same compound **13** were tried as shown in **Scheme 3**.

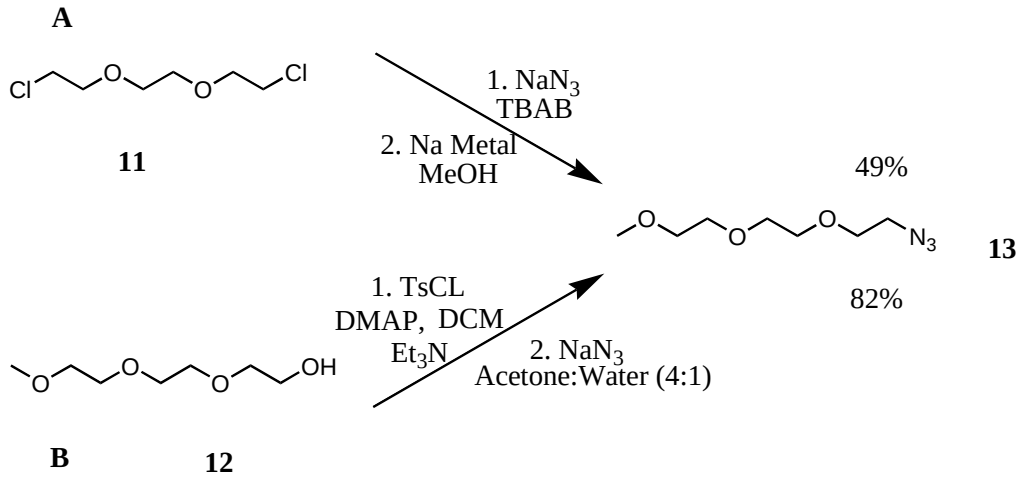

Scheme 3

In reaction A, compound **11,** NaN_3 and TBAB, followed by a secondary reaction of Sodium metal and MeOH to give rise to compound **13**. In order to optimize the reaction conditions and minimize the diazide byproduct, parallel synthesis was performed with the following ratios and results listed in **Table 1**.

Sample	Dichloro	NaN_3	TBAI (g)	Dichloro	Mono-Azide	Di-Azide
1	4	1	0.003	83%	17%	0%
2	3	1	0.003	78%	22%	0%
3	2	1	0.003	76%	22%	2%
4	1	1	0.003	40%	49%	10%
5	1	2	0.005	0%	37%	62%
6	1	3	0.0086	0%	0%	100%

Table 1

Due to availability of starting materials, greater yield, and lack of bi product such as the di-azide, reaction 2 proved to be more efficient in synthesizing the mono-azide compound necessary to improve water-solubility. In reaction B, compound **12** was reacted with TsCl, DMAP, DCM, and Et_3N to give the desired compound **13** in an 82% yield.

3. Ligand Exchange Reactions

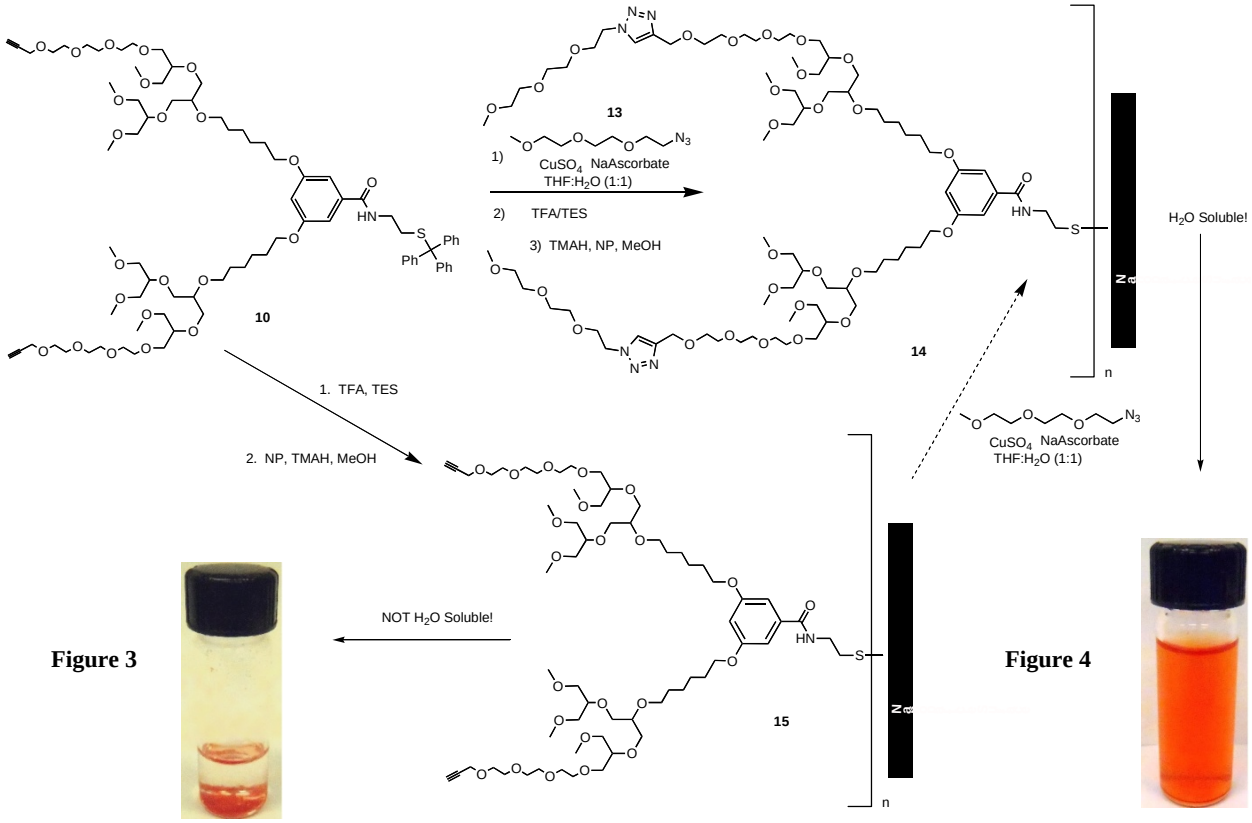

Figure 3

Figure 4

Conclusion

Scheme 3 reactions were successful in creating water-soluble nanoparticles after ligand exchange reactions as proved by the following pictures. **Figure 3** shows that nanoparticles are insoluble after ligand exchange in water before the mono-azide **14** was added, and **Figure 4** shows that after addition of **14** ligated nanoparticles are now soluble in water! Future work includes, but is not limited to, attaching QD's to solid support via 'Click' cycloaddition, adding PEG-azide **14** to remaining alkynes, and finally cleaving from bead used and attaching to a protein.

Acknowledgements

This work was supported by the National Science Foundation CHE-0851505/REU, National Institutes of Health (EB999802 and RR15569), and Arkansas Biosciences Institute.

Experimental Procedures

4

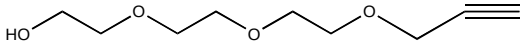

80%

Synthesis of compound 4: NaOH (8.45 g, 0.211mol) was added to a stirred solution of ethylene glycol (100 mL, 0.74mol) and the solution was heated up to 100'C until the NaOH was dissolved, then cooled down to room temperature. Propargylbromide (24 mL, 80% weight in toluene solution, 0.269mol) was added to the solution and warmed up to 45'C. After 1.5-3 hr the reaction mixture was diluted with brine and extracted over ether several times. The ether layer was dried over $MgSO_4$, filtered and concentrated. H NMR (Bruker, 300 MHz, $CDCl_3$), δ 4.18 (d, 2H), 3.72-3.63 (m, 10H, CH_2), 3.60-3.57 (m, 2H, CH_2), 3.61 (s, 1H, OH), 2.42 (t, 1H). [14,15]

5

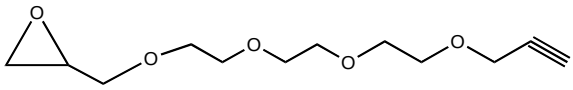

>95%

Synthesis of compound 5: To a stirred solution of **4** (41.29g, 0.219mol), TBAI (6.85 g, 10mol%, 0.019mol) in the 40%NaOH solution (360mL) was added drop wise epichlorohydrin **1** (50mL, 0.637mol). The mixture was stirred at room temperature for 20hr. The reaction mixture was diluted with saturated K_2CO_3. Compound **5** was extracted with ether. The ether solution was dried over $MgSO_4$, filtered and concentrated. ^{1}H NMR (Bruker, 300M Hz, $CDCL_3$), δ 4.18 (d, 2H), 3.79 (dd, 1H, CH), 3.42 (dd, 1H, CH), 3.66 (m, 12H, $6CH_2$) 3.15 (m, 1H), 2.78 (dd, 1H), 2.59 (dd, 1H), 2.41 (t, 1H), ^{13}C NMR (Bruker, 75MHz, $CDCl_3$) δ 79.58, 74.64, 71.86, 70.60, 70.46, 70.28, 70.19, 70.03, 68.98, 58.28, 50.66, 44.16. MS: 245.2 (M^+H), 263.1 ($M^+H + H_2$).

6

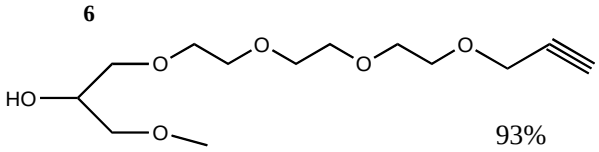

93%

Synthesis of compound 6: Na metal (9.0 g, 0.391mol) was added to MeOH (200 mL, 2.87mol) and stirred until Na was dissolved. **5** (48 g, 0.197mol) was added to the solution then refluxed overnight. The next day, solution was neutralized to Ph 7 with 3 M HCl (100 mL) then **6** was extracted with ether and DCM. ^{1}H NMR (Bruker, 300M Hz, $CDCL_3$), δ 4.20 (d, 2H), 3.95 (m, 1H), 4.19-3.41 (m, 16H, $8CH_2$) 3.37 (s, 3H, CH_3) 2.87 (d, 1H, OH), 2.42 (1, 1H), ^{13}C NMR (Bruker, 75MHz, $CDCl_3$) δ 79.29, 74.55, 73.54, 72.26, 70.26, 70.10, 70.06, 70.03, 69.90, 68.77, 68.59, 58.67, 57.87. MS: 277.2 (M^+H), 299 (M^+Na).

7

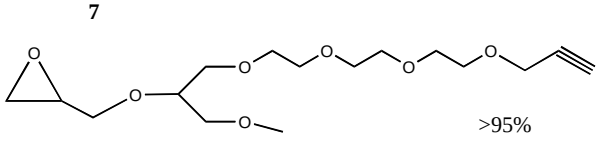

>95%

Synthesis of compound 7: To a stirred mixture of **6** (50 g, 0.181mol) TBAI (5.8 g, 10mol%, 0.16mol), in 40% NaOH solution (450 mL) was added drop wise epichlorohydrin **1** (45 mL, 0.574mol). The mixture was stirred at room temperature for overnight (20hrs). The reaction mixture was diluted with saturated K_2CO_3 solution and **7** was extracted with ether. The ether layer was dried over $MgSO_4$, filtered and concentrated. ^{1}H NMR (Bruker, 300M Hz, $CDCL_3$), δ 4.20 (d, 2H) 3.89 (dd, 1H), 3.71-3.45 (m, 18H, 8 CH_2) 3.36 (s, 3H, CH_3) 3.16 (m, 1H), 2.78 (dd, 1H), 2.62 (dd, 1H), 2.42 (t, 1H).

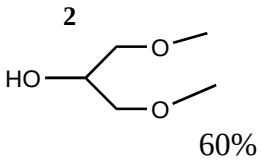

Synthesis of compound 2: To the sodium methoxide solution prepared from absolute methanol (100mL, 1.43mol) and sodium (3 g, 0.130mol) was added epichlorohydrin **1** (4.61g, 0.50mol). The mixture was refluxed for 20 hr under N_2. After, solution was acidified with 3M HCl; the reaction mixture was concentrated under reduced pressure. The insoluble material was filtered and compound **2** was the product. ^{1}H NMR (Bruker, 300M Hz, $CDCL_3$), δ 3.5 (t, 1H, OH), 3.47-3.38 (m, 4H, $2CH_s$), 3.37 (s, 6H, 2 CH_3). [16]

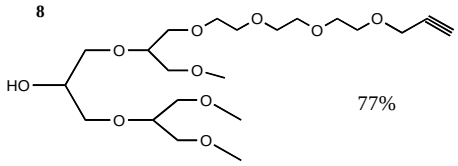

Synthesis of compound 8: NaH (841 mg, 0.035mol) was added to **2** (10 equivalents) and stirred until NaH was dissolved. Compound **7** (7.5 g, 0.233mol) was added to the solution and heated at 65'C overnight. After checking TLC, the reaction mixture was quenched with small amount of water and excess amount of **2** was distilled off. The residue was chromatographed on silica gel to give **8** in 77% yield. ^{1}H NMR (Bruker, 300M Hz, $CDCL_3$), δ 4.20 (d, 2H), 3.95 (m, 1H), 3.71-3.43 (m, 26H, $8CH_2$), 3.35 (s, 9H, $3CH_3$), 2.43 (t, 1H). , ^{13}C NMR (Bruker, 75MHz, $CDCl_3$) δ 79.59, 78.55, 78.46, 74.63, 72.75, 72.68, 72.60, 71.91, 71.87, 71.23, 71.14, 70.72, 70.50, 70.39, 70.29, 69.72, 69.66, 68.96, 59.10, 58.26. MS: 453.1 (M^+H).

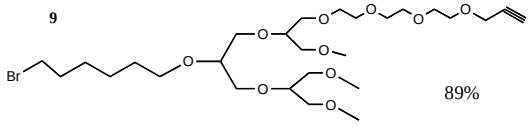

Synthesis of compound 9: NaH was added to a stirred solution of **8** (1.5 g, 0.003mol) in THF (20mL, 0.250mol) and the solution was stirred until NaH (350 mg, 2.2 equivalents, 0.015mol) was dissolved. After 15 minutes, 1,6-dibromohexane was added to the solution and the reaction was stirred at room temperature for 3 days. After checking TLC, solid was filtered off and the solution was concentrated. The residue was purified on silica gel to give **9** (1.63 g, 0.003mol) of 89% yield. . ^{1}H NMR (Bruker, 300M Hz, $CDCL_3$),^{1}H NMR (Bruker, 300M Hz, $CDCL_3$), δ .4.15 (d, 2H), 3.64-3.3 (m, 31H, 8 CH_2) 3.30 (s, 9H, 3 CH_3), 2.4 (t, 1H). 1.80 (m, 2H), 1.51 (m, 2H), 1.34 (m, 4H), ^{13}C NMR (Bruker, 75MHz, $CDCl_3$) δ 79.61, 78.35, 78.23, 78.18, 77.65, 77.22, 76.80, 74.65, 72.58, 72.55, 72.51, 72.48, 70.97, 70.94, 70.78, 70.57, 70.54, 70.48, 70.35, 70.16, 70.11, 69.03. MS: 617 (M^+H).

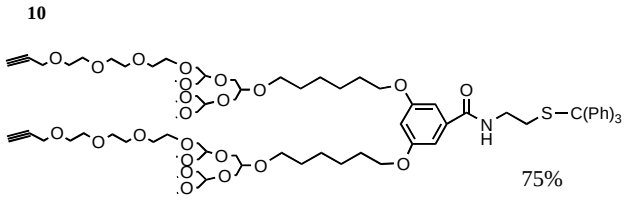

Synthesis of compound 10, 3G Ligand: To the protected thiol (0.673 g, 0.002mol) was added 0.50 g (0.004mol) K_2CO_3 and 0.15g (0.0006mol)18-crown-6. 2.0 g **9** (0.003mol) in 40 mL acetone was added to reaction mixture. Solution was refluxed at 75'C over night (16 hours). The reaction mixture was then concentrated, redissolved in DCM, filtered and concentrated in vacuuo. The resulting residue was purified by flash chromatography with silica 1:99 MeOH:EtOAc to give **10** in 75% yield as a tan oil.

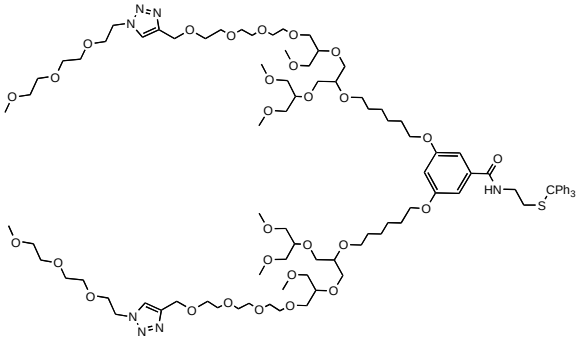

Synthesis of 14: $CuSO_4$ (0.0086 g) and Sodium Ascorbate (0.0137 g, 0.00007mol) were added to a vial followed by **10** (0.25 g, 0.0002mol) and **13** (0.0653 g, 0.003mol). To this mixture was added 1:1 THF/H_2O (8 mL). The vial was capped and heated at 50'C for 3 days. After TLC check, **14** was diluted with 10 mL saturated NH_4Cl then extracted with EtOAc, dried over $MgSO_4$, filtered, and concentrated to give 0.2603 g of **14** of 79% yield. This was used without further purification.

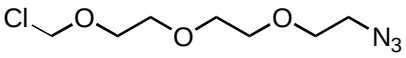

49%

Synthesis of chloroazide: For reaction **A**, to a stirred solution of **11** (11.52 g, 0.062mol) was added DMF (30 mL, 0.390mol) until dissolved. To the mixture was added NaN_3 (1.0g, 0.015mol) and TBAB (0.51g, 0.002mol). Solution was purged with N_2 and stirred over night at 80'C. Mixture placed under vacuum and then extracted with ether and dried over $MgSO_4$ and condensed to give rise to **13** (5.75g, 0.026mol).

13

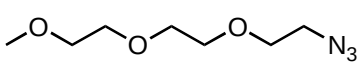

82%

Synthesis of monoazide: For reaction **B**, to a stirred solution of **12** (5.0 g, 0.030mol) was added DCM (50 mL, 0.780mol). To this was added Et_3N (7.7 g, 0.076mol) then DMAP (0.4 g, 0.003mol), and finally TsCl (11.5 g, 0.061mol). The reaction mixture was capped and stirred over night. Next, the solution mixture was washed with DCM and was dried over $MgSO_4$, filtered and concentrated. After checking TLC, residue was chromatographed on silica gel to give rise to **13** (8.70 g, 0.046mol) with yield of 82%.

General synthesis for ligand exchange: To the protected thiol was added trifluoroacetic acid (TFA)1.5 mL per 100 mg ligand, and triethlsilane (TES) 0.1 mL per 100 mg ligand. After 30 min stirring, the reaqction mixture was concentrated and dried. To the residue was added 3 mL of MeOH and basified to pH>10 with tetrabutylammoniumhydroxide. This was added to the semipurified nanoparticles in 2:1 w/w and refluxed 16 hours. The resulting red solution was centerfuged to remove insoluble particles and purified by dialysis (nominal 2000) in MeOH.

References

(1) Feynman, R. *Eng. Sci. (CalTech)* **1960**, *23*, 22.

(2) Michalet, X.; Pinaud, F. F.; Bentolila, L. A.; Tsay, J. M.; Doose, S.; Li, J. J.; Sundaresan, G.; Wu, A. M.; Gambhir, S. S.; Weiss, S. *Science* **2005**, *307*, 538.

(3) Worden, J. G.; Dai, Q.; Shaffer, A. W.; Huo, Q. *Chem. Mater.* **2004**, *16*, 3746.

(4) Worden, J. G.; Shaffer, A. W.; Huo, Q. *Chem. Commun* **2004**, 518.

(5) Cardona, C. M.; Jannach, S. H.; Huang, H.; Itojima, Y.; Leblanc, R. M.; Gawley, R. E.; Baker, G. A.; Brauns, E. B. *Helvetica Chimica Acta* **2002**, *85*, 3532.

(6) Sung, K.-M.; Mosley, D. W.; Peelle, B. R.; Zhang, S.; Jacobson, J. M. *J. Am. Chem. Soc.* **2004**, *126*, 5064.

(7) Howarth, M.; Liu, W.; Puthenveetil, S.; Zheng, Y.; Marshall, L. F.; Schmidt, M. M.; Wittrup, K. D.; Bawendi, M. G.; Ting, A. Y. *Nat. Meth.* **2008**, *5*, 397.

(8) Battaglia, D.; Peng, X. *Nano Letters* **2002**, *2*, 1027.

(9) Li, J. J.; Wang, Y. A.; Guo, W.; Keay, J. C.; Mishima, T. D.; Johnson, M. B.; Peng, X. *J. Am. Chem. Soc.* **2003**, *125*, 12567.

(10) Li, L. S.; Pradhan, N.; Wang, Y.; Peng, X. *Nano Letters* **2004**, *4*, 2261.

(11) Peng, Z. A.; Peng, X. *J. Am. Chem. Soc.* **2000**, *123*, 183.

(12) Peng, Z. A.; Peng, X. *J. Am. Chem. Soc.* **2002**, *124*, 3343.

(13) Bos, J. L. *Cancer Res.* **1989**, *49*, 4682.

(14) Diot, J.; Garcia-Moreno, M. I.; Gouin, S. G.; Mellet, C. O.; Haupt, K.; Kovensky, J. *Org. Biomol. Chem.* **2009**, *7*, 357.

(15) Brunet, J.-J.; Chu, N.-C.; Rodriguez-Zubiri, M. *Eur. J. Inorg. Chem.* **2007**, *2007*, 4711.

(16) *Bull. Korean. Chem. Soc.* **2006**, *27*.

Methods towards Thiazolium Salt Rearrangements

Rebecca Foos, John Brown University
Siloam Springs, Arkansas

Abstract

Much of research within organic chemistry surrounds the methods of pharmaceutical development. The compound thiazole is considered to be a favored structure in many drugs, and as such methods by which it may be used synthetically are of great interest. This study develops the chemical rearrangement of an n-allyl substituted thiazole to a terminal alkylene chain at the beta carbon. Although the study is ongoing, successful rearrangement has been observed with yields up to 38%.

Figure 1. Full desired synthesis reaction scheme, begun with a thiazole and producing an Ireland-Claisen type rearrangement.

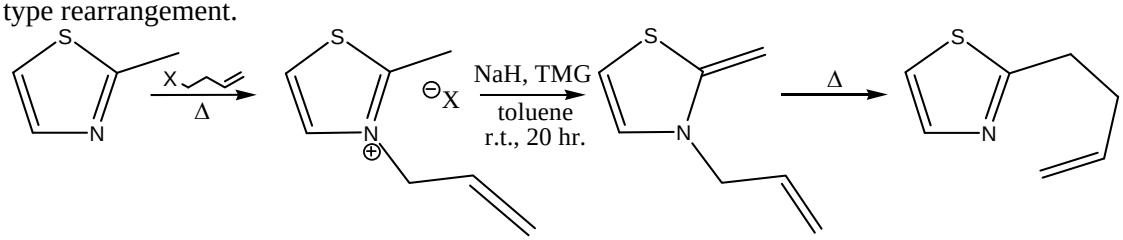

Introduction

Thiazole is known as a “privileged” structure in the chemi-pharmaceutical world due to its heavy use in drug syntheses. Fig. 2 shows several such drugs. Of course any drug of like these takes many synthetic steps to produce. For this reason, the synthetic rearrangement developed in this study (Fig. 1) is of great practical value in the field of pharmaceutical development, as it may be used in further synthetic studies for drug development.

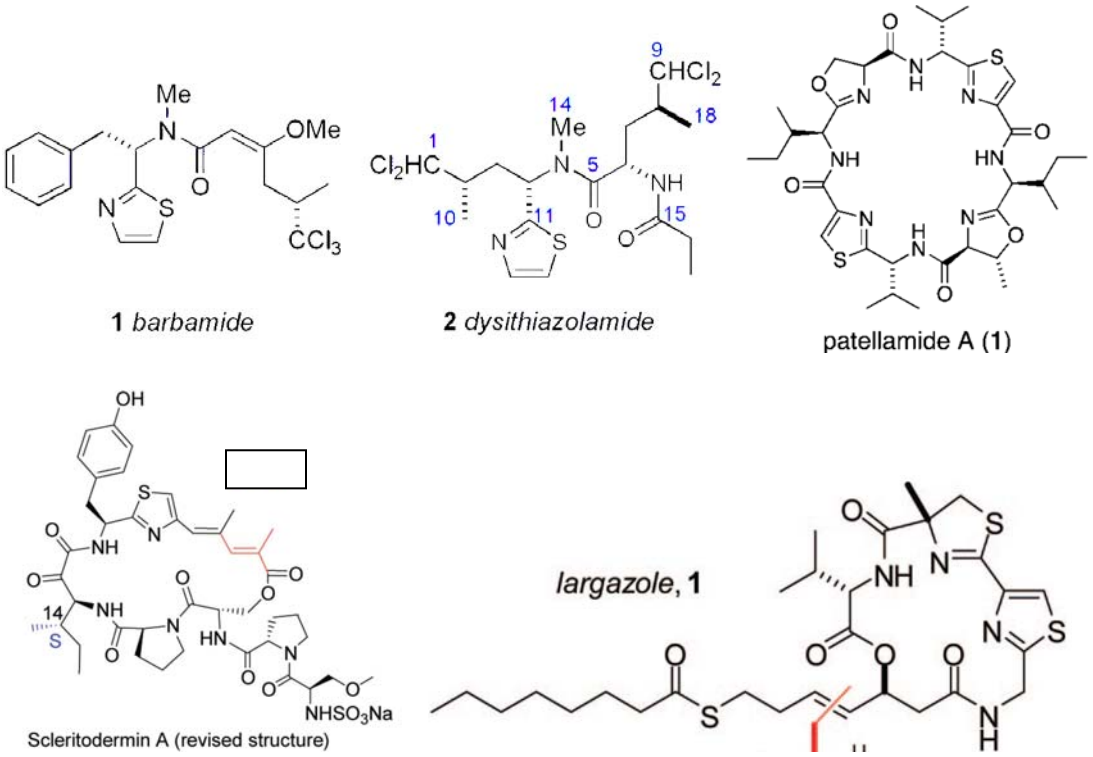

Figure 2a-e. Pharmaceutical examples of the repeated occurrence of thiazole base structure in drugs.

A close predecessor to the target rearrangement **1** is found in the Kurth reaction of the 1980s, which saw the same rearrangement with an oxygen replacing the sulfur.[I]

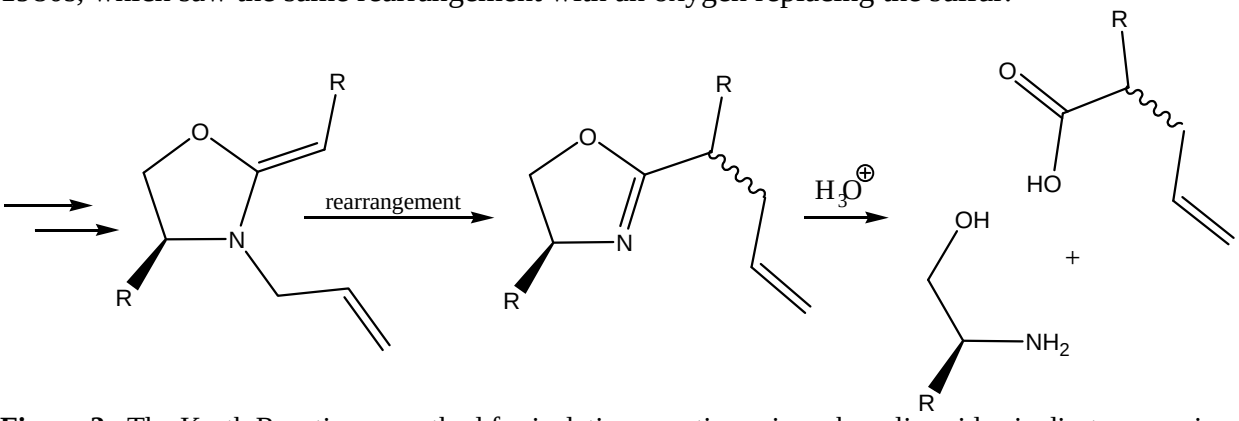

Figure 3. The Kurth Reaction, a method for isolating enantiomeric carboxylic acids via diastereomeric properties of the rearrangement product; scheme shown depicts only steps 3 and 4.

However, this reaction was not intended for pharmaceutical application, but instead served as a method towards enantiomerically selective production of a carboxylic acid via separation of the intermediate diastereomers. While stereochemistry could play a small role and has the potential to be exploited within this synthesis, this falls beyond the scope of this preliminary study.

Experimental Procedures

The first step in the rearrangement synthesis is the formation of the base salt (see Fig. 4). By heating the thiazole system to 120°C with an allylic electrophile for up to five hours, the salt is formed with up to 86% effectiveness. We favored the use of allyl tosylate, as the resulting anion has a low nucleophilicity and will not encourage side reaction. (Allyl tosylate is not commercially available, but was easily be synthesized by sodium hydroxide activation of an allyl alcohol in the presence of tosyl chloride at 0°C in ether.[II]) Purification of the allyl-thiazolium tosylate salt via trituration in ether to remove excess allyl tosylate and dehydration under high vacuum gave high purity as seen in NMR analysis.[III]

Figure 4. Reaction scheme showing the formation of the base thiazole salt. X=Br, OTS

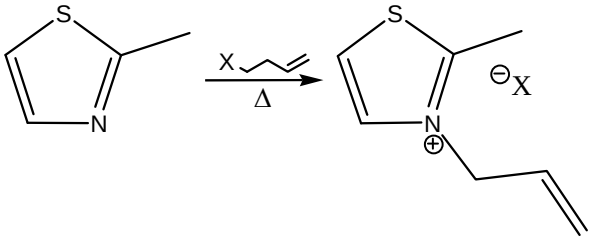

Following the salt formation, activation by base at the beta carbon by sodium hydride gives the ketene acetal intermediate, which upon heating spontaneously rearranges.

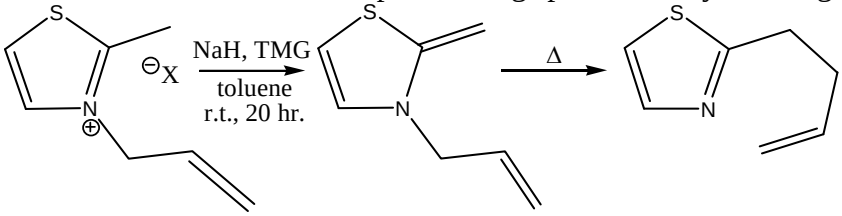

Figure 5. Rearrangement scheme.

This process, without the interference of an allyl group, has been previously developed in very complex systems giving suitably stable rearrangement products; however, there is a known side product which must be avoided.[IV] Fig. 6 shows the process known as dimerization, which gives an observed side product within the intended synthesis, a dimer of the original salt.

Figure 6. When not isolated from each other, the unreacted salt and activated ketene-acetal will react to form a dimer of the original salt.

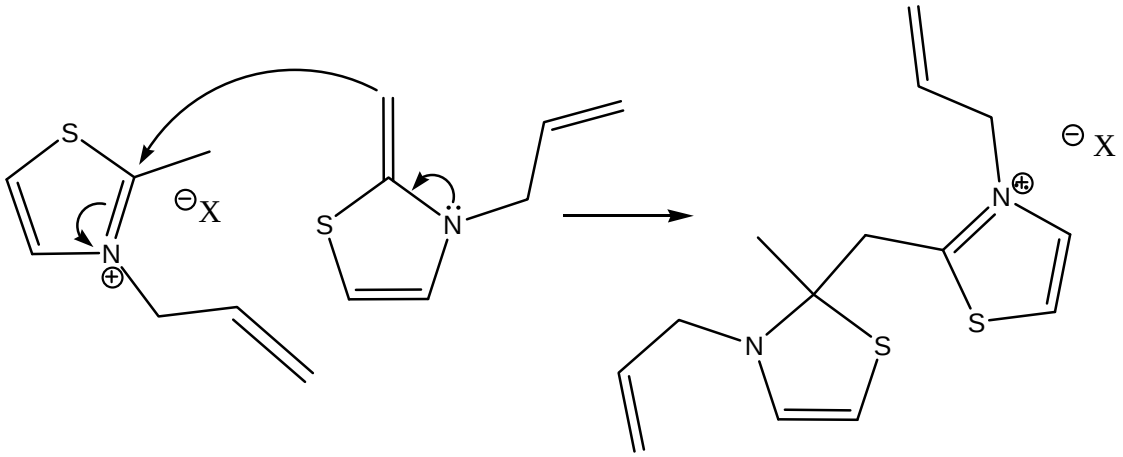

The side reaction may be avoided via very high dilution of the reaction mixture, which essentially serves to isolate the formed ketene acetal from the unreacted salt. This may be achieved in two ways:

1) by adding the salt in solution very slowly by syringe pump to a hot reaction mixture, which will presumably allow the ketene acetal to immediately rearrange upon formation, with low enough concentration that it will not kinetically be able to react with any unreacted salt

2) by using a solvent in which the salt is insoluble, thereby limiting the presence of salt with ketene acetal in solution by the innate solubility of the salt.[V] This second process also allows for complete reduction to the ketene acetal and subsequent heating to drive the rearrangement in a two step process, giving a bit more control and observability.

Via the second method, the procedure for the total rearrangement becomes rather straightforward. The salt is placed in toluene in a pressure tube to prevent the toluene from boiling off during heating. Sodium hydride (1.5 eq.) and tetramethyl guanidine (TMG, 8 eq.), a base facilitating the proton transfer, are added to the solution and the ketene acetal is formed at room temperature over a period of 20 hours.

At twenty hours, the reaction is placed in an oil bath and heated to 170 C for 2 hours. Purification via extraction in ether and column chromatography gives the final pure rearrangement product, verified by Nuclear Magnetic Resonance (NMR) Spectroscopy (see Fig. 7).

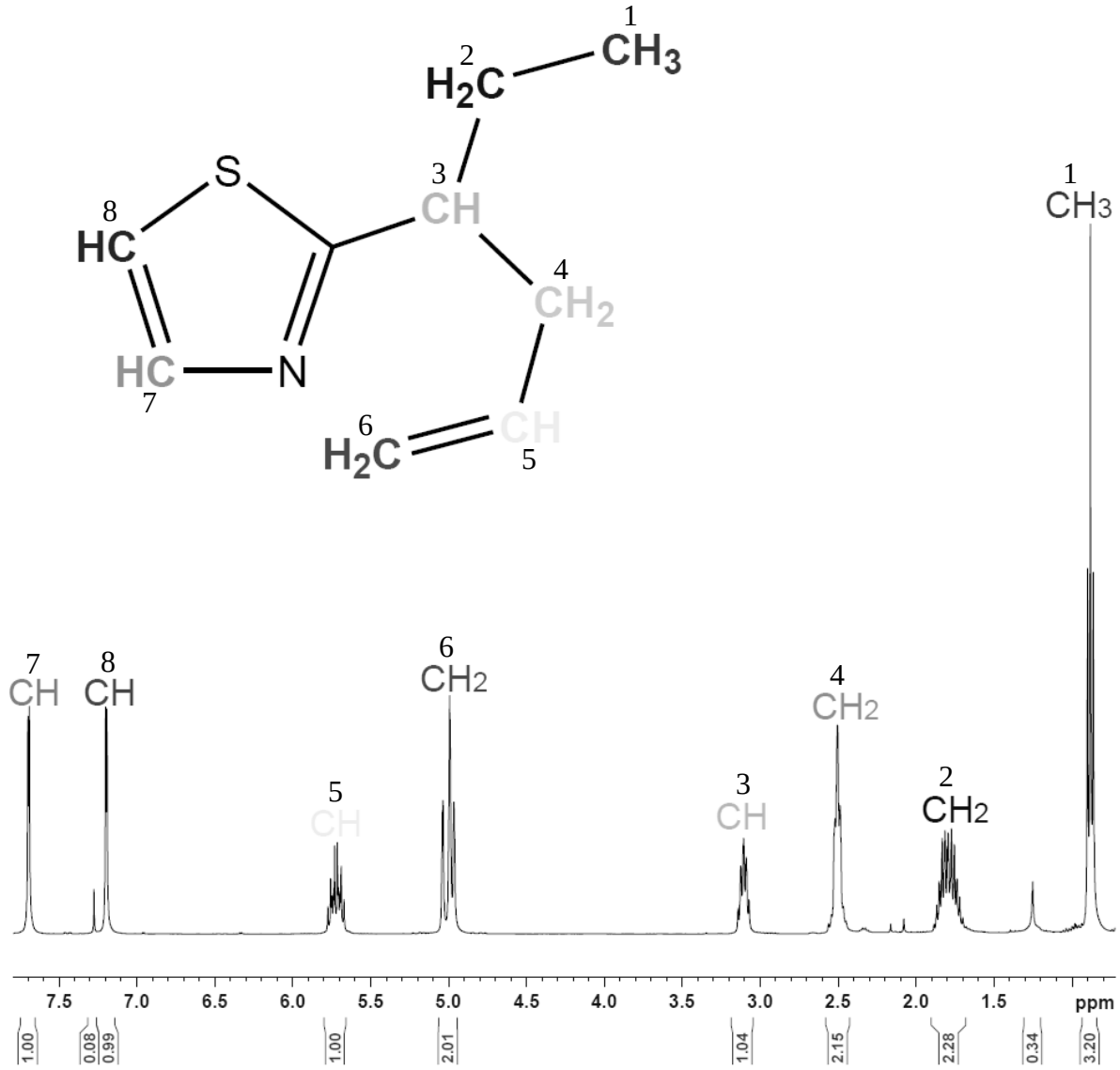

Figure 7. NMR spectra of displayed product system; the numerical peak assignments match the assigned protons, as determined by theoretical NMR shift and splitting prediction.

The clean spectra detailed above shows the purity of the rearrangement product at above 90%. This particular reaction gave a yield of 38%, which in the initial stages of development is rather high. My 2-methylbenzothiazolium rearrangement **8** gave 70% yield with above 90% purity, and more recent yields done by Silvana Dormi have given yields as high as 90% with good purity.

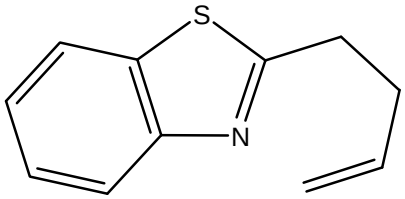

Figure 8. 70% yield benzylated thiazole rearrangement system.

Conclusion

While the progress within this study has been very exciting, work has yet to be done. Since my project ended, we have been looking into a few things. The main barrier towards this rearrangement appears to be the formation of the ketene-acetal, as rearrangement on heating by simulated studies would appear completely favorable. Hindrances to this step which we have examined are the high excess of TMG. As this was part of a procedure referenced when developing the study, we began with the prescribed 8 equivalences. However, recent time trials have shown that a lower amount, just two equivalences, gives a more stable and complete conversion to the ketene-acetal. This mini-study also tested the effectiveness of letting the conversion occur over 20 hours, which indeed proved the most complete method, although the majority of the salt had reacted within the first hour.

Further study will include labeling of the terminal rearrangement carbon via a methyl group or some such analogous inert functional group to check positively that the mechanism is indeed a rearrangement and not simply a electrophile/nucleophile intramolecular reaction. Following this confirmation, more complex systems will also be examined for the effective use of this rearrangement.

Acknowledgements

I would like to thank Dr. McIntosh for his support and guidance, and for making room for me in his busy lab. I would also very much like to thank Silvana Dormi, my “director of operations,” as she brought me into this project and worked alongside me to realize this rearrangement.

My thanks also to the University of Arkansas, the National Science Foundation NSF-REU CHE-0851505, NSF CHE-0911638, the National Institute of Health NIH RR-1569, and the Arkansas Biosciences Institute.

References

1. *Asymmetric Induction in the Claisen Rearrangement of N-Allylketene N,O-Acetals* Kurth, M. J.; Decker, O. H. W.; Hope, H.; Yanuck, M. D. *J. Am. Chem. Soc.* **1985**, *107*, 443-448

2. Allyl tosylate synthesis from: *Stereoselective Isomerisation of N-Allyl Aziridines into Geometrically Stable Z Enamines by Using Rhodium Hydride Catalysis* Tsang, D. S.; Yang, S.; Alphonse, F. A.; Yudin, A. K. *Chem. Eur. J.* **2008**, *14*, 886-894

3. Various salt syntheses giving benzothiazolium salt synthetic procedure: *Computer Aided Benzothiazole Derivatives. Synthesis, Structure and Biological Study of New Push-pull Conjugated Benzothiazolium Salts* Buffa, R.; Zahradnic, P.; Foltinová, P. *Heterocyclic Communications* **2001**, *7*, 331-336

4. For complex system ketene-acetal generation and isolation, see: *Generation of Cyclic Ketene-N,X-Acetals (X=O,S) from 2-Alkyl-1,3-oxazolines and 2-Alkyl-1,3-thiazolines. Reactions with Acid Chlorides, 1,3-Diacid Chlorides and N-(Chlorocarbonyl) Isocyanate* Zhou, A.; Pittman, C. U. *Synthesis* **2006**, *1*, 37-48

5. Pseudo dilution via insolubility to prevent dimerization found in: *Isolation of Monomeric Methylene Bases Derived from Benzothiazolium Quaternary Salts* Owen, J. R. *Tetrahedron Lett.* **1969**, *32*, 2709-2712

Fluid Motion with Magnetohydrodynamics

Amanda Hicks, John Brown University
Siloam Springs, Arkansas

Abstract

The fundamentals of redox magnetohydrodynamics in a magnetic field parallel with the plane of the electrode array are investigated in a confined solution. A parallel magnetic field was created from two small permanent magnets held a few centimeters apart, creating a magnetic field between them parallel to the chip. Electroactive potassium ferri- and ferrocyanide were reduced and oxidized at the electrodes in order to create ion flux. The cross product of the parallel magnetic field and the ion flux produces the magnetohydrodynamic force, which makes the fluid flow across the electrodes rather than around them as has been previously observed with a magnetic field perpendicular to the array. Observed velocities changed depending on the depth of the cell, the height within the cell that the velocity was measured at, and the current being used. The fluid moves in four horizontal circulations, moving in opposite directions over the working and counter electrodes and being pulled back around the sides of the electrode to replenish the flow.

Introduction

There are many applications in microfluidics for MHD. The ability to move fluid without the use of moving parts and the ability to switch directions very quickly makes it attractive for use as a pump, which could be used for PCR, integrated microfluidic/NMR systems, or other devices. MHD would also be useful for mixing within a small, confined volume where traditional methods cannot be used. This paper demonstrates a pattern of four adjacent circulations in the same plane which would be particularly useful for this.

Magnetohydronamic, or MHD force ($\mathbf{F_B}$) is defined by the rule $\mathbf{F}_B = \mathbf{j} \times \mathbf{B}$. The force is created by cross product of the ion flux **j** and the magnetic field **B**. What this force affects is the fluid containing the ions, and the fluid moves in the same direction as the force. The directions of each can be worked out using the right-hand rule; by pointing the fingers of the right hand in the direction of B, and curling them into j, the thumb will point in the direction of the force.

In addition, using a redox species, here potassium ferri and ferrocyanide, eliminates some of the traditional problems with using MHD, keeping electrodes from being destroyed by oxidation and preventing electrolysis of water, which forms bubbles that hinder flow.

Previous small volume, chip-based studies have been performed with the magnet below the chip, creating a magnetic field perpendicular to the plane of the chip. The study describe herein differs in that it uses a pair of magnets held on either side of the chip to create a magnetic field parallel to the plane of the chip. This is at a right angle to a different part of the ion flux than has been previously studied. Unlike where with the perpendicular field, the edge effects were what was observed, the primary force in these studies will be caused by the ion flux going vertically in and out of the electrodes, which will cause the fluid to move differently, going across the electrode instead of around it in circles.

Experimental Procedures

Chemicals and materials. All chemicals were reagent grade and used as received. Solutions were prepared using bottled deionized water from Ricca Chemical Company. Potassium ferricyanide was purchased from EM Science (Gibbstown, NJ), and potassium ferrocyanide trihydrate was purchased from J. T. Baker (Phillipsburg, NJ). Potassium chloride was bought from EMD (Gibbstown, NJ). Polystyrene latex microspheres (10 μm diameter, 2.5 wt% dispersion in water) were acquired from Alfa Aesar (Ward Hill, MA). Sylgard 184 silicone elastomer base and curing agent, used to make the polydimethysiloxane (PDMS) gaskets, were obtained from Dow Corning Corporation (Midland, MI). Precleaned microscope slides (3 in. by 1 in. by 1.2 mm) were bought from VWR. Metal deposition on the chips was carried out using a chromium-plated tungsten rod (Kurt J. Lesker Co., Clairton, PA), and fragments cut from a gold coin (Canadian Maple Leaf, 99.99%) placed in a molybedenum boat (Kurt J. Lesker Co., Pittsburgh, PA) for evaporation, and all chips were based on silicon wafers (125-mm diameter, 600-650 thickness, and (100) orientation) with 2-μm, thermally-grown SiO_2, purchased from Silicon Quest international. Benzocyclobutene, BCB, (Cyclotene 4024-40) was acquired from Dow Chemical Company. Electrical connection of the potentiostat to the contact pads on the chip used an edge connector from Sullins Electronics Corp. (San Marcos, CA).

Chip design. Gold electrodes were patterned onto silicon wafers and diced. Fabrication was performed by others in our laboratory and will be describe in a susequent paper. The general procedure for fabrication of a different chip design can be found in Ref [1]. Each chip is 1.2 cm long and 5 cm wide, and has nine individually-adressable large electrodes. All electrodes are 2 mm long, and 3200, 2000, 800, 200, or 25 μm wide, with gaps of 1 mm between all except between the 3200 μm and 2000 μm electrodes. The chip is symmetrical around the 25 μm electrode. In the magnetic field, the field is parallel to the 2000 μm side of the electrodes.

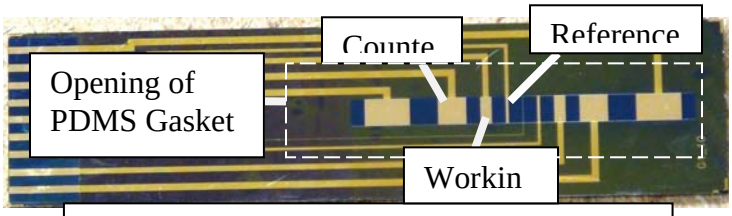

Figure 1: photograph of the chip used.

In general, the 800 μm electrode closest to the leads was used as the working electrode, with the 2000 μm electrode 1000 μm away used as the counter, and the 200 μm electrode located 1000 μm away on the other side was used as the reference. See Figure 1.

Magnetic Field. The parallel magnetic field setup consisted of two 0.5 T NdFeB sintered permanent magnets (Amazing Magnets, Irving, CA) measuring 1 inch across and 0.25 inches thick placed 2.3 centimeters apart, creating a field of 0.27 T at the center. The magnets were held apart at that distance by a low carbon steel u-bar measuring 10 cm on each side and 2.5 cm thick, with a cutout 7.5 cm long and 3.5 cm wide. The magnetic field was measured with a DC magnetometer (Gauss) from AlfaLab Inc.

Because of the relatively small size of the magnets in relation to the chip, the magnetic field was not even across the chip. The working electrode was always placed in the same spot in the very center of the magnetic field in order to ensure that the force would be consistent so the measured velocities would not change.

Experimental setup. A PDMS film with a rectangular opening measuring 2.8 by 0.7 cm cut into it was placed on the chip, with the opening exposing all electrodes over the entire chip. This gap was then filled with the solution that contained the redox species, the electrolyte, and the microbeads. A piece of a glass microscope slide was then placed on top as a lid. This created a closed electrochemical cell, with the thickness of the PDMS defining the depth of the cell. Four PDMS gaskets were used of thicknesses 620 µm, 940 µm, 1250 µm, and 2500 µm.

Because of the density mismatch between the solution and the beads, the beads tended to sink or rise in the cell, so every experiment required a fresh solution. Replacing the solution also involved washing the chip, the PDMS film, and the glass slide with deionized water, then drying the chip with either N_2 gas or argon purchased from Airgas (Danbury, CT) to blow the liquid off of it. The PDMS and glass slide were dried with kimwipes purchased from Kimberly-Clark Global Sales, Inc (Roswell, GA). Occasionally the chip was also rinsed with ethanol from Pharmco-Aaper (Brookfield, CT) in order to prevent electrode fouling.

Movement of the microbeads was observed with a Leica DM 2500M microscope outfitted with a Mitutoyo M Plan Apo 10 objective. The movies were recorded using a Sony Handycam HDR-XR500 digital camera (30 frames per second, 1920 x 1080 pixels per frame).

Bead velocities given herein are the average velocity calculated from several, generally four, microbeads. These velocities were determined by how far a bead traveled across the electrode, using the width of the electrode as the scale, over a period of 10 s, determined by the number of video frames that had passed. A frame was captured once every thirty frames, or once per second, and the velocity measurements were calculated from these. All measurements were taken 5 s after the current was first applied to ensure uniformity of the data. No movement was observed in experiments without a current or a magnet present that could not be attributed to density gradients.

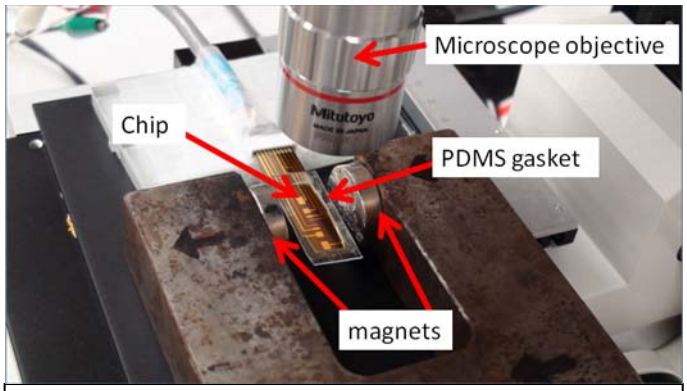

Figure 2: Photograph of setup showing magnets, chip, and PDMS gasket on microscope stage.

Electrochemical Control. A CHI 760B potentiostat (CH Instruments, Austin, TX) was used for chronopotentiometry and chronoamperometry in three-electrode configuration. For most experiments, the working electrode was 800 µm wide by 2000 µm long, and it was 1000 µm away from the counter electrode, which was 2000 by 2000 µm. The reference remained on the other side of the working electrode from the counter, again 1000 µm away, and was 200 µm wide by 2000 µm long. All solutions were 0.07 M $K_3Fe(CN)_6$, 0.07M $K_4Fe(CN)_6$, and 0.1 M KCl unless otherwise specified, with either a 25X or 50X dilution of microbeads added while the solution was being made as to not change the dilution of the other species.

A cathodic current of 30 µA was used for all experiments unless otherwise specified. This current was chosen for the experiments because it is below the diffusion limited current, and thus will not damage the electrodes or cause electrolysis of water, which would cause bubbles that would hinder flow, but high enough to see a substantial amount of bead movement.

Results and Discussion

Characterization of the electrodes. In order to assure that all electrodes were working, electrodes were initially characterized using Cyclic Voltammetry (CV) before being used. Figure 4 shows examples of CV responses for the 3 electrodes used in these studies. The peak current for a range of 0.5 v to -0.5 v in .07M ferri/ferrocyanide is 270 µA at the 800 µm working electrode. The calculated value for this current using $i_p = (2.69 \text{ X } 10^5)n^{3/2}AD_o^{1/2}C_o^*r_o$ is 525 µA. The reason for this inconsistency is unknown, but has been observed consistently over several chips and electrode sizes.

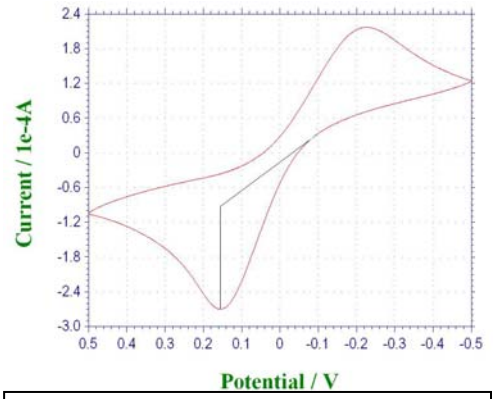

Figure 4: Cyclic Voltammogram of the 800 µm electrode.

Chronoamperometry was used to determine the safe current limit for the electrodes. The 800 µm working electrode gave a current of 38.4 µA over 40 s, which is how the current most often used at 30 µA was obtained.

Does the bead velocity change over time?

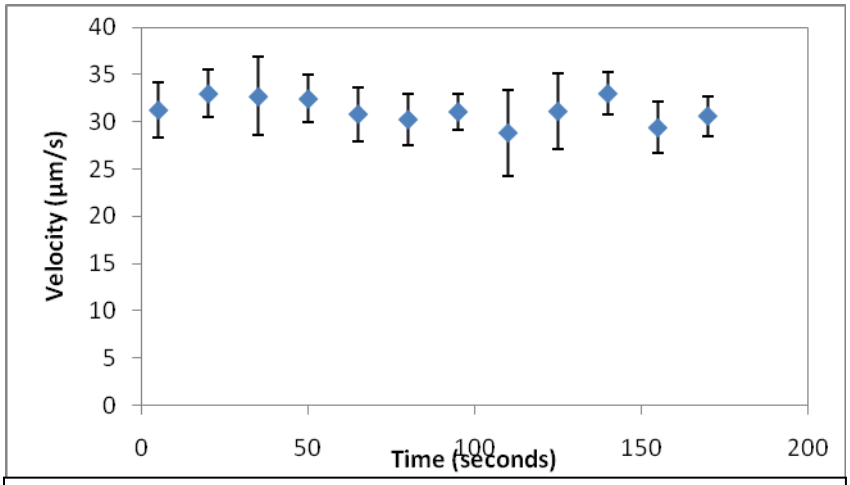

Figure 5: Graph of bead velocity over about three minutes, in a 640 µm deep PDMS gasket at a measured height of 480 µm.

The bead velocity remains constant over time as seen in Figure 5. Although there are minor variations in the data, the F value of an ANOVA test was 0.816, proving all the points to be equal within the 95% confidence level. This makes sense, given the $\mathbf{F}_B = \mathbf{j} \times \mathbf{B}$ rule. If the ion flux is held constant, and the magnetic field is constant, the force and therefore the velocity should not change unless one of the other two variables does, regardless of the duration of the experiment.

It therefore does not matter when during the course of experiment velocities are taken, as long as it is before the redox species in the solution is exhausted, thus preventing current from flowing. The only other condition on time is when the beads, due to the density mismatch of the solution, sink to the bottom of the cell or rise to the top and stick.

Does it match the theory?

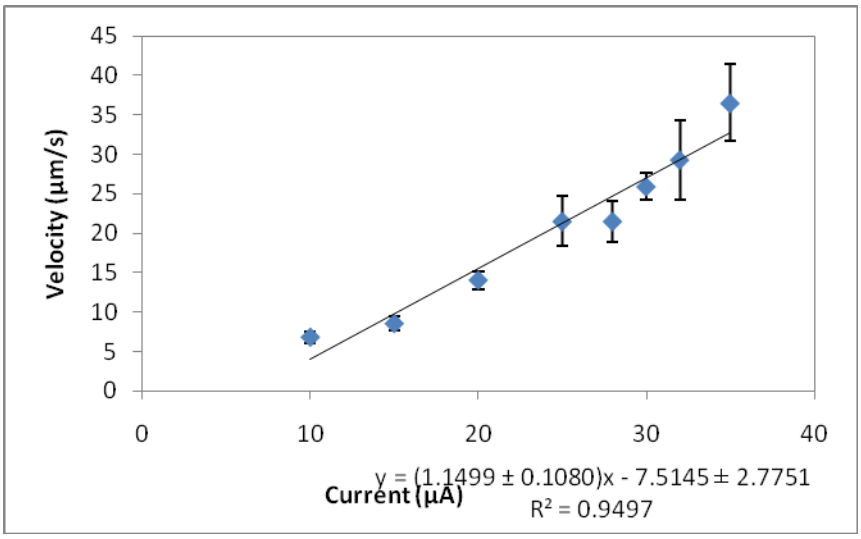

Figure 6: Graph of bead velocity versus currents ranging from 10 µA to 35 µA. These experiments were done in a 620 µm deep PDMS, at height of 480 µm, and all velocities were taken five seconds after the current was first applied. These measurements show eight beads per point rather than four.

If **j,** ion flux, is related to **i,** current, then according to $\mathbf{F}_B = \mathbf{j} \times \mathbf{B}$, as current increases in a constant magnetic field, the force should increase in a linear manner along with it. As shown in Figure 6, this is indeed the case, but only from ~15 µA to ~30 µA.

At this time it is unknown why this graph does not go through zero. The R^2 value of 0.95 indicates some deviation from linearity. Using different conditions to try and get a more obvious pattern, linear or otherwise, has been attempted, but without success. It is possible that at lower currents the force is small enough that otherwise minor changes in other variables, such as the

position of the PDMS gasket, the exact position within the magnetic field, or others could change the observed velocity noticeably. At higher velocities, the linear trend is more obvious, but at lower ones, it's very hard to get reproducible results.

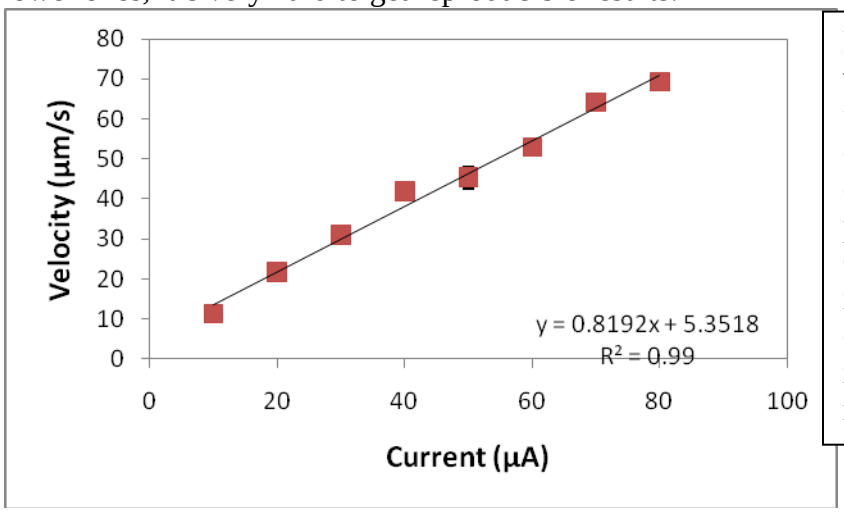

Figure 7: Graph of bead velocity vs currents ranging from 10 µA to 80 µA. This experiment was done using a concentration of 0.1 M potassium ferricyanide and 0.1 M potassium ferrocyanide in order to allow higher currents to be used, and done in a 620 µm deep PDMS, with measured height of 320 µm.

The trend continues to be linear as current increases in Figure 7, showing that **i** is related to **j.** As this figure shows, using higher currents gave a much straighter graph than the original low-current experiment did. However, it still does not go through zero. There may be a factor affecting the velocity that we are not taking into account that explains this, but it is unknown at this time. More experiments of this type are still being done.

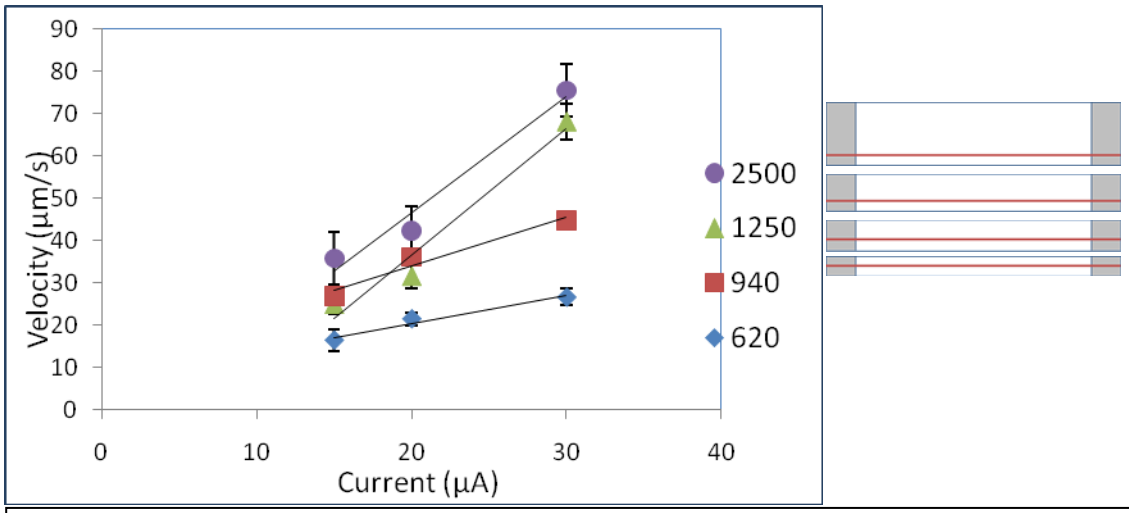

Figure 8: Graph of bead velocity vs current at different PDMS depths. The diagram to the side shows that the measured height was consistent in all depths. The linear equations for 2500, 1250, 940, and 620 µm deep PDMS are as follows:
2500: y = 2.7407x - 8.1321 R^2 = 0.9681 1250: y = 2.9893x - 23.168 R^2 = 0.9641
940: y = 1.1386x + 11.289 R^2 = 0.957 620: y = 0.6561x + 7.3518 R^2 = 0.9653

Figure 8 shows that the depth of the cell similarly does not change the linear trend, although it seems like current might have more of an effect when a deeper PDMS than they do when a shallow one is used. More experiments would be necessary to verify this.

What is the overall pattern in fluid flow? Because the ion flux coming straight up or down off the electrode is perpendicular to the parallel magnetic field, the right hand rule states that the fluid will flow across the electrode in the same plane as the chip, perpendicular to the direction of the magnetic field and in opposite directions over the working and counter electrodes. What was unknown before the start of this project was how the fluid being moved by that force would be replenished.

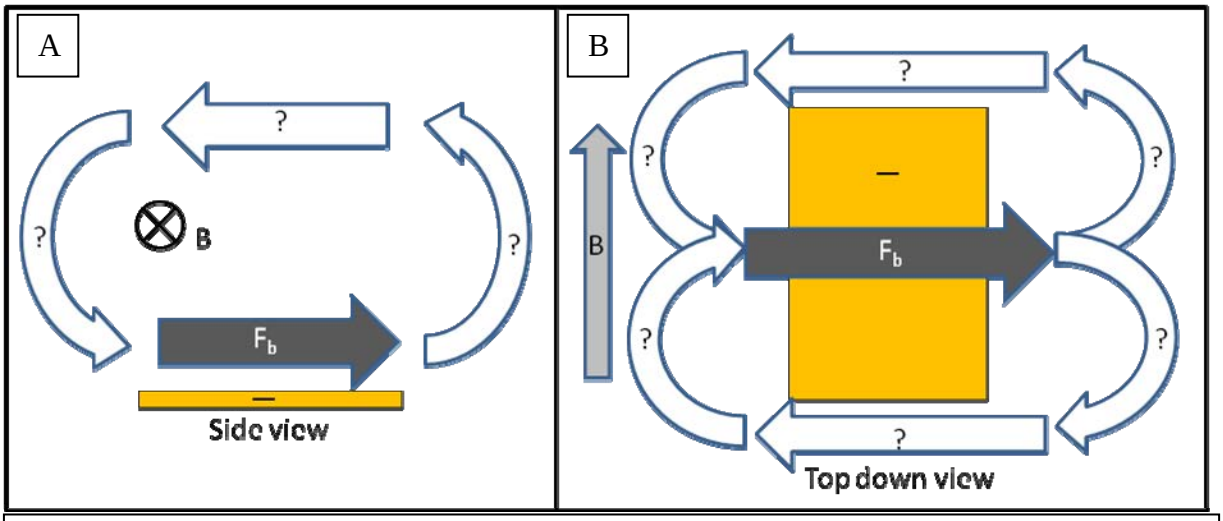

Figure 9 parts A and B: Two possible patterns of fluid movement over the working electrode. The large dark arrows are the force caused by the ion flux near the plane of the electrode, and the white arrows are the two ways in which the flow could replenish itself.

The initial expectation was that the fluid would move according to Figure 9A, where the movement would turn upwards and cycle back around vertically. Fluid here would be fighting edge effects, which would push downward where the fluid would be trying to go upwards and upwards where the fluid needed to go down, but because of the large size of these electrodes, edge effects were thought to be small enough to be easily overwhelmed, especially if the cell height was very high.

The second expectation, shown in Figure 9B, was that the fluid would move around the sides of the electrodes to replenish itself, forming two large circles on the same plane as the chip over each electrode. This pattern would not be fighting edge effects, but would require the flow to split instead of forming a single circle.

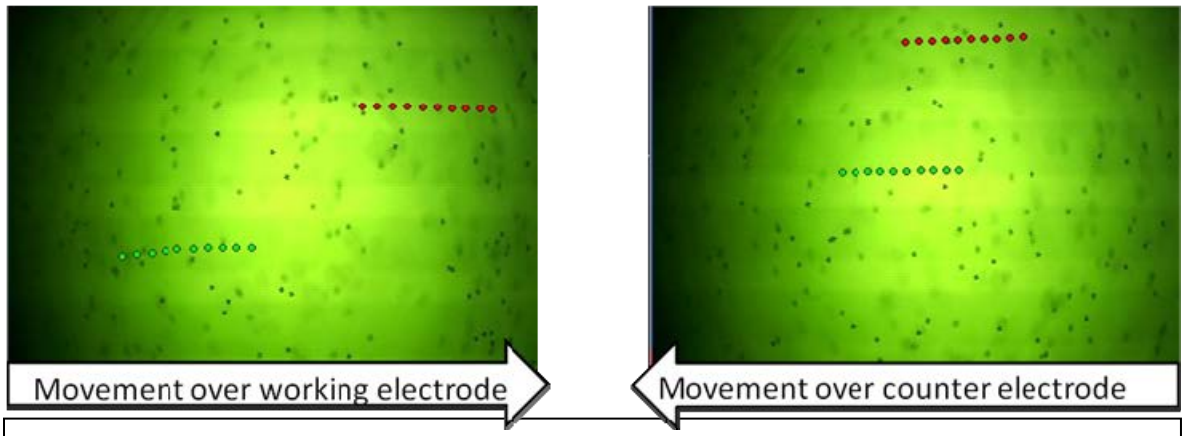

Figure 10: pictures taken over the counter and working electrodes, showing bead tracking and movement direction. These measurements were taken in a 2500 µm deep PDMS gasket, using 0.1 M Ferri/Ferrocyanide, at a current of 100 µA. Rather than an 800 µm working electrode and 2000 µm counter electrode as was used for most experiments, the working electrode had a width of 2000 µm and the counter 3200 µm. Because of the increased speed those changes produced, the tracked beads, seen as outlined dots, here are shown 1/6th of a second apart.

Figure 10 shows the experimentally obtained flows over the working and the counter electrode. There are two of them, moving in opposite directions, as the right hand rule predicted. Regardless of how high or low in the solution where beads speeds are measured, the beads go in the same direction over the electrode. If there were a vertical circular motion, there would be a difference in direction between the top of the solution and the bottom of the solution, but this did not occur. Only horizontal circulations were observed, like those in figure 9B.

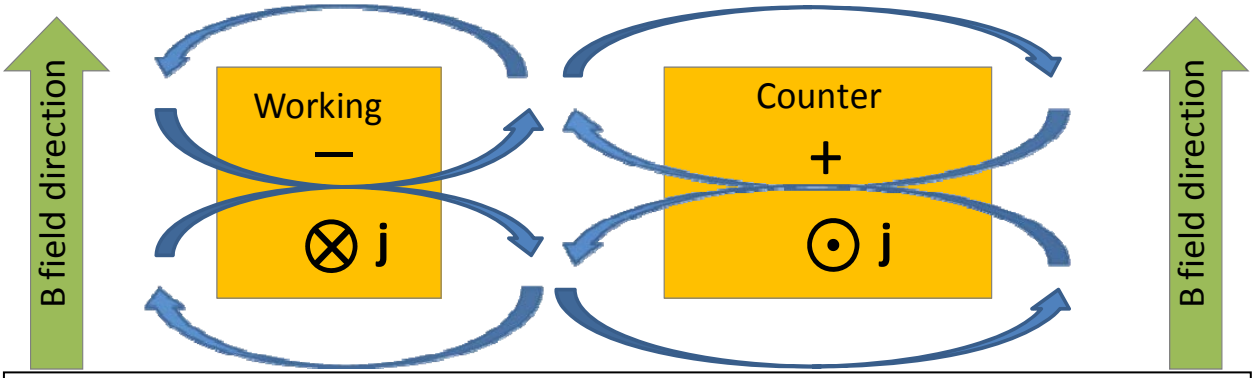

Figure 11: Diagram of observed fluid movement over the working and counter electrodes, viewed from the top down, roughly to scale.

Overall, the fluid forms four large, flat circulations as seen in Figure 11 which meet between the two electrodes and push away from each other. The observed movement is much faster over the electrodes than it is circling back around, though this has not been quantified. The role that edge effects play in any vertical motion, or in keeping this pattern horizontal to the chip, is unknown at this time, largely due to the bead tracking method not be able to measure vertical

motion, and also the inability to differentiate between vertical motion caused by edge effects and that caused by density gradients within the solution. Circulation in the style of Figure 9A was not observed, regardless of the depth of the cell.

Vertical position and gasket height. The effects of changing the cell depth were originally explored to see if the fluid flow pattern could be made to flip around and go back over the electrode to replenish the flow, as seen in Figure 9A. That was not observed; however, large differences in velocity between the different PDMS heights became apparent, as well as differences depending on what height the velocity was measured at.

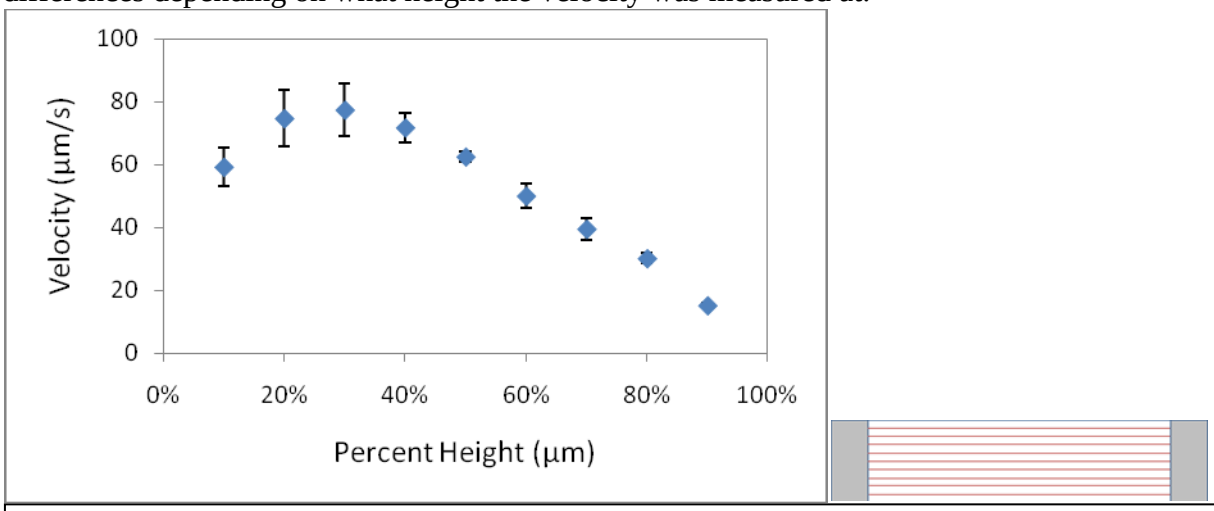

Figure 12: Graph of bead velocity as a function of measured height in the cell. This was taken from a single, very long experiment in a 2500 µm deep PDMS where the height was gradually increased by increments of 320 µm until the lid of the cell was reached. The small diagram to the side shows an approximate cross section of the PDMS, showing where the measurements were taken as red lines.

The velocity reaches a peak when the velocity is taken at around 25% of the total height in a 2500 µm cell depth, as seen in Figure 12. Here, the fluid is outside the no-slip boundary, so resistance is lessened, but the fluid is still relatively close to the electrode providing the force. This has not been tested in other cell depths, but the pattern was reproducible in the 2500 µm cell depth. It's possible that the peak might appear elsewhere in the cell if it were shallower, as the point where the no-slip boundaries least effect the velocity of the fluid flow would change as the ceiling got closer or further away.

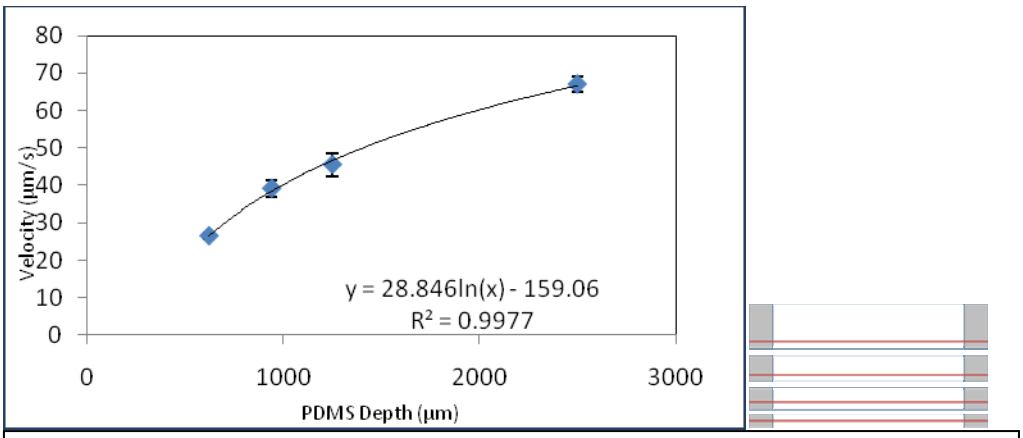

Figure 13: Graph of relative bead velocity as a function of the PDMS depth. These experiments were done at a current of 30 µA. The diagram to the side shows that the measured height was constant regardless of which PDMS was being used.

Increasing the depth of the cell decreases the resistance, as the no-slip boundaries become further and further away from each other, so even at a fixed height within the cell (here 320 µm), fluid moves faster. As the depth approaches infinity it has less and less of an impact, thus the graph begins to level out in a logarithmic fashion.

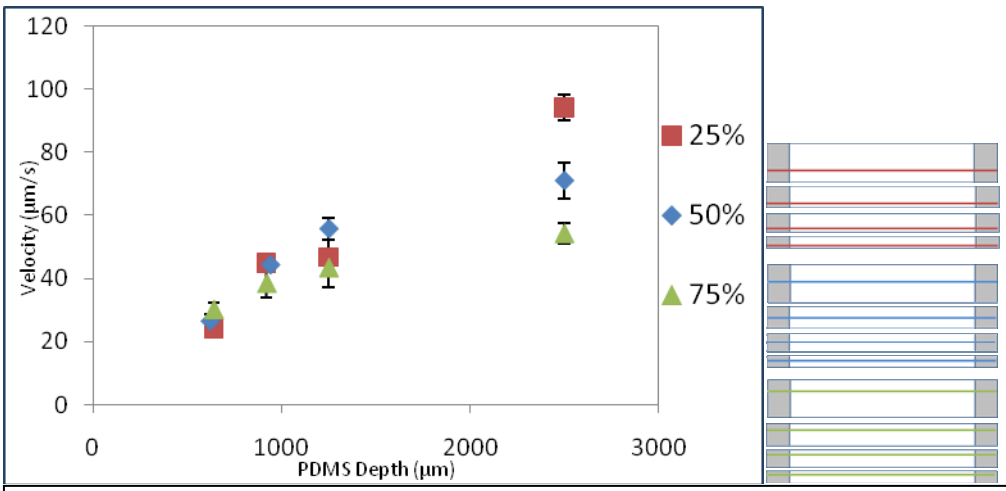

Figure 14: Graph of bead velocity as a function of the PDMS depth measured at a three different percentages of the total height of the cell. The three diagrams to the side show the measured heights for the different

The same trend can be observed when the measured height is a percentage of the total depth, as in Figure 14. Again, the differences between velocities at different heights can be easily seen, with the measurements closer to the electrode tending to go faster. It is also interesting to note how the no-slip boundaries, in the thinner PDMS, keep all velocities very similar. As they get further apart, the beads can speed up as resistance lessens.

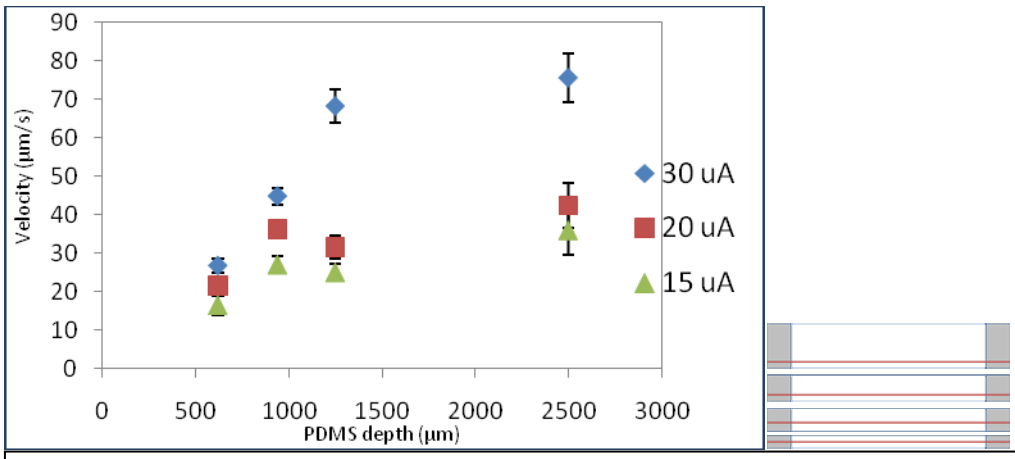

Figure 15: Graph of bead velocity vs PDMS depth at 30 µA, 20 µA, and 15 µA currents.

Even at different currents, the trend of leveling off as the PDMS depth reaches a maximum continues, though at lower currents it seems to make less of a difference.

Conclusions

The velocity of the beads does not change over time as long as the applied current remains constant. This fits the relationship defined by $\mathbf{F}_B = \mathbf{j} \times \mathbf{B}$, in that when neither ion flux nor the magnetic field density changes, the velocity does not change. It also implies that experiments can be taken for very long periods of time without substantially affecting the fluid dynamics.

There is a linear relationship between current and velocity, supporting that ion flux (**j**) is related to current (**i**). What keeps this relationship from being linear through zero is unknown.

The solution goes around the electrodes instead of up and back over the top in order to replenish the flow over the electrode, no matter how deep the PDMS gasket is. Whether this is the result of edge effects keeping the fluid from moving upwards or of something else is currently unknown. The four circulations this produces are attractive for mixing on a small scale, or within enclosed spaces where moving parts cannot be easily used.

The velocity of the beads varies through the height of the solution, reaching a peak at around 25% in a 2500 µm deep PDMS. This is because of the no-slip boundaries at the edges of the cell, which resist movement and therefore slow the fluid flow near the chip, the walls, and the lid. The highest velocity is where the fluid is outside the no-slip boundary, but still close to the electrode providing the ion flux, and therefore the force. This same principle also means that deeper PDMS will have higher velocities, as the gap between the no-slip boundary at the floor of the cell and the one at the lid increases, decreasing resistance throughout the rest of the cell. As cell height approaches infinity, this has less and less of an effect.

These results all add to the fluid manipulation toolkit that MHD has to offer.

Acknowledgements

I thank Ingrid Fritsch, Melissa Weston, Joe Bruton, and the rest of Fritsch research group, Vishal Sahore for chip fabrication, and the National Science Foundation for financial support through grant CHE-0719097 and NSF/REU CHE-0851505.

References

[1] E.C. Anderson, M.C. Weston, I. Fritsch, Investigations of Redox Magnetohydrodynamic Fluid Flow At Microelectrode Arrays Using Microbeads, Anal. Chem., **2010**, *82*, 2642-2651

[2] M.C. Weston, M.D. Gerner, I. Fritsch, Magnetic Fields for Fluid Motion, Anal. Chem., **2010,** *82*, 3411-3418

[3] Qian, S.; Bau, H. H. *Mech. Res. Commun.* **2009**, *36*, 10–21.

Configuration and Geometry of the RWALP15 Transmembrane Peptide in a Lipid Bilayer

Jared Kafader, Elmhurst College
Elmhurst, IL

Abstract

Membrane proteins along with their fundamental peptide-lipid interactions are some of the least understood areas of biochemistry. To answer some of the questions, RWALP15, a short model transmembrane peptide, was synthesized with isotopically labeled residues through solid phase peptide synthesis and analyzed by means of ^{2}H solid-state NMR in various lipid membrane environments such as DLPC (C12:0), DMPC (C14:0), and DOPC (C18:1). The Geometric Analysis of Labeled Alanines (GALA) was used to determine the orientation of RWALP15 in each lipid bilayer. Synthesis confirmation of RWALP15 was determined through MALDI-TOF mass spectrometry and peptide purification was performed by HPLC. The ^{2}H NMR spectra reveal the RWALP15 peptide does in fact have a defined orientation in each of the DLPC, DMPC and DOPC lipid bilayers. Circular dichroism spectra suggest that RWALP15 does contain an α-helix structure in each lipid system, though immensely diminished in DOPC. Fluorescence emission spectra suggest that the anchoring tryptophans are located around the lipid/water interface in DMPC, DLPC, and DOPC. The observed ^{2}H quadrupolar splittings along with the GALA analysis indicate the tilt of RWALP15 to be ~7˚ in DLPC and DMPC bilayers. It is surprising to observe a transmembrane orientation of RWALP15 in DMPC considering that the peptide hydrophobic length appears to be significantly shorter than the lipid bilayer thickness.

Introduction

Membrane proteins as well as their fundamental peptide-lipid interactions are poorly understood areas due to inherent difficulties in working with membrane proteins. Often smaller model peptides are employed because they allow investigation of specific interactions under controlled conditions. Features such as peptide length, residue placement and side-chain properties that would normally be hard to interpret can be investigated effectively using model systems. There has furthermore been an increase in the study of antimicrobial peptides because of the emerging increase of multidrug-resistant bacteria in common antibiotics.[1] It has been found that peptide antibiotics could be useful because they kill bacteria at a rapid rate through the disruption of bacterial cell membranes. This new form of antibiotics may not be affected by the drug resistance that past antibiotics have faced.[2]

Small synthetic amino acid chains have been used to better understand how membrane proteins interact with lipid bilayers that are mimics with those in cell membranes that are a part of every cell in the human body. The model WALP series of peptides, Ac-GWW(LA)nLWWA-[ethanol]amide, have been extensively used to comprehend this concept.[3-6] The comprehension of membrane proteins are essential to the expansion of knowledge of biological processes, encoded gene products, and a good number of drug targets that lie within a cell.[6] WALP peptides are often transmembrane peptides with α helical structure.[5] Peptides that associate with the lipid bilayer can normally be described as in one of two states. The first is that the peptide is

long enough to reside inside or across the lipid bilayer. The amphipathic tryptophan residues at either end of a WALP peptide can interact with each side of the bilayer, producing an anchoring and stabilizing effect.[5] The second is that the peptide is too short to span the lipid bilayer and becomes surface-bound. Again using the tryptophans is possible, but this time the tryptophans would anchor the surface-bound peptide to the outside of the lipid bilayer. In both cases the tryptophans would be positioned in the lipid head group region near the membrane-water interface. The lipid bilayer is an important component of biological membranes because it controls the distribution, organization, and function of bilayer-spanning proteins, which are significant and imperative to the existence of life.[7]

RWALP15 contains 15 amino acids chain in the following sequence, acetyl-GRWLALALALALWRA-amide. (In the one-letter code, G is glycine; R, arginine; W tryptophan; L, leucine; and A, alanine.) The hydrophobic helical core of leucines and alanines in RWLAP15 is only about 13.5 Å long and is still only 16.5 Å in length when its tryptophan anchors are included. The lipids DLPC, DMPC, and DOPC have hydrophobic thicknesses of about 19.5, 23, and 27 Å, respectively. RWALP15 is therefore quite short and has both arginine and tryptophan as possible anchoring residues for a transmembrane orientation on each end of the peptide. For this project, I produced the RWALP15 peptide through solid-phase peptide synthesis. Two different samples were made with deuterated alanines in different positions. HPLC was employed to monitor the purity of the peptide, and mass spectrometry was utilized to measure the molecular mass of the synthetic RWALP15. Each peptide in fact was designed to include two deuterium-labeled alanines of differing isotope abundance levels. These ^{2}H isotope labels along with solid-state ^{2}H NMR can aid in the determination of the RWALP15 orientation with respect to the lipid bilayer, including the tilt and rotation within the lipid bilayer using the GALA (Geometric Analysis of Labeled Alanines) method.[4,8] In addition, circular dichroism (CD) spectroscopy was used to determine the secondary structure of the peptide in the lipid environments, and fluorescence emission spectra were recorded to examine the polarity of the tryptophan environment.

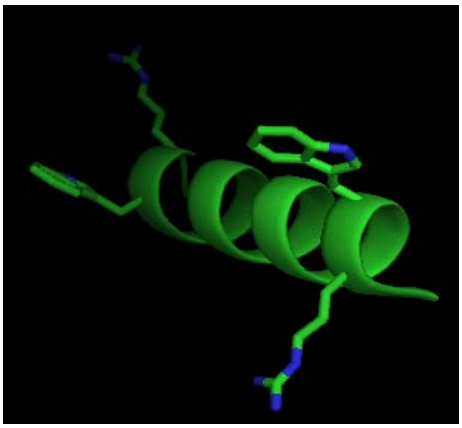

Figure 1: This 3-D image of RWALP15 illustrates its α-helix configuration and arginine and tryptophan side chain groups.

Methods

Due to the lack of commercially available isotopically-labeled Fmoc-Alanine-d_4 for use in solid-phase peptide synthesis (SPPS), it was first produced.[5,9] The chemicals alanine-d_4, manufactured by Cambridge Isotope Laboratories (Andover, MA), triethylamine (TEA) manufactured by Mallinckrodt (Paris, KY) and N-(9-fluorenylmethyloxycarbonyloxy) succinimide (Fmoc-ONSu) manufactured by NovaBiochem (San Diego, CA) were used for this synthesis reaction. Alanine-d_4 (445 mg) was dissolved in 5 mL of water plus 5 mmol (700 µL) of TEA in a round bottom flask. A stir bar was added and placed over a stir place in the hood. Then 4.8 mmol of Fmoc-ONSu (1.62 g) was dissolved in 5 mL of acetonitrile in a 20 ml beaker with gentle heating and a stir bar. The Fmoc-ONSu along with the acetonitrile was added to the round bottom flask all at once and stirred for two hours. During the first 15 minutes of the

reaction 200 µL of TEA was added as needed to the round bottom flask in order to stabilize its pH and make sure a pH between 8.5 and 9 is maintained during the two hour stirring period. After the two hour reaction period the stir bar was removed and the filtrate was concentrated on a rotary evaporator until the Fmoc-Alanine turned into a viscous yellowish-white gel. Then the stir bar was re-added and 60 ml of 4.0 N hydrochloric acid was added to the concentrated filtrate. An extraction with ethyl acetate was performed with 50 ml of ethyl acetate. The aqueous bottom layer was discarded. The extraction was conducted again with 60 mL of 4.0 N hydrochloric acid and then followed three more times with 100 ml of water each time. The ethyl acetate layer was collected in a clean round bottom flask, concentrated under nitrogen, and reduced with the rotary evaporator, and further dried under high vacuum overnight.[9]

The Fmoc-alanine-d_4 product was recrystallized to improve purity. To do so 50 mL of ethyl acetate was added to the product in the round bottom flask, and dissolved with stirring and gentle heating. The product was then filtered through a fine glass filter. The filtrate was transferred to a recrystallization jar and 15 mL of hexane was added to the mixture. The jar was placed in the freezer to induce crystallization. After a week in the freezer the formed crystals were filtered through a 150 mL course glass filter and the filtrate was returned to the freezer for the formation of another crop of Fmoc-alanine-d_4. ^{1}H NMR was performed on the product crystals to confirm the product collected was fmoc-alanine-d_4.

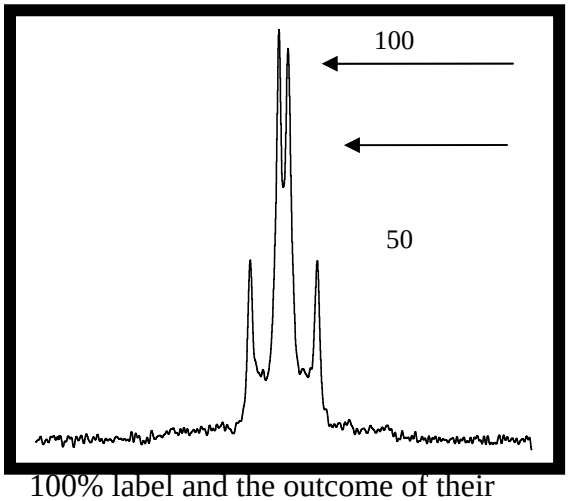

100% label and the outcome of their corresponding NMR splittings.

SPPS of RWALP15 – RWALP15 was synthesized using "Fast-Moc" chemistry on a Perkin-Elmer Applied Biosystems 433A synthesizer (Foster City, CA) using Fmoc-protected L-amino acids (NovaBiochem, San Diego, CA). Two deuterium-labeled Fmoc-alanines were incorporated into each peptide with differing abundances (50% and 100%). RWALP15 was synthesized first with labels on the 5th and 7th position alanine and again with labels on the 9th and 11th position alanine. Side-chain protecting groups were employed for residues containing potentially reactive side chains such as Fmoc- Arg-Pbf and Fmoc-Trp-Boc. The N-terminal was coupled with acetyl-glycine to ensure electrical neutrality on each end of the peptide. During this process, the fmoc-alanine is activated, the resin is deprotected, and the resin is coupled to the previous residue and then the process is repeated for the next amino-acid in the chain. TFA Cleavage – A cleavage reaction utilizing trifluoroacetic acid was performed to cleave the finished peptide from the acid-labile resin as well as remove any side-chain protecting groups such as the Pbf protecting group on the arginine and the Boc protecting group on the tryptophan residues.

A TFA cocktail was made consisting of 1.7 mL of TFA, 100 µL of triisopropylsilane, 100 µL of water, and 100 mg of phenol. The TFA solution was added to ~120 mg of RWALP15 resin and allowed to incubate on an orbital shaker for three hours. The cleaved resin and solution was filtered using a short glass Pasteur pipette with a glass wool and the TFA solution containing the peptide product was collected. The solution was reduced under nitrogen gas flow to about 1 mL. The peptide was precipitated in 25 ml of ice cold 1:1 Methyl *tert*-Butyl ether (MtBe)/Hexane in a 50 mL plastic centrifuge vial by adding dropwise. The solution was left on

ice for 30 min and after then centrifuged at 4 degrees Celsius for 10 minutes at 1500 RPM. The supernatant was discarded and the pellet was re-suspended in another 25 mL of ice cold 1:1 MtBe : hexane. This washing process was repeated three more times to remove bulk TFA. The pellet was then dried under nitrogen and lyophilized from 1 mL acetonitrile : water for 4 times to remove residual amounts of TFA.

Peptide Quantification – The resulting product was dissolved in 2 mL of TFE and transferred to a 10 mL vial. The centrifuge vial was then rinsed with another 2 mL of TFE. Two samples were prepared by mixing 10 µl of peptide solution with 4 mL of methanol. The absorbencies were then measured on a UV-Vis spectrometer at 280 nm. The average of the two absorbencies were found and the molar concentration was calculated. From the peptide solution, a 1 mg/mL solution was prepared for HPLC experiments. A 0.1 mg/mL solution was also prepared for mass spectrometry. MALDI-TOF mass spectrometry experiments were carried out at the Statewide Mass Spectrometry Facility by its staff. Peptides in TFE were dried under nitrogen gas flow down to a film and were lyophilized with 0.5 ml of acetonitrile and 0.5 ml of water, frozen in liquid nitrogen, and put on the vacuum line overnight.

Purification of RWALP15 - Peptides were purified through HPLC on a Zorbax Semi-prep C8 column using a 80/20 to 84/16 methanol/water gradient with 0.1% TFA over 30 minutes. Crude peptide was dissolved into two mL TFE and subsequent 500 µL aliquots were injected onto the column for separation and collection. UV-Vis monitoring at 280 nm was used for peptide detection. The collected purified solution was lyophilized three times to remove TFA.

CD and Fluorescence Sample Preparation – About 5 mg of RWALP15 powder was taken and dissolved in 1.5 mL TFE. Then 20 µL of the peptide was mixed with 980 µl of methanol and the concentration was determined of RWALP15 through UV-Vis at 280 nm. Then 62.5 mmol of RWALP15 from the TFE solution was transferred into three eppendorf tubes labeled with DLPC, DMPC, DOPC. Then 3.75 µmol of lipid was added to their respective eppendorf tubes to make a 1:60 peptide/lipid ratio. The tubes were filmed under nitrogen gas and put on a vacuum line for 48 hours. The peptide/lipid mixtures were resuspended with 500 µL of distilled water. The eppendorf tubes were then sonicated for one to two hours until they appeared transparent. After, the eppendorf tubes were centrifuged for 10 min at 10 thousand rpm and the supernatant was transferred to new tubes. Each solution was transferred to a 0.1 mm cuvette and the absorbances were checked on a diode array between 200-300 nm to ensure all values were under 1.5 AU. The CD samples were made and run utilizing a Jasco J710 spectropolarimeter (Easton, MD) using 1.0 mm path length, 1.0 nm band width and 20 nm/min scan rate. The samples were run from 190-250 nm with 13 scans per-sample. The fluorescence samples were diluted down to 1:10 with water, vortexed well, run, and spectra were recorded on a Perkin Elmer LS-55 fluorescence spectrometer. Samples were excited at 280 nm and five scans were collected and averaged.

Oriented NMR Sample Preparation – An oriented glass plate sample with a 1:60 peptide/lipid ratio was produced for solid-state NMR experiments. 1.33 µmol of peptide dissolved in TFE along with 80 µmol of lipid (either DLPC, DMPC, or DOPC) were transferred to a single glass test tube. The mixture was put under nitrogen flow to remove the solvents and placed on the vacuum line overnight. Forty glass slides were arranged over two petri dishes and 1 mL solvent (95% methanol and 5% water) was added to dissolve the peptide/lipid film. Then 25 µL of the peptide/lipid solution was added to each of the 40 glass plates evenly with a Hamiliton syringe. After, another 150 µL of methanol was added to the test tube and was evenly dispersed on the 40 glass plates. The glass plates were dried on under the vacuum line in a

dessicator for two days with a cover to protect the light sensitive samples. Afterwards, 1.2 µL of deuterium depleted water was added across each slide with a Hamiltion syringe. The 40 slides were stacked, and placed in a cuvette. Epoxy glue was used to seal a glass lid on the cuvette and 40 minutes later another layer of epoxy was placed over the first layer. The cuvette was then kept at 40 degrees celcius in a heating block until the samples became clear, which suggest they are ready for solid-state NMR experiments. P31 NMR was run on each sample to check bilayer alignment at both β=0 and 90, and proton decoupling The scans were run with a 90° pulse rate of 6 µs along with an interpulse time of 5 seconds. All samples were run on a Bruker Avance 300 spectrometer (Billerica, MA) operated at 46.1 MHz with 32 scans at 323K. After the P31 was run, the 2H solid-state NMR was run and quadrupolar splittings were found at both the β = 90° and β = 0° alignment using two Bruker Avance 300 spectrometers (Billerica, MA) operated at 46.1 MHz. The scans were run with an interpulse delay of 90 ms, 90° pulse time of 3.4 µs, and an echo delay of 115 µs with about 800,000 scans run per sample per alignment.

Results

Mass spectrometry was performed on each RWALP15 peptide synthesized to confirm that the molecular weight of the two samples were in fact RWALP15 plus the weight of the deuterium labels with a weight of 1730.1 g. The analytical HPLC chromatograms of each peptide demonstrated that most of the product was the RWALP15, but with small, acceptable amounts of impurities surrounding it. It was decided anyway to purify both RWALP15 (^{2}H: A5-50%, A7-100%) and RWALP15 (^{2}H: A9-50%, A11-100%) through the use of HPLC separation and UV-Vis monitoring to hopefully enable more distinct ^{2}H NMR quadrupolar splittings. The CD spectrum illustrated a peak at 208 nm and another peak at 222 nm, which shows that RWALP15 does contain an α-helix configuration. It was concluded that RWALP15 holds the α-helix character in DMPC with the highest MRE value at the wavelength of 195 nm and distinct peaks at 208 nm and 222 nm, closely followed by DLPC, illustrating that the RWALP15 α-helix is more strained in the DLPC lipid. The flatter DOPC CD graph shows that there is probably not much of helix in the DOPC lipid bilyer and RWALP15 is likely to surface bound in this situation, perhaps not crossing the lipid bilayer. Fluorescence data demonstrated that RWALP15 in DMPC, DLPC, and DOPC bilayers with hydrophobic thicknesses of about 19.5, 23, and 27 Å respectively gave max emission wavelength

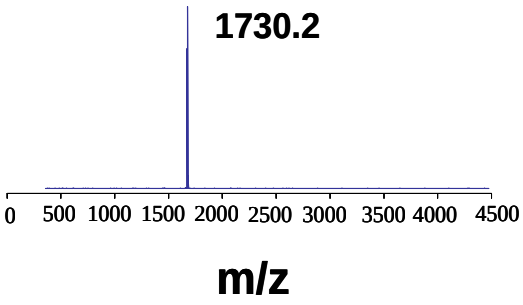

Figure 3 : Mass spectrometry of RWALP15 with molar mass of 1722.1 g + 8 g deuterium.

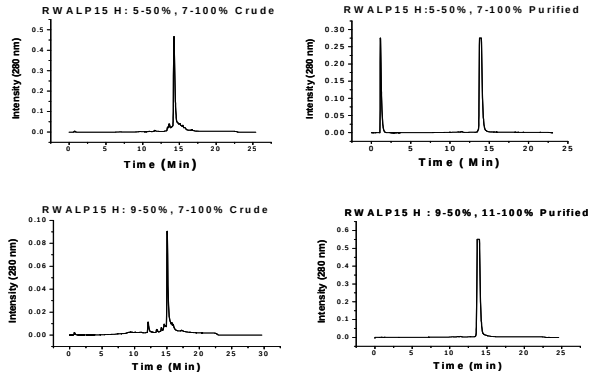

Figure 4 : Due to impurities, the RWALP15 crude product was purified through use of HPLC.

values at 334.5, 341.5, and 337 nm respectively. These wavelengths are less than the value of tryptophan in water, which has a fluorescence emission maximum at 355 nm. All ^{31}P spectra for the peptide-lipid samples run had a strong peak around -25 ppm for ß = 90° alignment and a strong peak around +25 ppm for ß = 0° alignment, indicating that all ^{2}H NMR samples were properly aligned in the bilayer phase. Solid state ^{2}H NMR of RWALP15 (^{2}H: A5-50%, A7-100%) and RWALP15 (^{2}H: A9-50%, A11-100%) in oriented glass plate samples were recorded in DLPC, DMPC, and DOPC bilayer lipids. Distinct ^{2}H quadrupolar splittings were observed for each sample; their values are listed in table 1. Peptide tilt analysis was performed using the GALA method [6]. The GALA results for DLPC show a S_{zz} value of 0.84°, a Tau value of 6.0°, a Rho value of 252°, an RMSD equal to 0.56 kHz (which indicates an excellent fit), and a epsilon parallel value for the alanine side-chain geometry of 59.4°. The GALA results for DMPC illustrated similar results with a S_{zz} value of 0.86°, a Tau value of 7.3°, a Rho value of 243°, an RMSD equal to 0.25 kHz, and again an epsilon parallel value of 59.4°. The Tau and Rho values are very similar for DLPC and DMPC, but RWALP15 seems to have radically different results in the CD spectroscopy and ^{2}H NMR results in DOPC.

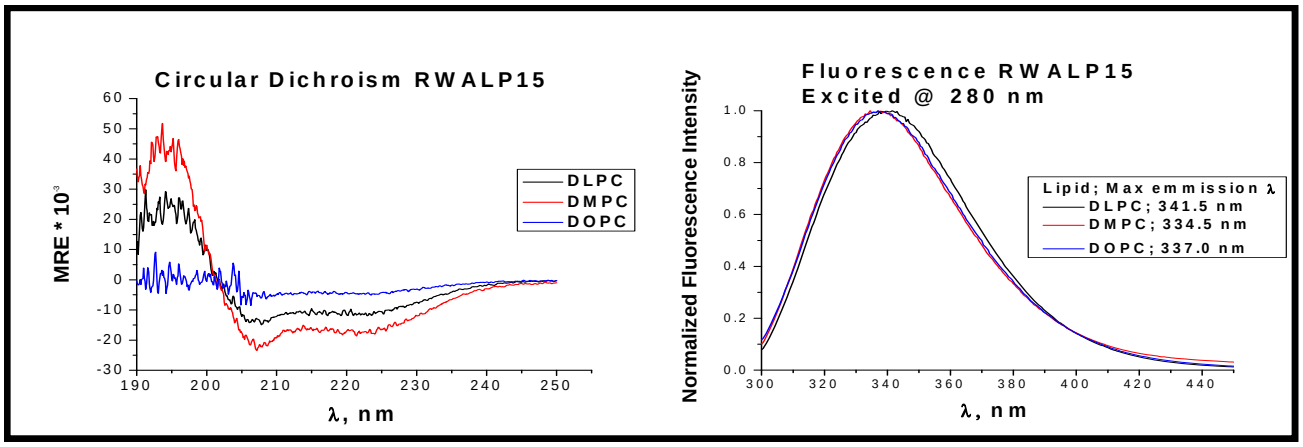

Figure 5: The CD results illustrated that RWALP15 resides in a α-helix configuration in all lipids, but a much smaller amount of helical character, if any, exists in DOPC, the longest of the lipids.

Figure 6: The fluorescence data indicate that Trp residues in RWALP15 are likely found at the membrane interfacial region in all DMPC, DLPC, and DOPC bilayers. This suggests a transmembrane orientation, or perhaps a surface orientation with tryptophans intercalated into DOPC.

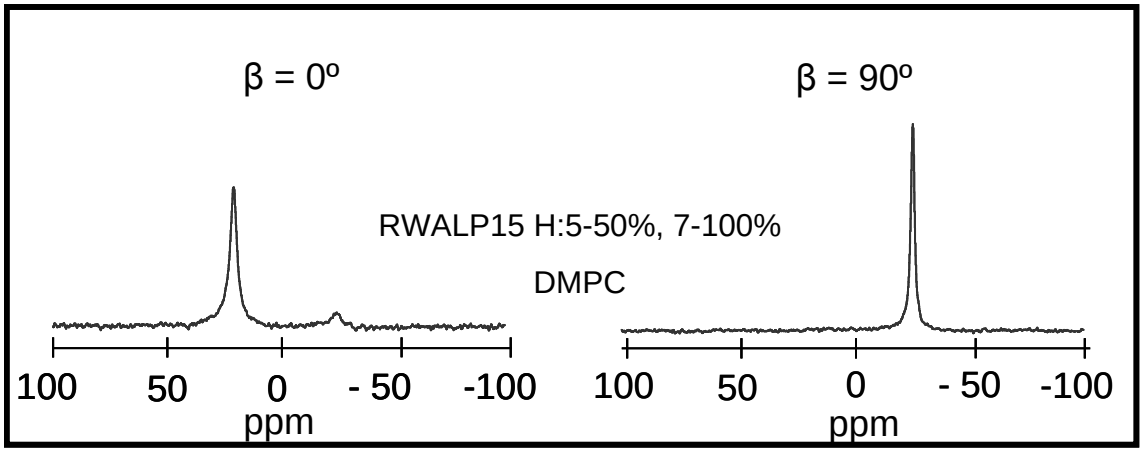

Figure 7: Oriented peptide-lipid samples were first analyzed with ^{31}P NMR to ensure a well oriented bilayer before running ^{2}H NMR experiments. At β = 0º an aligned sample should have a single peak around +25 ppm and at β = 90º the aligned sample should have a peak around -25 ppm.

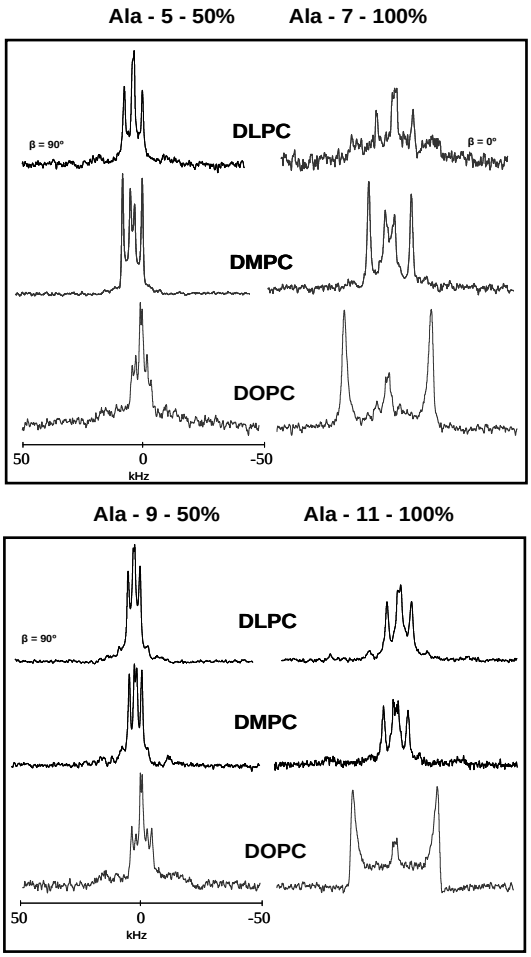

^{2}H Solid-State NMR Splittings

Lipid	DLPC			DMPC			DOPC		
Ala-d_4	β=0º	β=90º	"Average"	β=0º	β=90º	"Average"	β=0º	β=90º	"Average"
5(50%)	1.9	0.7	1.7	3.8	1.9	3.8	Unable to distinguish		
7(100%)	16.3	8.1	16.3	17.3	8.4	17.1			
9(50%)	1.3	0.6	1.3	2.1	0.9	2.0	Unable to distinguish		
11(100%)	10.5	5.1	10.3	10.1	5.0	10.1			

Figure 9 : RWALP15 was placed in the lipids DLPC, DMPC, and DOPC, which have a hydrophobic thickness of 19.5, 23, and 27 Å respectively. Distinct splittings were seen in DLPC and DMPC, implying that RWALP15 has defined orientations in these lipids. Side chain hydrogens are represented by strong peaks, with backbone hydrogens visible as well. The situation in DOPC is more complex.

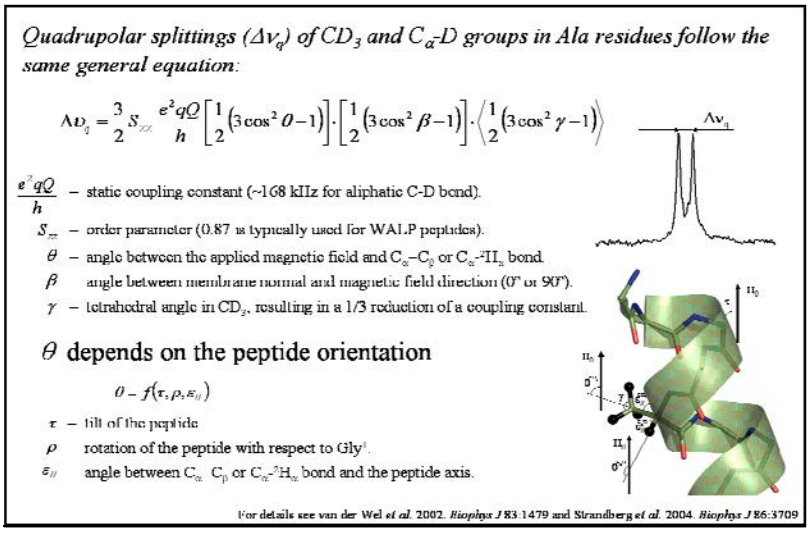

Figure 8 : This chart illustrates the concepts behind the GALA (Geometric Analysis of Labeled Alanines) analysis techniques.

RWALP in DLPC

S_{zz}	0.84º
Tau	6.0º
Rho	252º
RMSD	0.56 kHz
$\varepsilon_{//}$	59.4º

RWALP in DMPC

S_{zz}	0.86º
Tau	7.3º
Rho	243º
RMSD	0.25 kHz
$\varepsilon_{//}$	59.4º

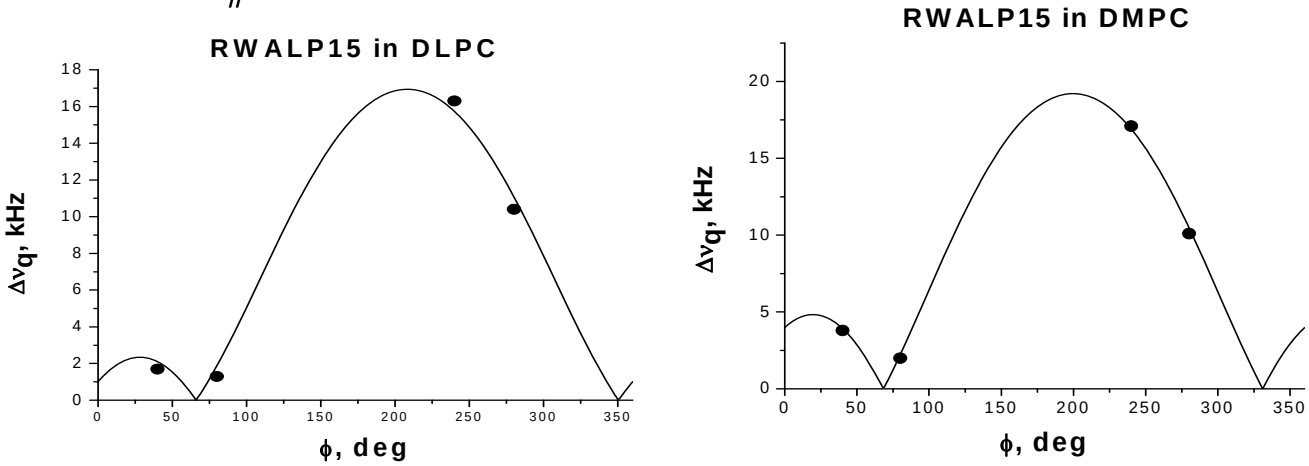

Figure 10 : The experimental data from DLPC and DMPC (shown with dots) were collected through ^2H solid-state NMR and best fit according to the $\Delta\nu_q$ equation. A best fit curve is shown with the solid line to demonstrate a specific GALA scenario.

Discussion

In the CD results, RWALP15 in DMPC lipid has an uncharacteristically stronger signal than when in a DLPC bilayer. This suggests that RWALP15's α-helix structure is better suited for the conditions that are present in DMPC, rather than DLPC, which is unusual. One speculation for the DLPC value to be lower than its DMPC counterpart is because of the competition between the arginine and tryptophan anchors on either end of the lipid bilayer unwinding and perhaps twisting or distorting the α-helix out of an ideal configuration. Further unwinding of the α-helix in DOPC would not exactly mach the GALA program that assumes that the peptide entered in its system is an α-helix in shape. The fluorescence data obtained stated that the tryptophans on either end of the peptide in all DMPC, DLPC, and DOPC are not out in the water surrounding the lipid bilayer. The fluorescence value for tryptophan in water is 355 nm, while the values obtained for RWALP15 in DMPC, DLPC, and DOPC are significantly less, implying that the tryptophans in each situation are somewhat removed from the water. The data for DOPC having a value that is in the middle of DLPC and DMPC is strange due to the fact that DOPC has the thickest membrane out of the three lipids. This data might suggest that DOPC is sitting on the membrane, not spanning it, with its tryptophans inserted in the lipid bilayer. The solid-state ^{2}H NMR data illustrate that RWALP15 does have defined orientations in or on the lipid bilayer in DMPC and DLPC, although multiple states may exist in DOPC, as too many peaks are seen, and different results are observed for the $\beta = 0°$ and $\beta = 90°$ sample orientations. The data also demonstrate that the RWALP15 peptide has a relatively small tilt in the membranes because all the main alanine side chain quadrupolar splittings are less than 10 kHz wide, which is not always true but commonly seen in the WALP series peptides. The RWALP15 (^{2}H: A5-50%, A7-100%) purified peptide in DMPC illustrated that the outer side chain peaks were the A7 position 100% deuterium labeled alanine with a more intense splitting than the middle peaks, which often receive an extra intensity from residual deuterium in the water. The HPLC purification process not only made the splittings of the deuterium labels more prominent, but made the signals of the labels further correspond with their deuterated intensities as well. The GALA projections as a result of the obtained NMR splittings illustrate that in both situations in DLPC and DMPC results are similar with a small amount of tilt and rotation in each lipid. These preliminary GALA results show that there is a small tilt (Tau) of only 6 to 7° and the rotation (Rho) of the RWALP15 peptide is about 250° in both lipids. There are a multitude of implications for the specific amount of tilt and rotation that RWALP15 demonstrates and why they vary from DLPC to DMPC. One reason is because the hydrophobic thickness of both DLPC and DMPC vary with values of 19.5 and 23 Å. With the core helix of RWLAP15 only being about 16.5 Å in length between its tryptophan anchors, this creates a mismatch in lengths, with the peptide trying to span the membranes that are larger than its central region. This difference can induce bilayer modulation and different peptide tilts to overcome this significant length difference. DOPC, with a hydrophobic thickness of 27 Å is almost twice the length of the RWLAP15 core, which can be a reason why the results from this experiment are complicated and might point to a surface–bound state for RWALP15 in this lipid. With the NMR results having more than two splittings in at the $\beta = 90°$ position and rather inconclusive splittings seen at the $\beta = 0°$ position, a GALA analysis could not be formulated for RWALP15 in DOPC, increasing speculation that RWALP15 may be surface bound in this situation.

Acknowledgements

I would like to extend my gratitude to the National Science Foundation, NSF-REU CHE-0851505, for giving me this opportunity to participate in this summer research experience, and Dr. Paul for coordinating the REU program at the University of Arkansas campus. I would also like to extend a special thanks to Dr. Roger Koeppe II for his guidance, Nicholas Gleason for his patience, and the rest of the Koeppe lab, Vitaly Vostrikov, Johanna M. Froyd-Rankenberg, and Dr. Denise Greathouse for their everyday assistance.

References

(1) Greathouse D.; Vostrikov V.; McClellan N.; Chipollini J.; Lay J.; Liyanage H.; Ladd T. *Journal of Peptide Science*. **2008**, 10, 1002.

(2) Hancock, R. Lancet. 1997, 349, 418-422.

(3) Killian, J.A.; Salemink, I.; De Planque, M.; Lindblom, G.; Koeppe, R.E. II; and Greathouse, D.V. *Biochemistry*, **1996**, 35, 1037-1045.

(4) van der Wel, P. C. A.; Strandberg, E.; Killian, J. A.; Koeppe, R. E.,II. *Biophys. J.* **2002**, *83*, 1479–1488.

(5) Thomas, R.; Vostrikov, V.; Greathouse, D.; Koeppe, R, II. *Biochemistry*, **2009**, 48, 11883-11891.

(6) Vostrikov, V.; Hall, B.; Greathouse, D.; Koeppe, R, II.; Sansom, Mark. *JACS*, **2010**, 132, 5803-5811.

(7) Anderson, O.; Koeppe, R, II. *Annu. Rev. Biophys. Biomol. Struct*. **2007**, 36, 107-130.

(8) Strandberg, E.;O¨ zdirekcan, S.; Rijkers, D. T. S.; van der Wel, P. C. A.;Koeppe, R. E., II.; Liskamp, R. M. J.; Killian, J. A. *Biophys. J.* **2004**,86, 3709–3721.

(9) Kortenaar, Int. *J. Pept. Prot. Res.*, **1986**, 27, 398-400.

Degradation of GDP to Form Apo-Cdc42 wt.

Erika Russell, Bethune-Cookman University
Daytona Beach, FL

Abstract

The goal of the summer research project was to examine possible new ways to liberate GDP from the protein of interest Cdc42Hs. Two experiments were tried to try to create apo-Cdc42Hs. First, the fluorescent analogue of GDP was degraded using alkaline phophatase. Secondly, Cibracon Blue was used as possible affinity matrix due to its high affinity for ADP-binding proteins and because it binds to ADP it should also bind to GDP. Furthermore, with apo-Cdc42Hs there will be a better understanding of the structure of Cdc42Hs which could potentially reveal insights on GDP dissociations and how this leads to cell proliferation[(1)].

Figure 1: Cdc42Hs-

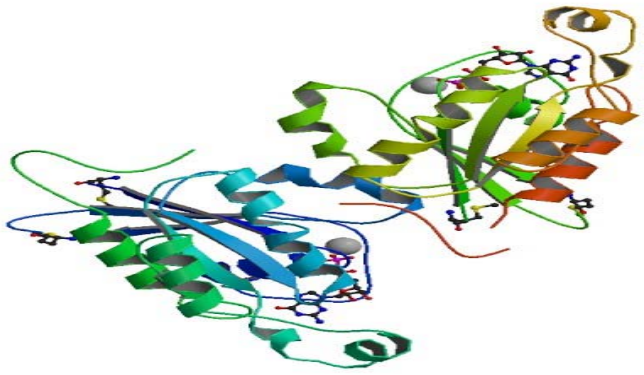

GDP[(2)]

Introduction

Cdc42 wt has 178 amino acids and is one of the first identified human oncogenic proteins—mutants of Cdc42 wt account for nearly 30% of all cancer cells[(1)]. The Ras family is a group of related proteins that are involved in cellular signal transduction. As a member of the Ras family of GTP-binding proteins, Cdc42 wt aids in cellular transformation and cell growth via increased rates of GTP to GDP cycling[(4)]. When Cdc42 wt is bound to GTP, it is active and will remain in this state until a GTP-ase activating protein causes it to hydrolyze the phosphate group body to an inactive GDP state. To return to the active state Guanine nucleotide exchange factors (GEFs) catalyze the exchange for bound GDP to GTP. This is significant because a regulatory protein, dbl, has the ability to stimulate the exchange for GDP to GTP in Cdc42 wt either by increasing the rate of cycling between GTP and GDP, or by a deficiency in GTPase activity which can lead to cell proliferation and transformation[(1)]. Additionally, Cdc42 wt has a high affinity for dbl when it is in a nucleotide free state which is why it is important to determine new ways to liberate GDP from Cdc42 wt in order to begin to study the molecular details of this form of the protein. One of the new approaches included the potential exploitation of a chromatographic matrix with an affinity for proteins with a well-defined nucleotide binding site.

Experimental Procedures

Cdc42Hs was expressed in Escherichia coli BL21(DE3) (Novagen) at 37^{o}C for 3.5 hours. Protein expression was induced with 1mM IPTG at a cellular density of OD_{600}0.4-0.5. The cells were disrupted in a French pressure cell (20,000 psi) in 300mM NaCl, 50 mM Tris-HCl, (pH 8.0), 10mM $MgCl_2$, with protease inhibitor (1mM AEBSF, 1x Halt protease inhibitor, 1mM GDP). The soluble fraction after centrifugation at 20,000 rpm for 30 minutes was subjected to affinity chromatography on a 5mL nickel column (HisTrap, GE Healthcare, Piscataway, NJ). The protein eluted from the column at 100 mM imidazole with a 0-to300-mM imidazole linear gradient over 5 column volumes. A chromatograph of Cdc42Hs being eluted by imidazole can be seen in figure 1. The imidazole was removed by ultrafiltration. Protein aliquots were lyophilized and held at -80^{o}C. The concentration of the purified protein was determined by absorbance spectroscopy (extinction 15,370 M^{-1} cm^{-1}, at 280nm).

Once the protein was purified two different experiments were attempted to try to accomplish the same goal—the generation of apo-Cdc42Hs. In the first experiment the goal was to unfold Cdc42Hs using a buffer containing Urea, and to refold without GDP. To begin parameters were established using a control protein Pyruvate Kinase and a Cibracon-Sepharose Column. The protein was selected because it possesses a dinucleotide fold and because of this it should bind well to the Cibracon blue dye. This is believed because Cibracon Blue dye is covalently attached to the Sepharose matrix[7-8] and can be used to have a greater affinity for the binding sites of proteins with a dinucleotide fold like Pyruvate Kinase and Glutamine Synthetase. This is important to try because if it works then we can also try to bind Cdc42 wt to exploit potential binding affinity of Cibracon Blue. Consequently, in the control experiment the control protein Pyruvate Kinase was added to a cibracon-sepharose column. The column was equilibrated with 20mM Tris-Base buffer pH 7.5, followed by adding 300mM of NaCl pH 7.5 (via a gradient) to elute the protein[4]. A picture of what this should look like can be seen in the chromatograph in figure 3. The goal was to elute the protein using NaCl and confirm that the protein came off the column by gel electrophoresis. The hope was that once this was accomplished we could then place the sample containing protein, GDP, EDTA, DTT, Mg2+, and Urea (to unfold protein) into dialysis tubing in PBS buffer[4]. Place dialysilate on column and elute using imidazole. Finally, add apo-Cdc42Hs to cibracon-sepharose column.

In the second experiment a fluorescent analogue of GDP—Mant GDP was added to a buffer containing 64mM Tris-HCl, pH 7.6, 1mM EDTA, 1mM NaN_3[5]. Subsequently, dry alkaline phosphatase (200µL) beads were added to the Mant-GDP-Buffer, and the reaction was observed over 2 hour period of time—taking readings (200µM of Mant-GDP buffer and 800µM buffer) every 20 minutes using the fluorometer (This was important to try because if alkaline phosphatase degraded the fluorescent analogue of GDP then it should also degrade GDP in Cdc42Hs). Once this is accomplished GDP was exchanged for GMPPCP. Alkaline Phosphatase reduced GDP to guanosine, (which can be monitored on the FPLC) and after a full GDP-GMPPCP exchange is believed to have occurred phosphodiesterase will be added to degrade GMPPCP and leaving Cdc42Hs nucleotide free[5] and ready to be added to the Cibracon-Sepharose column.

Data Collection and Analysis:

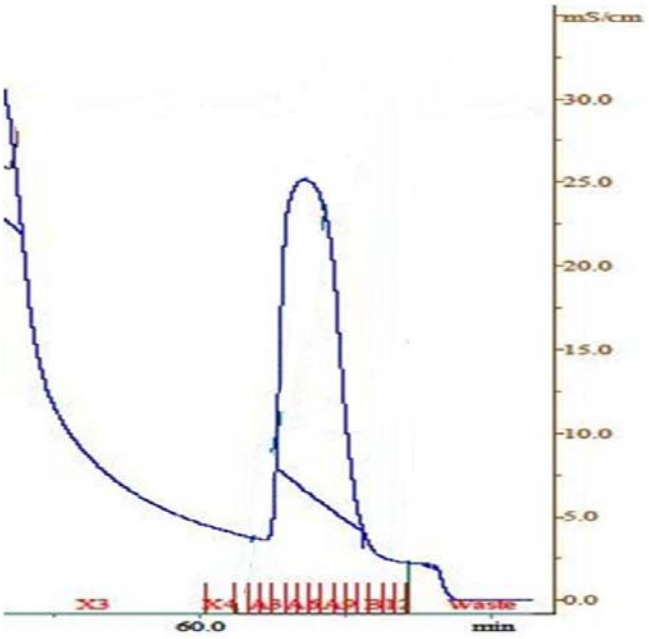

Figure 2

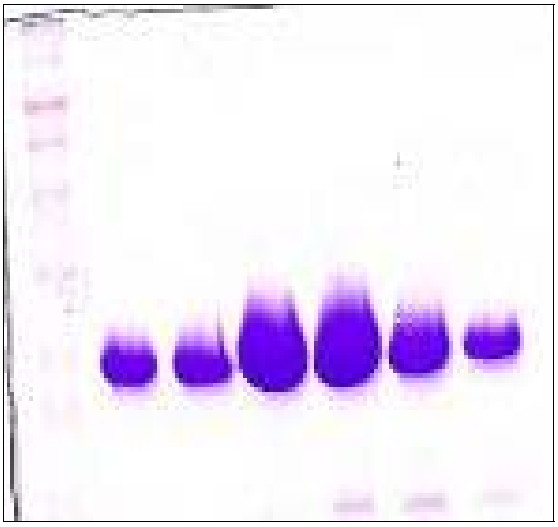

Figure 3

Figure 2 shows a chromatograph of Cdc42Hs being eluted by imidazole using the FLPC (2L of culture yielded 2ml of pure Cdc42Hs). There were a lot of setbacks that prolonged the process of protein purification. An extensive amount of time was spent on the preparatory work to attempt to purify Cdc42Hs. First, DNA had to be extracted from E. coli cells and a transformation was performed in competent E. coli cells. A transformation is done by pre-warming the water bath to 42^{o}C, incubating plates at 37^{o} C, and adding 1 µl of DNA to the culture. Proceed by adding 20µl of BL21 DE3 and placing in water 30 second. Next, insert LB miller broth into each sample, mix gently, and place in shaker for 45 minutes (200 rpm and 35^{o} C). Centrifuge for 5 minutes at the maximum speed, insert 100 µl of LB miller broth into each sample, and decant 100µl of LB miller broth followed by 50µl of sample onto agar plates. Use cell spreader to spread across each plate and allow growing over night at 37^{o} C in incubator. Once this process is complete perform a test expression via gel electrophoresis that allows for verification that the protein has been expressed. If an ample of amount of protein is visible in the gel then the protein is amplified. If the protein results do not show this then the process is performed again with new DNA, which was done numerous times until we finally attained adequate test results via gel electrophoresis. Figure 3 shows gel electrophoresis confirming pure Cdc42 wt. The samples were collected from the fractions that correspond to the peak in figure 2.

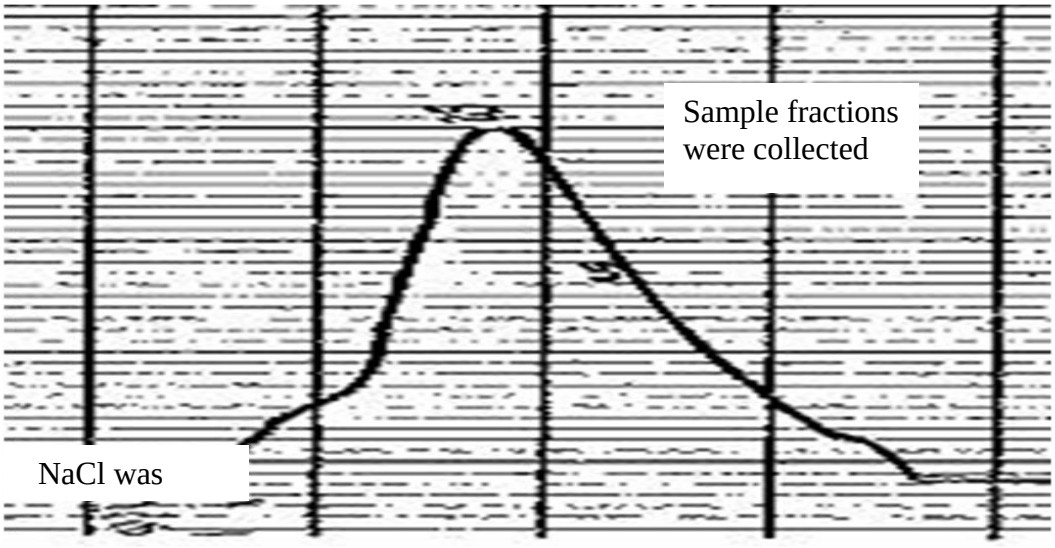

Figure 4

Figure 4 shows a Chromatograph of Pyruvate Kinase from Cibracon Sepharose column. Sample fractions were collected and tested using gel electrophoresis, however we did not see any bands at 25Kda (molecular weight of pyruvate kinase) so we could not confirm that this is the protein. Consequently, some experimental error could be involved; especially because obstacles arose from the fact that the amount of protein necessary to be able to observe the protein is unknown. Therefore, the challenge was to successfully bind enough protein to the cibracon-sepharose column to visibly observe the presence of protein via gel electrophoresis—which did not occur.

Results and Discussion

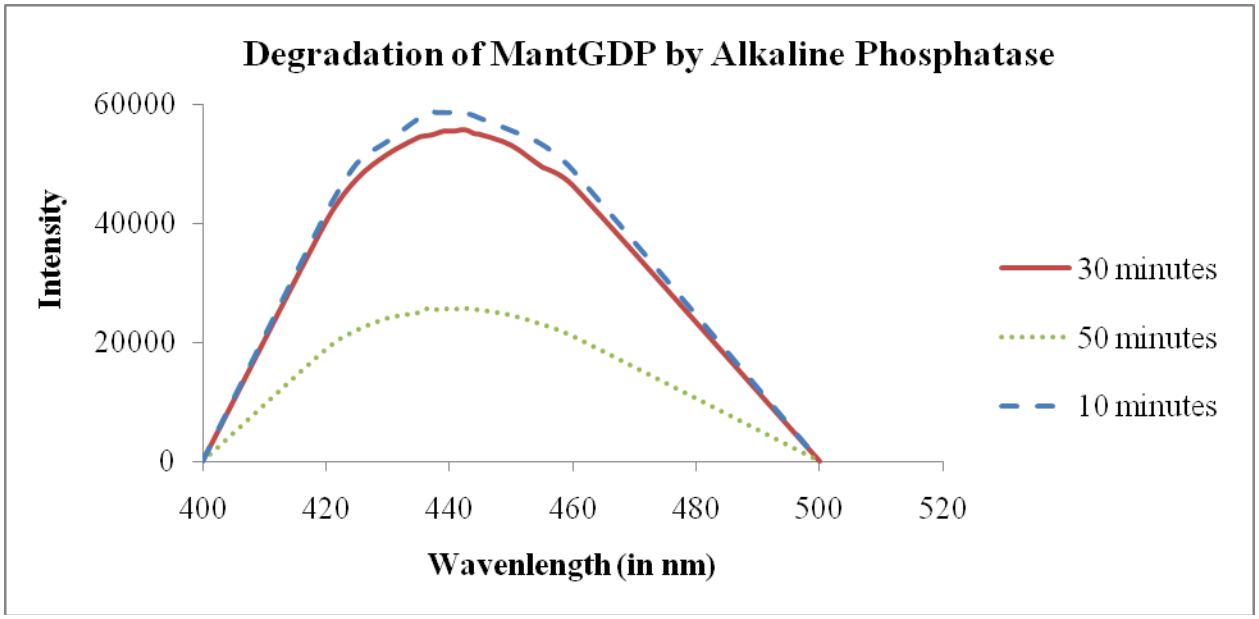

Figure 5

In figure 5, Alkaline Phosphatase was added to Mant-GDP buffer. The reaction was observed over 1 hour period of time—taking readings (200μM of Mant-GDP buffer and 800μM buffer) every 20 minutes using the fluorometer. The graph showcases the intensity decreasing significantly because GDP is degraded by Alkaline Phosphatase.

Figure 6

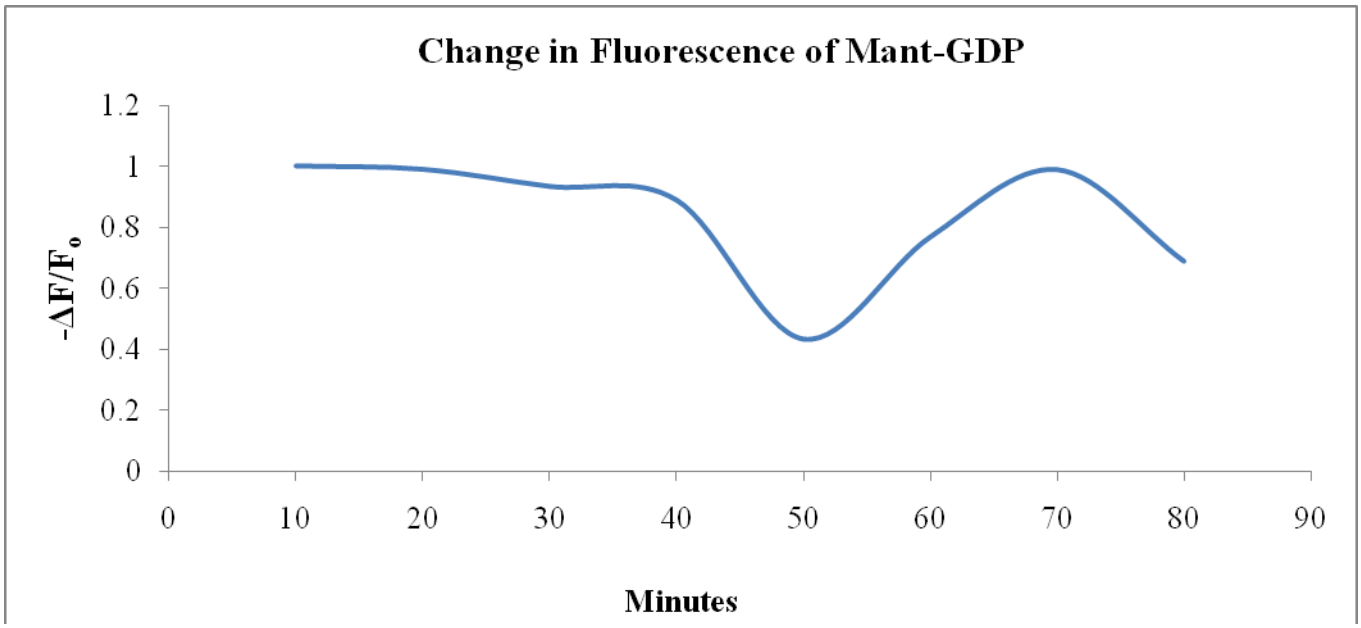

Figure 6 is a continuation of figure 5, here ΔF is the change in fluorescence relative to the initial fluorescence, where the initial value is the 10 minute reading and the final value is the 80 minute reading. This graph further illustrates what is being displayed in figure 4, that at about 50 minutes GDP is degraded.

Conclusion

In Figure 4, for the first 50 minutes the intensity steadily decreases starting at 60,000 and dropping to 25,000—after 50 minutes the intensity fluctuates indicating that GDP was completely degraded after about 50 minutes. However, we were unable to repeat experiments to establish a trend in the potential noise after 50 minutes or if another excited state process was being exploited from an emission stand point. From this information there is reason to believe that because Alkaline Phosphatase degrades the fluorescent analogue of GDP then it should also degrade bound GDP in Cdc42Hs.

Acknowledgements

Funding was provided by National Science Foundation CHE-0851505/REU and NIH-5K01CA113753 to P.D.A. A special thank you is given to Dr. Paul Adams for support, guidance and instruction, as well as Brandon Suttles and Reena Chandsashekar for assistance and supervision.

References

1. Bos, Mariano. Ann. Rev. Bioichem. “Ras Genes” (1987) 55, 779-827.

2. Demerdash, Omar, and Michael Daily. PLoS Computational Biology (2009) 5(10):e1000531ff.

3. Feltham, Joanna, Volker Dotsch, Sami Raza, and Danny Manor. Biochem.“Definition of the Switch Surface in the Solution Structure of Cdc42H*s*.” (1997) 36, 8755-8766.

4. Jing Zhang and, C. Robert Matthews. Biochem. “Ligand Binding Is the Principal Determinant of Stability for the p21H-ras Protein.”(1998) 37, 14881-14890.

5. John, Jacob, Roland Sohmen, Jurgen Feuerstein, Rosita Linke, Alfred Wittinghofer, and Roger Goody. Biochem. “Kinetics of Interaction of Nucleotides with Nucleotide-Free H-ras p21.” (1990) 25, 6058-6065.

6. Lowe, Christopher, and James Pearson. Methods Enzymol “Affinity chromatography on immobilized dyes.” (1984)104, 97–113.

7. Sakai, Hiroshi, Koichi Suzuki, and Kazutomo Imahori. J. Biochem "Purification and Properties of Pyruvate Kinase from Bacillus stearothermophilus." (1986) 99.4, 1157-1167.

8. Thompson, Sioe T, and Earle Stellwagen. PNAS USA. "Binding of Cibracon blue F3GA to proteins containing the dinucleotide fold." (1976) 73.2, 361-365.

9. Thompson, Sioe T, Kathleen H Cass, and Earle Steelewagen. PNAS USA. "Blue Dextran-Sepharose: An Affinity Column for the Dinucleotide Fold in Proteins." (1975) 72, 669-672.

A Kinetics Study of Cytochrome C and Cytochrome C Oxidase

Maria Williams, Texas Southern University
Houston, Texas

Abstract

The basis of my experiment is to the study the reaction of cytochrome c and cytochrome oxidase using site-directed mutagenesis and steady-state kinetics. The goal was to characterize the electrostatic interaction between cytochrome c and cytochrome oxidase. The mutants that were expressed in this project were E89T/E90Q and E89T/E90K. These mutants replaced the native negative charge on glutamic acid 90 [E90] with a neutral charge, glutamine [Q], or a positive charge, lysine [K]. By gathering data from the kinetic experiments, we will be able to determine if the mutations had an effect on the reaction between cytochrome c and cytochrome oxidase. Steady-state kinetics generally displays saturation kinetics at sufficiently high cytochrome c concentrations and often obeys Michaelis-Menten kinetics with a Michaelis constant, K_m, and a maximum velocity, V_{max} [2].

Introduction

Electron-transfer reactions play an essential role in biological processes such as mitochondrial respiration. Cytochrome c and cytochrome c oxidase are two major components of the electron transport system (Figure 1). Cytochrome c is an electron carrier outside of the mitochondrial membrane shuttling one electron at a time from complex III to complex IV. It contains a heme group with two axial ligands, one His-N and one Met-S, giving octahedral coordinates to the iron atom. The two iron oxidation states are Fe (III) d_5 and Fe (II) d_6 [4].

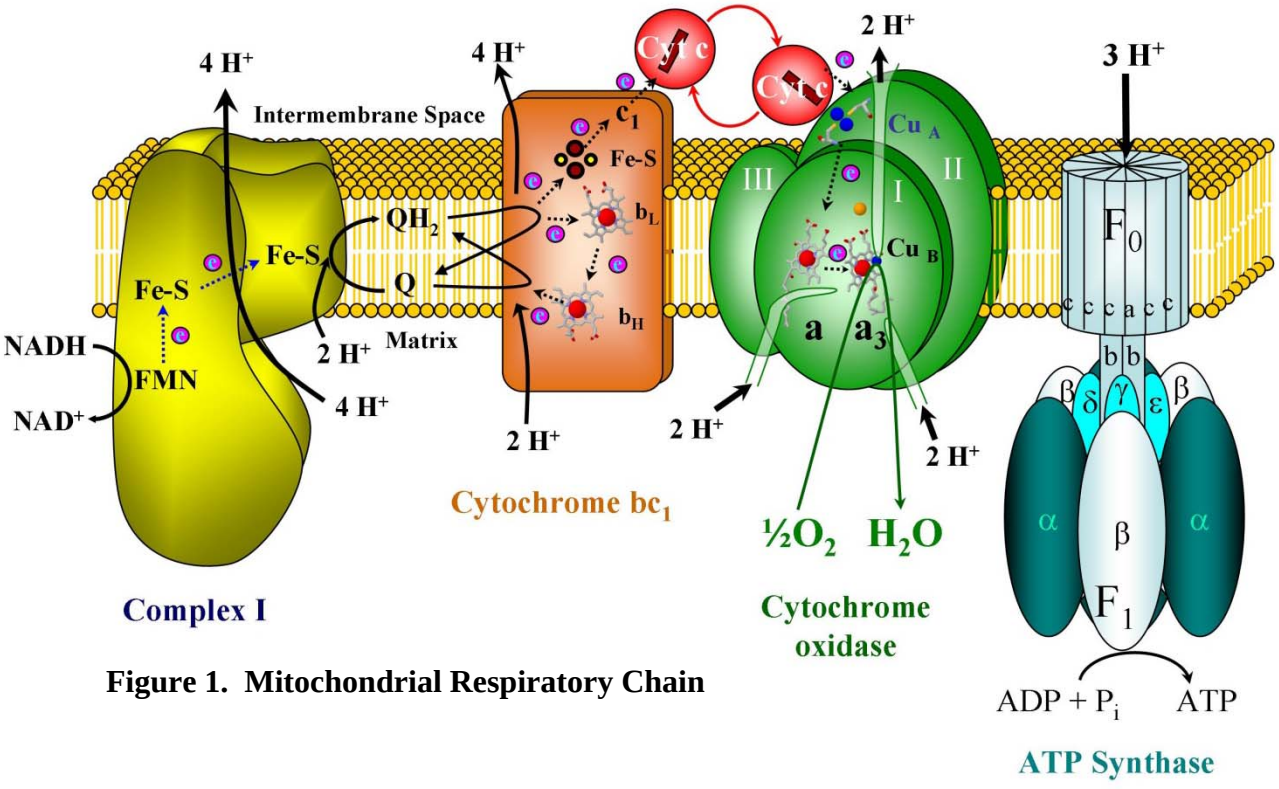

Figure 1. Mitochondrial Respiratory Chain

Cytochrome oxidase is a large membrane-bound enzyme with each half of the dimer consisting of 13 polypeptide chains. The complex acts as a terminus of mitochondrial electron transport in aerobic life, by using four electrons to reduce dioxygen. A series of metalloprotein complexes embedded in mitochondria or bacteria utilizes electron transfer reactions to pump protons across the membrane and create an electrochemical potential (Figure 1) [1]. In each half of cytochrome oxidase there are three metal sites that involve electron transfer: bimetallic Cu_a monometallic cytochrome a, and bimetallic heme a_3/Cu_b (Figures 1,2). Cytochrome c initiates electron flow through the enzyme by delivering one electron at a time to Cu_a, which sits just outside of the membrane. Electrons flow from $Cu_{a,}$ though cyt a to a_3/Cu_b, which is where O_2 is bound and reduced to water [6]. Two sources of electrons are known for the ETS, namely nicotine adenine dinucleotide (NAD) and flavin adenine dinucleotide (FAD). Reduced NAD transfers electrons to complex I and FAD transfers electrons to succinate dehydrogenase complex (complex II).

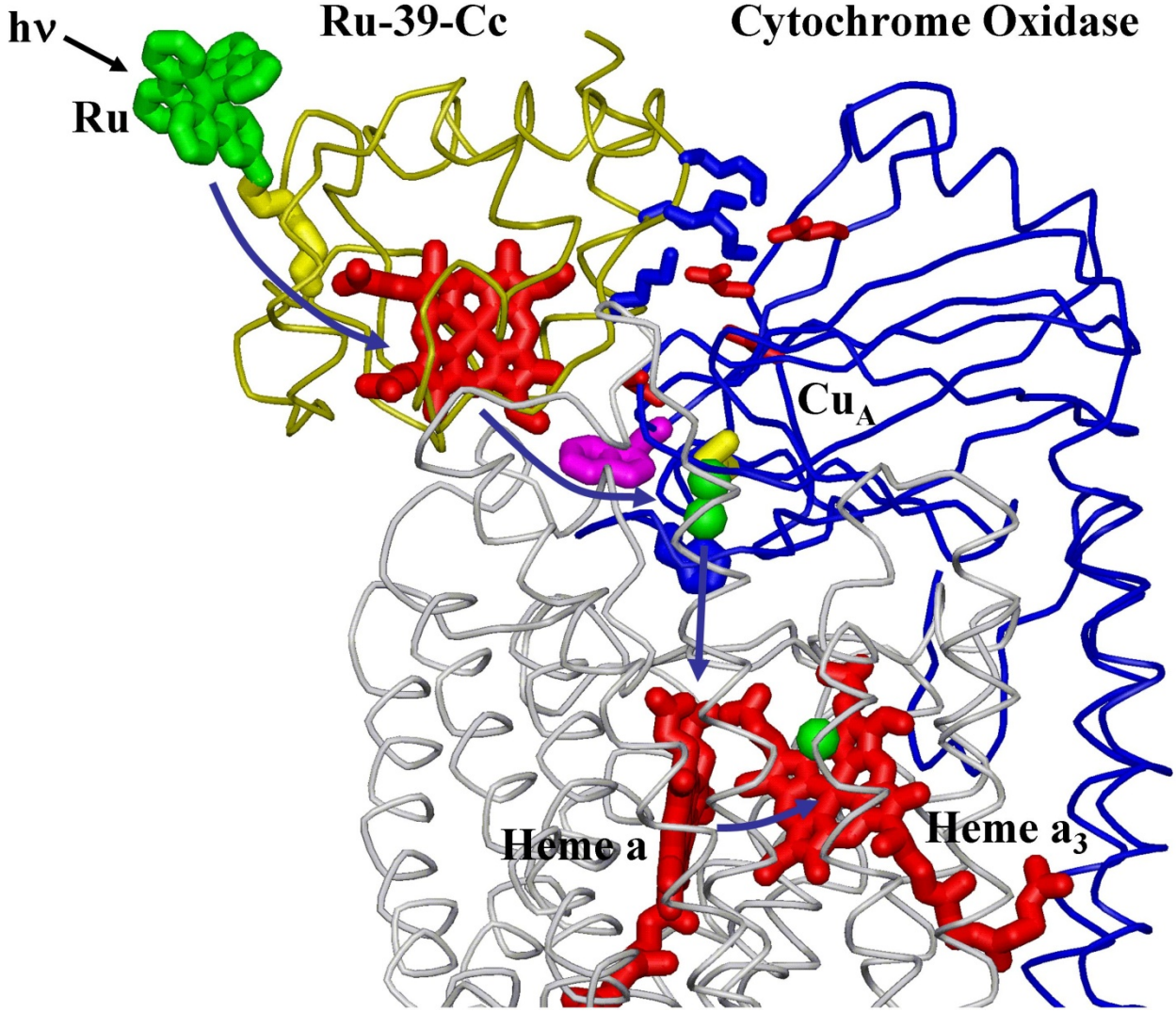

Figure 2. Complex between Cytochrome c and Cytochrome Oxidase

Oxygen serves as the terminal electron acceptor, oxidizing the heme a_3/Cu_b binuclear center in cytochrome oxidase. Electron transport inhibitors act by binding one or more redox centers, preventing electron transfer directly [3]. Changes in the chemiosmotic gradient are used to control electron transport, and only two electron entry points in the electron transport chain are known to be used in the mitochondria. An inhibitor may completely block electron transfer by irreversibly binding to a redox site. For example, cyanide binds with cytochrome oxidase so as to prevent oxygen binding and reaction. Electron transfer is reduced to zero.

The overall goal of my experiment was to the study the reaction of cytochrome c with cytochrome oxidase using site-directed mutagenesis and steady-state kinetics. The specific aim was to characterize the electrostatic interaction between cytochrome c and cytochrome oxidase. The mutants that were expressed in this project were E89T/E90Q and E89T/E90K (Figure 3). These mutants replaced the native negative charge on glutamic acid 90 [E90] with a neutral charge, glutamine [Q], or a positive charge, lysine [K]. By gathering data from the kinetic experiments, we will be able to determine if the mutations had an effect on the reaction between cytochrome c and cytochrome oxidase.

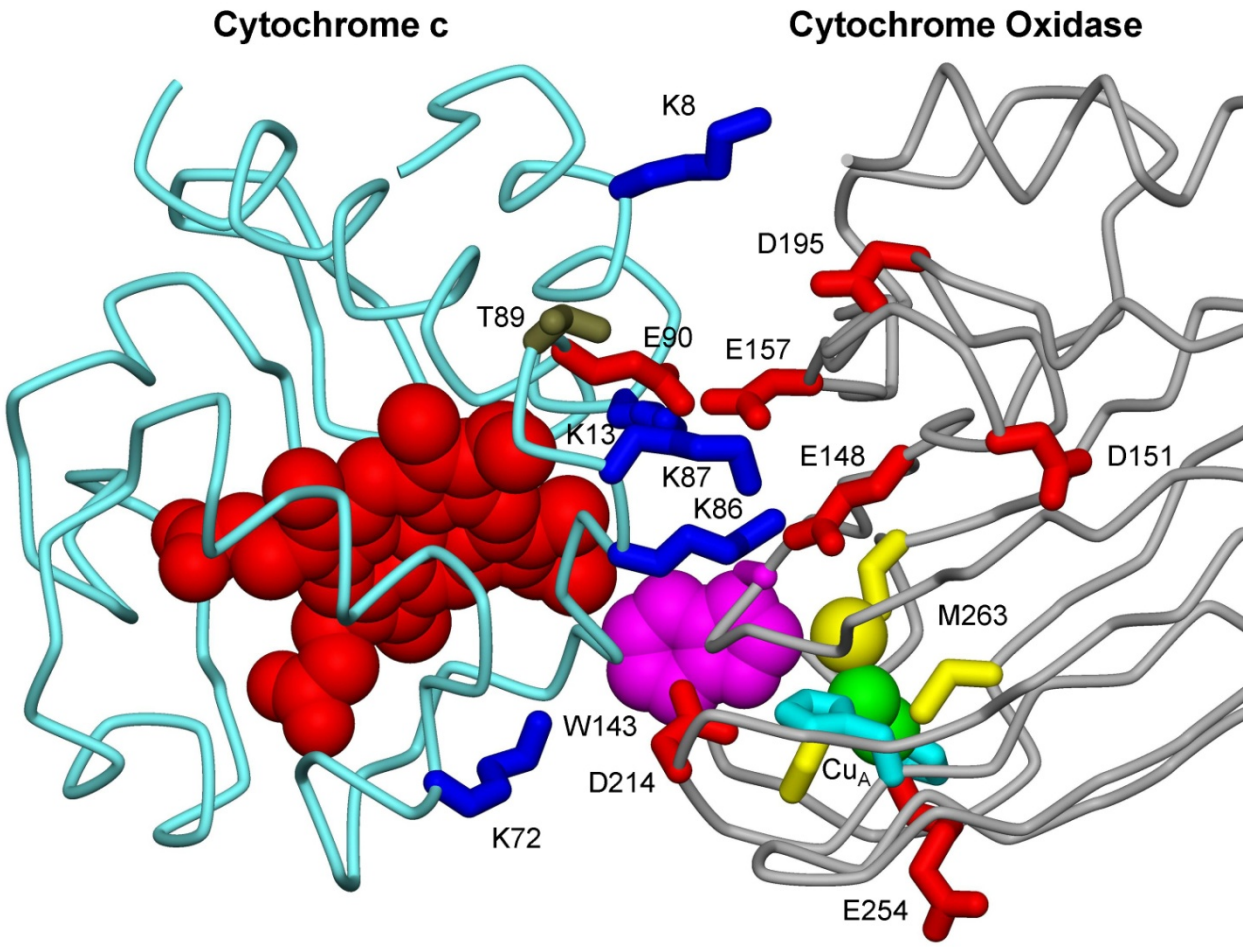

Figure 3. Complex between Cytochrome c and Subunit II of Cytochrome Oxidase

Experimental Procedure

The mutants that were used in the experiment are labeled as E89T/E90Q and E89T/E90K. The mutants were expressed in XL21BE3 native E.coli cells using plasmid DNA strands with the selected mutations which will grow and express. The mutants were expressed in rich broth for a forty-eight hour period and were spun down in the centrifuge to get the protein into solution. Once all of the rich broth is gone the cells were lysed and the protein purified. The purification process included ammonium sulfate precipitation, size exclusion chromatography, and high pressure liquid chromatography (HPLC) using a cation exchange column. The protein was highly pure after the HPLC. The protein still had a high concentration of salt, so it was exchanged with 5 mM sodium phosphate pH 7, using a centrifuge concentrator. The protein was then used for the kinetic studies. The kinetics was started by measuring out .08705 grams of sodium dithionite and 5 milliliters of water to make .1M of solution which is made anaerobic. The stock solution of oxidase was diluted by a 1:100 ratio, so 3 uL of oxidase was diluted with 300 uL of buffer. The buffer was 5 mM sodium phosphate/100 mM NaCl .01% lauryl maltoside, pH 7 at 25 C. For each experiment, a concentration of cytochrome c was placed in 500 uL of buffer and degassed. The concentration was then measured on the degassed sample and on average 3 to 5 μL of sodium dithionite was added to the sample to fully reduce cytochrome c. The spectra were checked again to see if cytochrome c was fully reduced. Once this had happened, the top was opened to check to see if the spectra remained stable. The amount of oxidase was measure out by calculating the concentration of the oxidase stock. On the days the experiments were conducted, approximately 5 nM cytochrome oxidase was used. Then the required amount of oxidase was added to the sample and the rate of oxidation of cytochrome c was measured at 550 nm in the spectrometer. This was repeated many times to obtain data for the experiment.

Results and Data Analysis

In (Figure 4), the E89T/E90Q mutants coming off the cation exchange column of the HPLC in a highly pure state. The highest peak in the chromatogram represents the time it took the pure protein to elute off of the column.

In (Figure 5), at approximately 550 nm, the spectrometer is reading that the E89T/E90Q mutant has been completely reduced at this peak.

In (Figure 6), the transient graph shows the reduction of E89T/E90Q mutant with cytochrome oxidase.

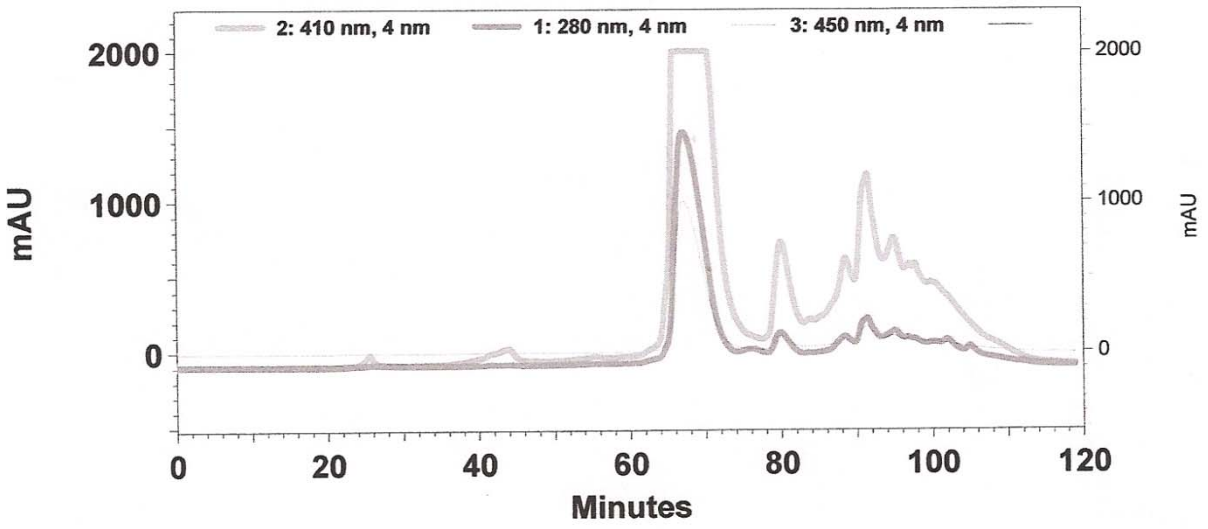

Figure 4. HPLC Chromatogram of E89T/E90Q

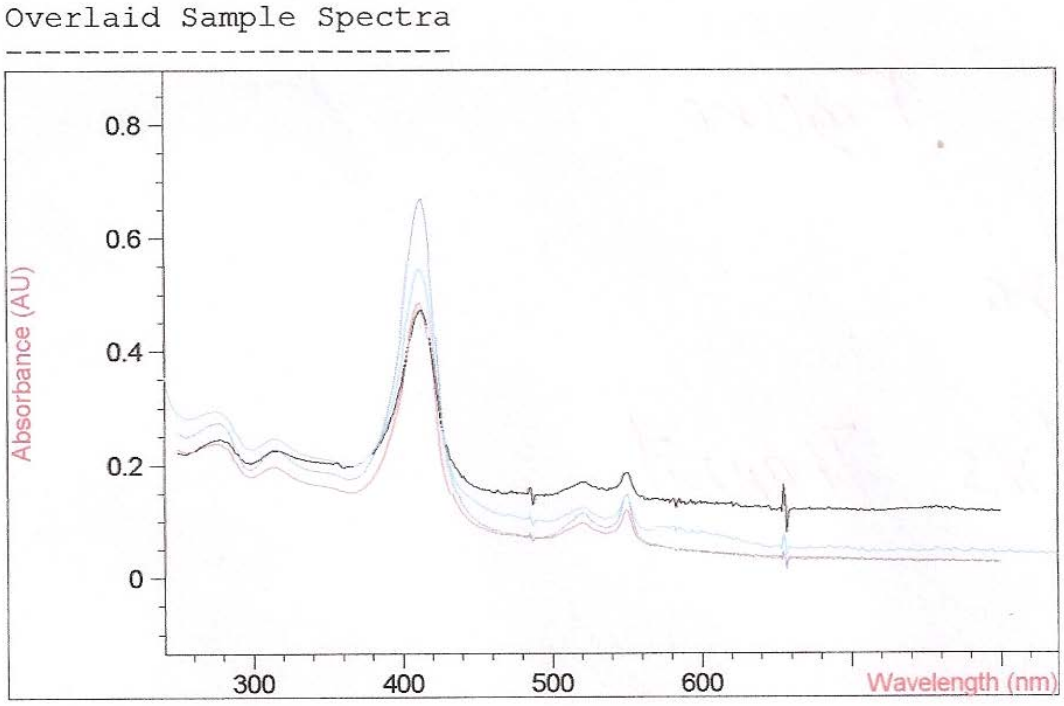

Figure 5. Visible Spectra of E89T/E90Q

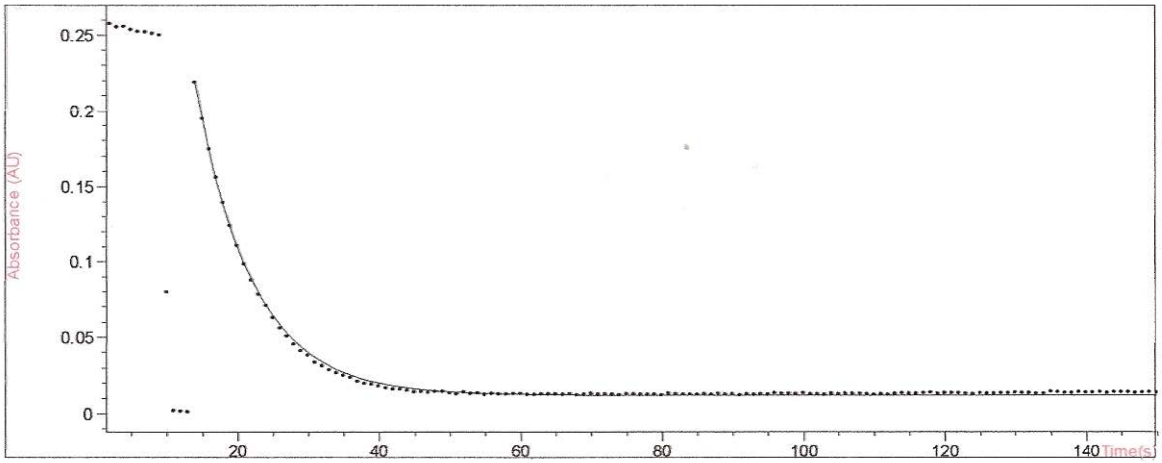

Figure 6. Reduction of E89T/E90Q cytochrome c by cytochrome oxidase monitored at 550 nm.

Kinetics of Reaction of cytochrome c mutants with cytochrome oxidase

07/15 Human Cyt c Wild Type

V_{max}= 4.76

Concentration uM	Rate s^{-1}
1.13 uM	0.678
3.38 uM	0.792
4.8 uM	1.62
8.2 uM	2.60
18.2 uM	2.61

07/15 E89T/E90Q

V_{max}= 2.74

Concentration uM	Rate s^{-1}
3.6 uM	0.876
8.34uM	1.25
10.5 uM	1.44
14.2 uM	1.92
22 uM	1.81

07/15 E89T/E90K

V_{max}= 2.04

Concentration uM	Rates s^{-1}
2.2 uM	0.831
5.4 uM	0.894
12.3 uM	1.62
16.4 uM	0.918
25 uM	1.29

07/16 Human Cyt c Wild Type

V_{max}= 3.20

Concentration uM	Rates s^{-1}
1 uM	0.756
2 uM	2.03
3.4 uM	1.42
5 uM	2.39
8.7 uM	1.30
13.4 uM	2.01
17.9 uM	1.52

07/16 E89T/E90K

V_{max}= 2.47

Concentration uM	Rates s^{-1}
1.88 uM	0.700
3.85 uM	0.576
4 uM	1.26
9.12 uM	1.48
12.33 uM	2.00
18 uM	1.72

Discussion

The goal of our experiments was to determine the effect of replacing the native negative charge of the glutamic acid [E] of position 90 of cytochrome c with a neutral charge, glutamine [Q] and a positive charge lysine, [K]. The E98T/E90Q mutant expressed well and that allowed us to collect a large amount of protein for kinetic experiments. The E89T/E90K mutant did not express well but we did obtain enough for the kinetic experiments.

The reaction of cytochrome c with cytochrome oxidase obeyed first-order kinetics at all concentration of cytochrome c. The results of my experiments were that at lower cytochrome c concentration, the first-order rate constant was larger, and at higher cytochrome c concentration

the rate constant became smaller. The experiments were conducted on two consecutive days. Over the two day period we were able to gather data to plot on graphs but the 07/16 E89T/E90Q data was too scattered to plot. The objective in plotting the points is a trend line to get values for the $V_{max.}$

In summary, the V_{max} of both the E89T/E90Q and E89T/E90K mutants was smaller than that of wild-type cytochrome c, indicating that residue 90 plays a role in the interaction between cytochrome c and cytochrome oxidase.

Conclusion

The data that was collected indicated that E89T/E90Q and E89T/E90K mutants had a smaller V_{max} than that of the human cyt c wild-type. The residue 90 plays an essential role in the reaction between cytochrome c and cytochrome oxidase. For a significant conclusion, there was not enough data to conclude that the E90Q and E89T/E90K mutants bind tighter to the cytochrome oxidase. The oxidase was placed on ice for the duration of the project but once a concentration of cytochrome c has been taken the activity of the enzyme may need to be checked also for stability.

Acknowledgements

This research was funded by NSF REY CHE-0851505. A special thanks to Dr. David Paul for the opportunity to participate in the REU program. I would also like to thank Dr. Lois Geren, Marilyn Davis, Dr. Jeffrey Havens, and Dr. Francis Millett who helped in the completion of this project. Without you this effort would have not been possible.

References

1. Johnathan P. Holser, Shelagh Ferguson-Miller, and Denise A. Miller
   Annu. Rev. Biochem. 2006.75:165-187.

2. Millett, F., deJong, C., Paulson, L., & Capaldi, R. A. (1983) Biochemistry 22, 546.

3. Pickrell AM, Fukui H, Moraes CT Springer Science+ Business Media, LLC 2009.

4. Siletsky SA, Han D, Brand S, Morgan JE, Fabian M, Geren L, Millett F, Durham B, Konstantinov AA, Gennis RB.
   Biochim Biophys Acta. 2006 Sep-Oct;1757(9-10):1122-32. Epub 2006 Jul 21.

5. Yuan ZQ, Zhang Y, Li XL, Peng YZ, Huang YS, Yang ZC.
   Eur J Pharmacol. 2010 Jul 12.

6. Zhen Y, Schmidt B, Kang UG, Antholine W, Ferguson-Miller S.
   Biochemistry. 2002 Feb 19; 41(7):2288-97.

APPENDIX

Student Posters
Candid Pictures

Analysis of [6,6]-phenyl C_{61}-butyric acid methyl ester (PCBM) by FTMS

Eric M. Berget[1], Evgenia Akhmetova[2], Charles L. Wilkins[2]
[1]Minnesota State University Moorhead, Moorhead, MN, 56563, USA
[2]University of Arkansas, Fayetteville, AR, 72701, USA

Overview:

▪Optimal sample preparation protocol was developed for Matrix Assisted Laser Desorption/Ionization Fourier Transform Mass Spectrometry (MALDI-FTMS) analysis of [6,6]-phenyl C_{61}-butyric acid methyl ester (PCBM, $C_{72}H_{14}O_2$) by comparing different matrices, matrix:analyte ratios and sample deposition methods.

▪Laser power influence was investigated and the optimum value was established.

▪Laser Desorption/Ionization (LDI) FTMS analysis of PCBM was carried out as well and results were compared to those produced by MALDI-FTMS.

Introduction:

▪Organic photovoltaic (OPV) cells commonly use PCBM as an electron-accepting material, however it undergoes degradation under service conditions.

▪The investigation of degradation kinetics of PCBM and other components of OPV devices by laser ionization mass spectrometry techniques (such as MALDI and LDI) is the final goal of this project.

▪Fourier Transform Mass Spectrometry (FTMS) was used to analyze PCBM. FTMS uses an image current generated by the ion's cyclotron frequency to generate the mass spectrum by a mathematical process called the Fourier Transform.

▪MALDI is a soft ionization technique in which the analyte is mixed with a large excess of a matrix compound and deposited on the target plate. After deposition on the plate, the sample is exposed to the short laser pulse and is ionized with the assistance of the matrix compound which absorbs and dissipates the energy from the laser. Another laser ionization method is LDI, which is an ionization process similar to MALDI except without the use of an organic matrix as an energy buffer.

▪In this preliminary study pure PCBM was analysed using LDI and MALDI ionization methods in order to establish optimal sample preparation protocol. Several molar matrix to analyte ratios (250:1, 500:1, 750:1, 1000:1, 2000:1, 5000:1) were compared as well as two different matrix compounds – dithranol and 9-nitroanthracene. The two methods of sample deposition (dry droplet and aerospray) were compared as well.

Experimental:

Instrumentation and analysis:

▪Mass analysis was performed using the positive ion mode of a 9.4T Bruker Ultraflex FTMS with external ionization source and utilizing a Nd:YAG laser (operating at 355 nm). Each spectrum represents an average of 35 scans, each using 30 laser shots.

▪For spot-to-spot reproducibility analysis, experiments were performed as triplicates, collecting spectra from different spots on the target plate.

▪The spectra were calibrated with external peptide standard II mixture using matrix α-cyano-4-hydroxycinnamic acid (CHCA). The peptides Angio 21, Angio 1, and SubsP were used as calibration points.

Sample preparation:

▪Both PCBM and matrix compounds (dithranol, 9-nitroanthracene) were dissolved in toluene and mixed together.

▪Several molar matrix to analyte ratios were composed: 5000:1, 2000:1, 1000:1, 750:1, 500:1, 250:1.

▪For the dried droplet deposition method, approx. 1 µl of the matrix-analyte mixture was deposited on the stainless steel target plate and allowed to air dry.

▪For the aerospray deposition method, aerosol particles produced from approx. 50-100 µl of the matrix-analyte mixture were deposited on the stainless steel target plate.

Data & Discussion:.

Figure 1: MALDI-FTMS spectrum of PCBM; matrix-dithranol, molar matrix:analyte ratio 250:1, laser power 50%.

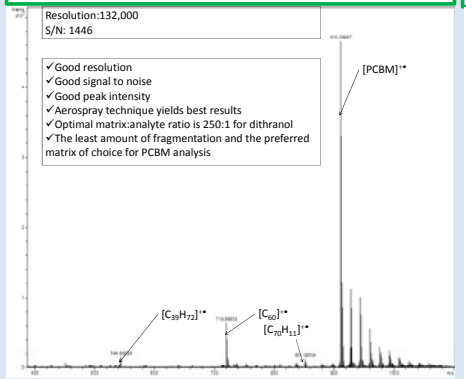

Figure 2: Enlarged section of the spectrum shown in figure 1.

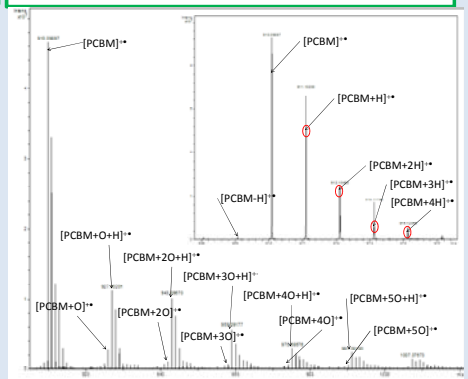

Figure 3: MALDI-FTMS spectrum of PCBM; matrix-9-nitroanthracene, molar matrix:analyte ratio 750:1, laser power 50%.

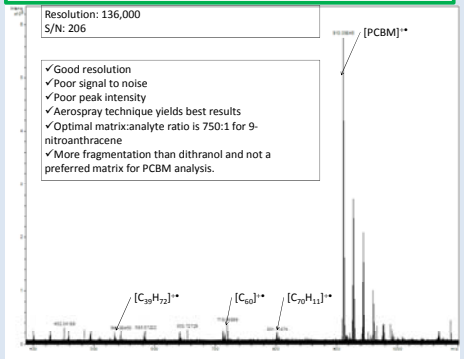

Figure 4: LDI spectrum of PCBM, laser power 50%.

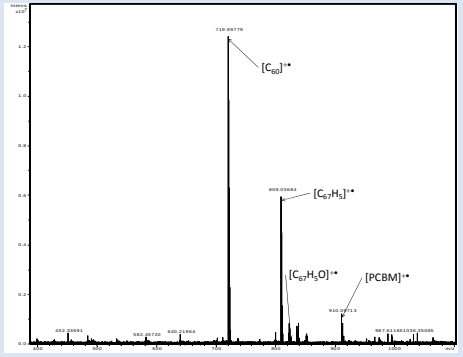

Figure 5: Laser power influence on the PCBM signal intensity (matrix-dithranol)
A – Dried droplet technique
B- Aerospray technique

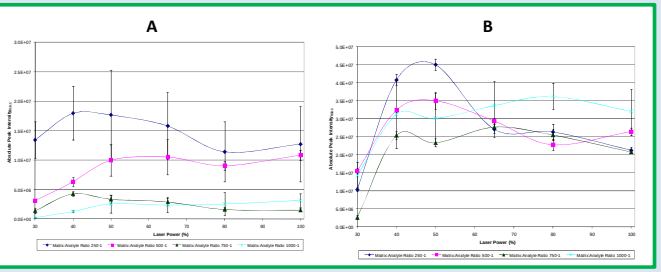

Figure 6: Laser power influence on the PCBM signal intensity (matrix-9-nitroanthracene)
A – Dried droplet technique
B- Aerospray technique

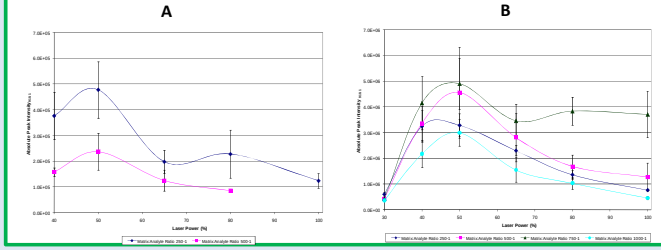

Figure 7: Illustration of PCBM ion generation and the reason for the appearance of double peaks.

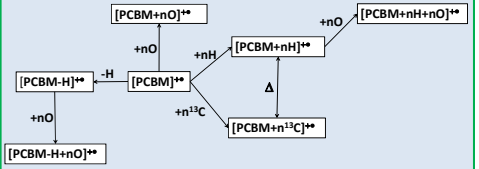

Figure 8: Composite summary of absolute peak intensity of PCBM at various molar matrix to analyte ratios.

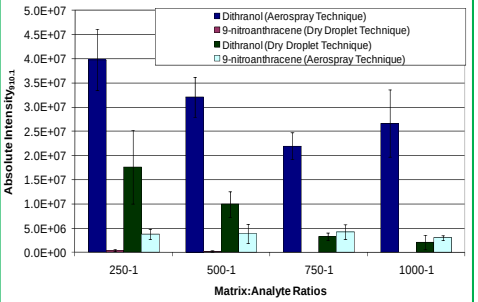

Conclusions:

▪Formation of various hydrogenated and oxidated derivatives of PCBM was observed and the species were identified.

▪The use of dithranol as a matrix at matrix:analyte ratio of 250:1, and aerospray deposition technique at a relative laser power of 50% produced spectra with the highest PCBM signal yield, highest signal-to-noise ratio and minimal amount of fragmentation.

▪ Aerospray deposition method was proven to produce spectra with higher spot-to-spot reproducibility.

Future Considerations:

▪NMR analysis of PCBM sample is needed to clarify whether the oxidated species are being formed during mass spectrometry experiment or are the evidence of sample degradation.

▪Accurate measurement of the laser power and shot-to-shot reproducibility is needed to quantify obtained results.

Acknowledgements:
The National Science Foundation CHE-0851505/REU
Dr. David Paul
Matthias Krust

Exploring New Reactivity of 2*H*-Azirines in Metal Catalysis and Organocatalysis

Jean-Marie Charles[1,2] and Dr. Nan Zheng[2]
(1) Cameron University, Physical Sciences Department, Lawton, Oklahoma 73505
(2) University of Arkansas, Department of Chemistry and Biochemistry, Fayetteville, Arkansas 72701

Background and Information

- Azirines are the smallest unsaturated heterocycles.
- Two isomers of azirines are known to exist:

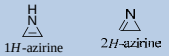

- 1*H*-azirines are anti-aromatic and much less stable than 2*H*-azirines.
- 2*H*-azirines possess a highly reactive nature influenced by their ring strain, making them useful precursors to synthesize more elaborate heterocycles[3]. However, they have been seldom studied in organocatalysis.

(3) Palacios, F.; de Retana, A. M. O.; de Marigorta E. M.; de los Santos, J. M. *Org. Prep. Proced. Int.* **2002**, *34*, 219.

Goals

We were interested in exploring the new reactivity of 2*H*-azirines with the aim of developing a new catalytic method for the synthesis of pyrrolidines with up to four continuous stereocenters. We proposed that with the assistance of a secondary amine such as L-proline, 2*H*-azirines would react with enals to create the desired pyrrolidine derivatives. Our group has recently developed a catalytic method for the synthesis of indoles from 2*H*-azirines. To increase the efficiency of this method, we were also interested in synthesizing indoles directly from the pentafluorobenzoates of oximes hence bypassing 2*H*-azirines as the intermediate.

Experimental

Synthesis of 2H-Azirines

Sequence I

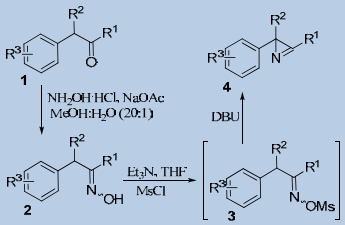

Taber D.F.; Tian, W. *J. Am. Chem. Soc.* **2006**, *128*, 1058-1059.

Sequence II

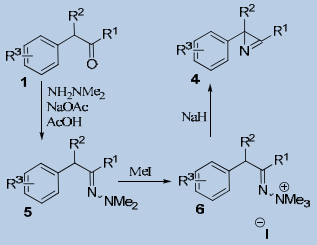

Padwa A.; Carlsen, P.H.J. *J. Org. Chem.* **1978**, *43*, 2029-2037.

Azirines Used in the Study

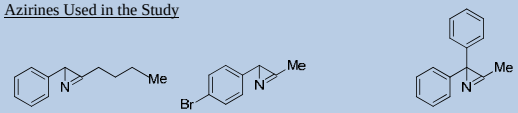

(synthesized through Sequence I)

(synthesized through Sequence II)

New Reactivity of 2H-Azirines

We Proposed:

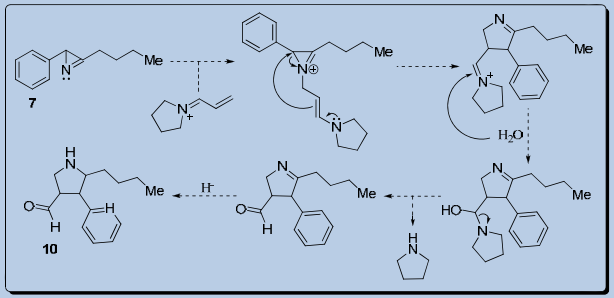

Results Obtained:

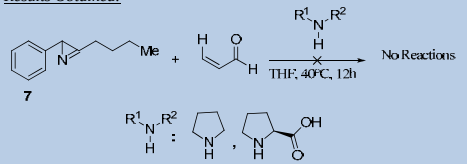

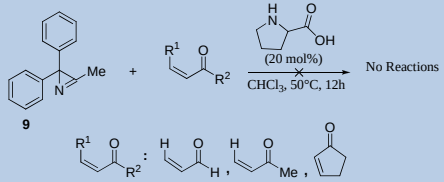

We Proposed:

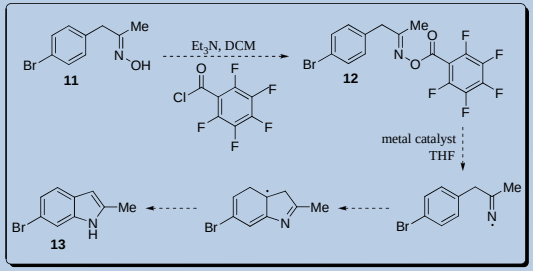

Results Obtained:

Table 1. Catalyst Screening

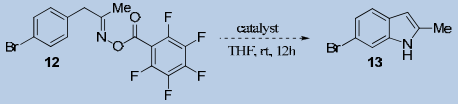

entry	catalyst (mol %)	**13**, yield (%)
1	CuCl (50)	0[a]
2	$CuCl_2$ (50)	0
3	CuTC (50)	0
4	$[CF_3SO_3Cu]_2 \cdot C_6H_5CH_3$ (10)	0
5	$FeCl_2$ (50)	0
6	$FeCl_3$ (50)	0[a]

[a] 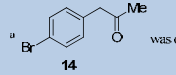 was obtained.

Conclusion

In conclusion, we have not yet been able to synthesize the pyrrolidine derivatives as we had proposed since in the observed reactions, 2*H*-azirine was completely recovered. We have not been able to obtain indoles directly from the pentafluorobenzoates of oximes either. However, we observed several byproducts in the screening experiments, one of which we identified was ketone **14**..

Acknowledgements

•University of Arkansas
•NSF-REU grant (CHE-0851505)
•Arkansas Bioscience Institute
•Dr. Samaresh Jana
•Dr. Mingzhao Zhu
•Mack D. Clements
•Daniel Rackl for synthesizing **9**

Computer Modeling of the Thermal Rearrangement of 2-aryl-2H-azirines to Indoles

Vernon D. Crowell and Peter Pulay
University of Arkansas, Fayetteville

Introduction:

Indoles see wide use in the pharmaceutical industry and are a common bioactive natural product. This has driven chemists to develop more effective ways of synthesizing indoles. Dr. Zheng and his lab have worked on a method utilizing the thermal rearrangement of 2-aryl-2H-azirines to indoles. Past experiments used various palladium or rhodium catalysts, but Dr. Zheng's lab sought to find a less expensive catalyst. The lab's experimental work discovered that only iron(II) chloride catalyzed the reaction, and only when the reaction occurred in THF. In order to supplement the experimental work, a theoretical study of a proposed catalytic cycle was performed.

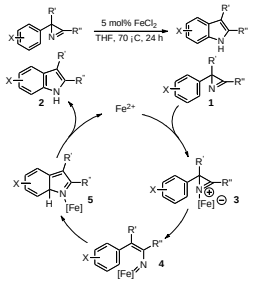

Jana, Samaresh; Clements, Mack D.; Sharp, Barry K.; Zheng, Nan. "Fe(II)-Catalyzed Amination of Aromatic C-H bonds via Ring Opening of 2H-Azirines: Synthesis of 2,3-Disubstituted Indoles." Accepted for publication by JACS.

Purpose:

The purpose of this project is to use computer modeling to supplement experimental work on the catalyzed thermal rearrangement of a 2H-azirine to a 2,3-disubstituted indole. A possible catalytic cycle involving a tetra-coordinated iron(II) complex was modeled at the B3LYP level.

Initial Reaction:

Calculations were performed at the B3LYP level of theory using the moderately sized m6-31g-d basis set. The initial catalyst was assumed to be the high spin, tetra-coordinated iron(II) complex shown in the reaction below.

Transition State Search and Verification:

After optimizing the geometries of reactants and the initial intermediates, approximate transition state geometries were found by scanning the coordinate of importance to that reaction step. In this catalytic cycle, various carbon-nitrogen bonds were scanned and the geometries optimized while constraining the bonds to certain lengths. After optimizing the approximate transition state obtained from scans, the transition state is verified by running a frequency calculation. A true transition state will have only one imaginary frequency, and this frequency can be verified as the true transition state by viewing the vectors corresponding to this frequency. The vectors with the largest magnitude should correspond to the variable being scanned.

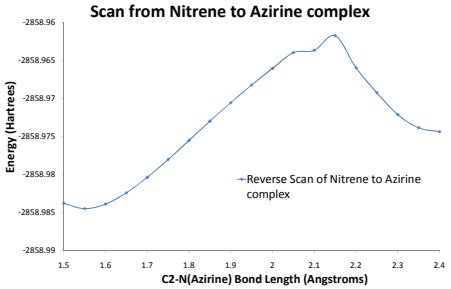

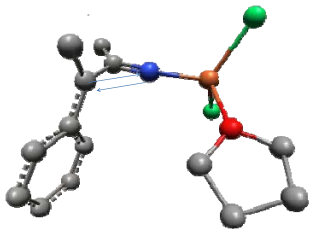

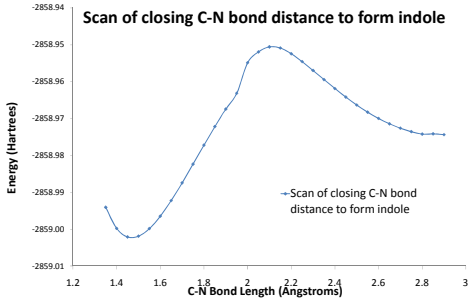

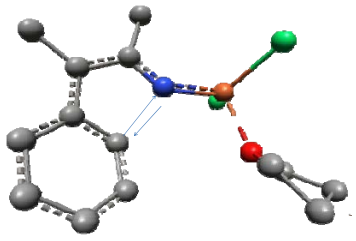

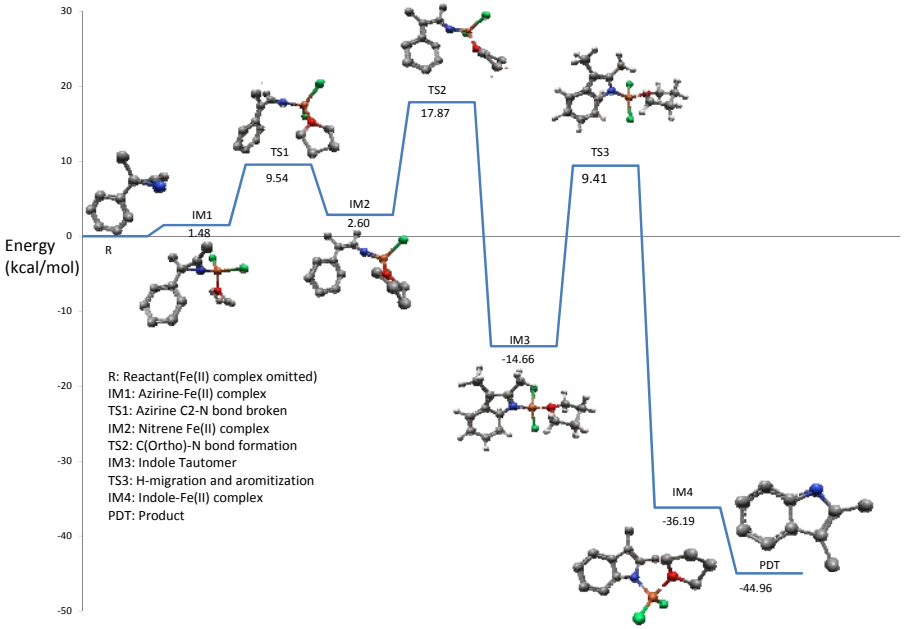

Hydrogen as substituent on C2:

When hydrogen is the substituent on C2 of the azirine ring, experiment shows that the rearrangement doesn't occur in the time allowed for the reaction. This is most likely due to the conjugation shown in the azirine ring system with hydrogen in the system, as the carbon-carbon bond in the azirine shows some double bond character. The azirine reactant with hydrogen as a substituent is more stable relative to the intermediates and transition states, raising energy barriers and thus increasing reaction time.

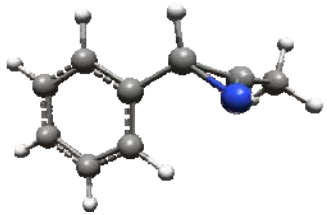

Findings:

Initially, the 2H-azirine displaces a THF from $Fe(THF)_2Cl_2$, a process that is endothermic by 1.48 kcal/mol. In the next step, the unusually long bond between the azirine C2 and nitrogen is cleaved to form a vinyl nitrene complex. From the nitrene complex, a non-aromatic indole tautomer is formed when the bond distance of the N-C(ortho) bond shortens. The next step involves the migration of hydrogen from the ortho carbon to the nitrogen, a process resulting in aromatization and a weakening of the nitrogen iron bond. The $FeTHF(Cl)_2$ is then expelled, resulting in the indole product. The substitution of hydrogen with the methyl group on C2 results in a relatively more stable reactant, which increases energy barriers and reaction time.

Acknowledgements:

We thank the Pulay group, the University of Arkansas REU program, Dr. Nan Zheng, and NSF-REU CHE-0861505.

Progress Toward Mono-Functionalized Water-Soluble Nanoparticles

Anna Fielder, Brandon Kelly, Kwangyul Moon, Daniel B. Eddings, Thomas Broja and Robert E. Gawley

Department of Chemistry and Biochemistry, University of Arkansas, Fayetteville, AR, 72701

E-Mail: afielder@uark.edu, bgawley@uark.edu

Project Goals

1. Synthesize, characterize, and optimize appropriately functionalized dendrons for ligation to quantum dots (QD's).

2. Explore solid-phase synthesis strategies to prepare quantum dots that are covalently attached to polymer resins. Derivatize the quantum dots for water solubility using methoxypoyethyleneglycol-capped dendrimers.

3. Functionalize the monovalent QDs for protein conjugation via four linkers that will provide maximum potential in a wide variety of protein applications: nitrilotriacetic acid (NTA), *N*-hydroxysuccinimide (NHS), maleimide, and acyl hydrazide. Conjugate the d-dots with representative proteins, purify, and characterize chemically and spectroscopically.

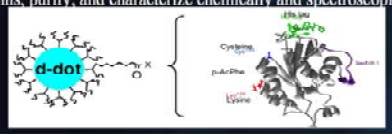

Goals for REU

1. Synthesize third generation target ligand for attachment to nanoparticle.

2. Improve the water-solubility of nanoparticles by reacting the terminal alkynes of the ligands with PEG chains via click chemistry.

Strategy for Goal #1

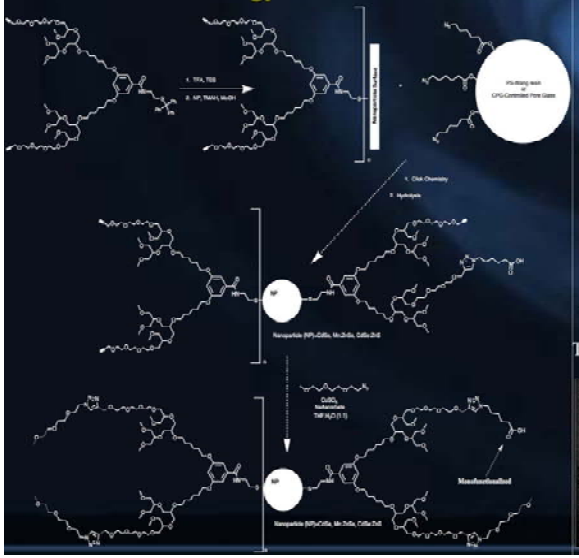

Synthetic Scheme - Ligand Synthesis and Click Chemistry

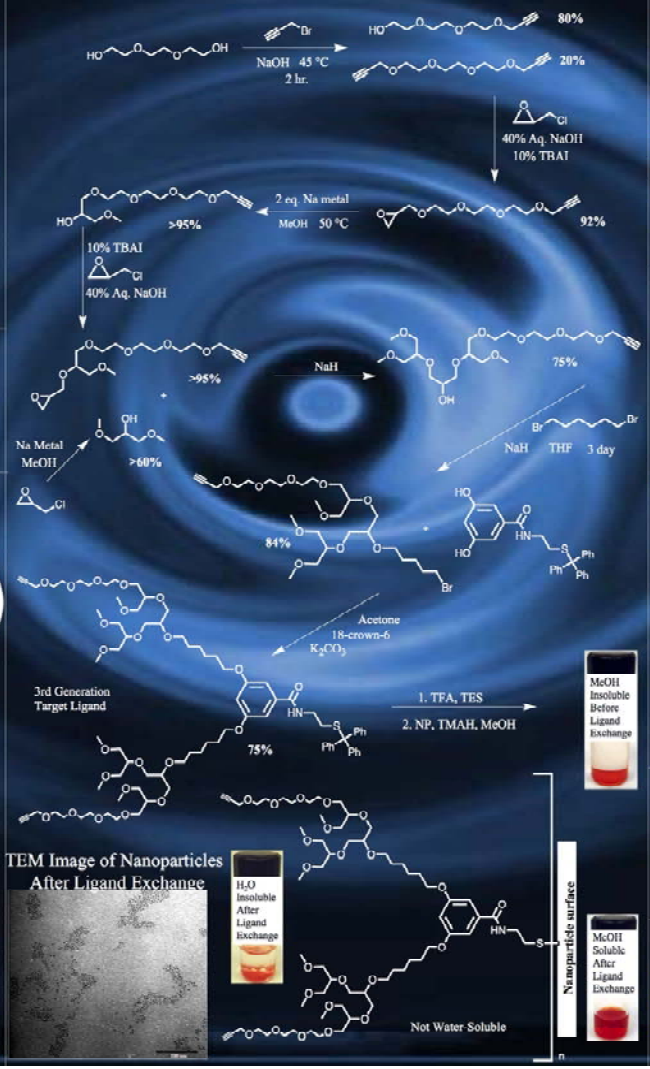

Improvement of Water-Solubility

In order to improve water solubility in the final target, additions of PEG chains to the terminal alkynes via click chemistry is desired.

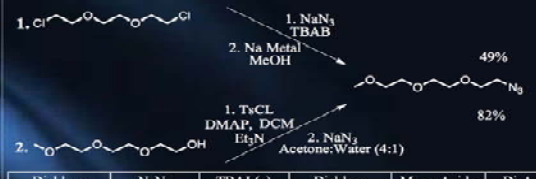

Dichloro	NaN_3	TBAI (g)	Dichloro	Mono-Azide	Di-Azide
3	1	0.003	78%	22%	0%

Due to greater yield, availability of starting material, and lack of bi-product, such as the diazide, reaction 2 proved to be more efficient in synthesizing the mono-azide compound necessary to improve water solubility.

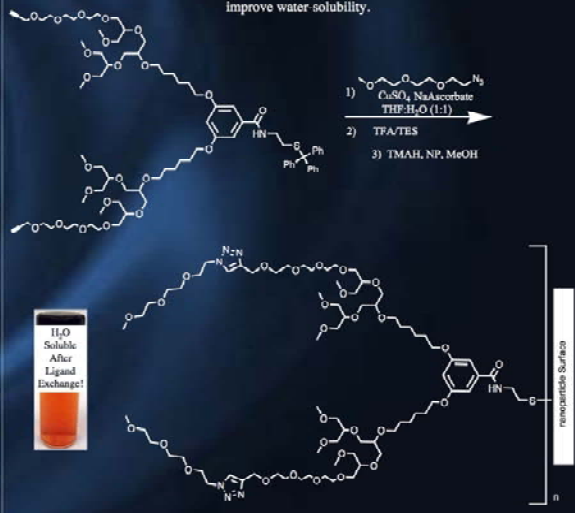

Future Work

1. Attach QDs to solid support through "Click" cycloaddition

2. Add PEG azide to remaining alkynes

3. Cleave from bead and attach to protein

Acknowledgements

National Science Foundation (CHE-0851505/REU)
National Institutes of Health (EB999802 and RR15569)
Arkansas Biosciences Institute

Methods towards thiazolium salt rearrangements

Rebecca Foos, Silvana Dormi, Matt McIntosh*

University of Arkansas, NSF REU

Abstract: Much of research within organic chemistry surrounds the methods of pharmaceutical development. The compound thiazole is considered to be a favored structure in many drugs, and as such methods by which it may be used synthetically are of great interest. This study develops the chemical rearrangement of an n-allyl substituted thiazole to a terminal alkylene chain at the beta carbon. Although the study is ongoing, successful rearrangement has been observed with yields up to 38%.

Thiazole is known as a "privileged" structure in the chemi-pharmaceutical world due to its heavy use in drug syntheses. Fig. 1 shows several such drugs. Of course any molecule of this size takes many synthetic steps to produce. For this reason, the synthetic rearrangement developed in this study is of great practical value in the field of pharmaceutical development.

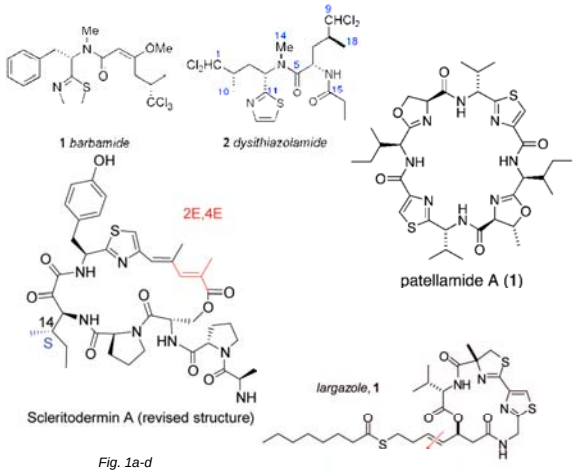

Fig. 1a-d

A close predecessor to this rearrangement is found in the Kurth reaction of the 1980s, which saw the same rearrangement with an oxygen replacing the sulfur. However, this reaction was not intended for pharmaceutical application, but instead served as a method towards enantiomerically selective production of a carboxylic acid.

The first step in the rearrangement synthesis is the formation of the base salt (see Fig. 2). By heating thiazole with an allylic electrophile – we used tosylate – for up to five hours, followed by purification via trituration in ether, yields of up to 86% were reached.

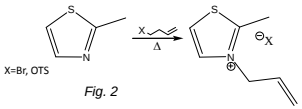

Fig. 2

Following the salt formation, activation by base at the beta carbon by sodium hydride gives the ketene acetal intermediate.

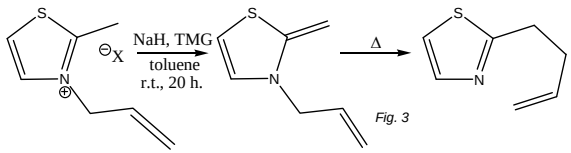

Fig. 3

This process, without the interference of an allyl group, has been previously developed; however, there is a known side product which must be avoided. Fig. 4 shows the process known as dimerization, which gives an observed side product within the intended synthesis, a dimer of the original salt.

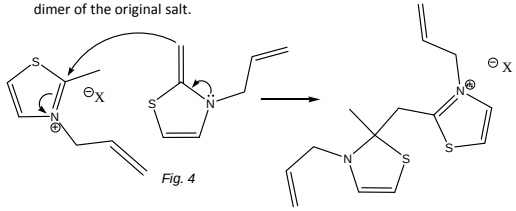

Fig. 4

The side reaction may be avoided via very high dilution of the reaction mixture, with essentially serves to isolate the formed ketene acetal from the unreacted salt.

This may be achieved in two ways:

1) by adding the salt in solution very slowly by syringe pump to a hot reaction mixture, which will presumably allow the ketene acetal to immediately rearrange upon formation, with low enough concentration that it will not kinetically be able to react with any unreacted salt

2) by using a solvent in which the salt is insoluble, thereby limiting the presence of salt with ketene acetal in solution by the innate solubility of the salt. This second process also allows for complete reduction to the ketene acetal and subsequent heating to drive the rearrangement in a two step process, giving a bit more control and observability.

Via the second method, the procedure for the total rearrangement becomes rather straightforward. The salt is placed in toluene in a pressure tube to prevent the toluene from boiling off during heating. Sodium hydride and tetramethyl guanidine (TMG), a base facilitating the proton transfer, are added to the solution and the ketene acetal is formed at room temperature over a period of 20 hours.

At twenty hours, the reaction is placed in an oil bath and heated to 150 C for 2 hours.

Purification via extraction in ether and column chromatography gives the final pure rearrangement product, verified by Nuclear Magnetic Resonance (NMR) Spectroscopy (see Fig. 5)

Fig. 5

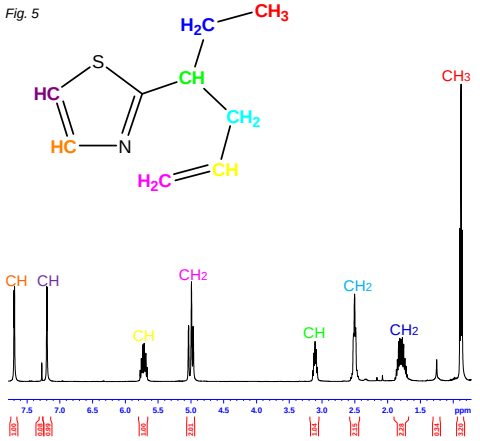

The clean spectra detailed above shows the purity of the rearrangement product at above 90%. This particular reaction gave a yield of 38%, which in the initial stages of development is rather high.

Further study will include labeling of the terminal rearrangement carbon via a methyl group to check positively that the mechanism is indeed a rearrangement and not simply a electrophile/nucleophile intramolecular reaction.

I would like to thank Dr. McIntosh for his support and guidance, and for making room for me in his busy lab. I would also very much like to thank Silvana Dormi, my "director of operations," as she brought me into this project and worked alongside me to realize this rearrangement.

My thanks also to the University of Arkansas, the National Science Foundation NSF-REU CHE-0861505, NSF CHE-0911638, the National Institute of Health NIH RR-1569, and the Arkansas Biosciences Institute.

NSF

UNIVERSITY OF ARKANSAS

Fluid Motion with Magnetohydrodynamics

Amanda Hicks, Melissa Weston, Joe Bruton, and Ingrid Fritsch
Department of Chemistry and Biochemistry, University of Arkansas, Fayetteville, AR 72701

Background and Introduction

F_B= j X **B** defines the magnetohydrodynamic (MHD) force, which is related to the Lorentz force.

$$\overrightarrow{F_B} = \vec{j} \times \vec{B}$$

Potential applications include microfluidics, or lab on a chip type applications. The MHD force is capable of moving fluid without the use of moving parts, and could be used for pumping, mixing, or stirring within a small, enclosed environment.

Purpose

•To understand the way the magnetohydrodynamic force moves fluid containing a redox species in a small volume using a magnetic field parallel to the chip rather than a perpendicular one as has been done in the past.
•To learn the different factors that affect the velocity of the beads.
•To find out whether the fluid goes around the sides of the electrodes or up and over them to replace the fluid that is moving away.

Methods

•A solution of 0.07 M potassium ferricyanide, 0.07 M potassium ferrocyanide, and 0.1 M potassium chloride, with a 50X dilution of 10 µm polystyrene beads in deionized water was prepared.
•Polydimethylsiloxane (PDMS) gaskets placed on the chip were used to determine the depth of the cell (the cell being the electroactive solution surrounding the electrodes.)

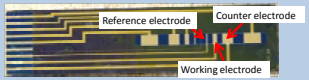

The chip used, with a symmetrical arrangement of electrodes

•Chronopotentiometry was used to control the current within the cell, using a gold working, reference, and counter electrode of 800 µm, 200 µm, and 2000 µm respectively.

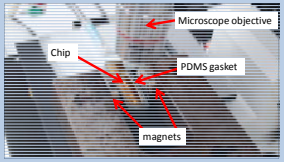

Photo of chip setup on microscope stage showing chip, PDMS, and parallel magnet setup using two 0.5 T NdFeB permanent magnets.

Cross section of setup to show electrode positions within the magnetic field. The working electrode was always kept as close to the center of the magnetic field as possible. (Not to scale)

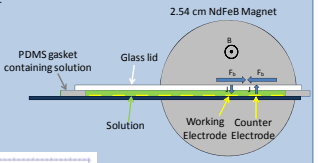

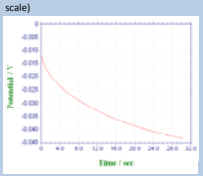

Plot of potential over time when a constant current is maintained at the electrode.
All experiments, except for those that varied current, were done at a cathodic current of 30 µA, which is below the diffusion limited current. This was done to avoid damaging the electrodes or electrolyzing water, which would produce bubbles and hinder the flow.

Data, Results, and Interpretation

Does time matter?

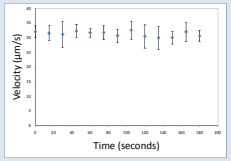

Graph of relative bead velocity over three minutes, showing velocities remaining unchanged over time.

Answer:
No. When using a controlled current, the velocity remains constant over time. This means that there is a broad window of time for measurements without changing the results, until the ions in solution are exhausted.

Does it match the theory?

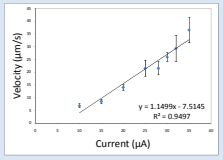

Graph of bead velocity at different currents showing a linear trend consistent with the movement within the perpendicular field. It is important to note that it does not pass through zero, but the reason for that is not known at this time.

F_B= j X **B**
j, ion flux, is related to **i**, which is applied current.
Therefore, higher currents should lead to higher velocities.

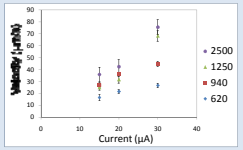

Different currents at different PDMS depths continue to follow a linear trend, proving that the relationship holds.

Answer:
Yes. The relationship between current and bead velocity is linear, following the relationship of **j** being represented by **i**.

What is the overall pattern of the fluid flow?

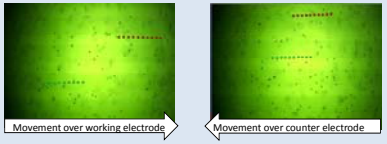

Top down view of flow between working and counter electrodes showing the reversal of the fluid direction between the electrodes

Answer:
The fluid moves in opposite directions over the working and counter electrodes, forming four circulations across and around the electrodes instead of going up and over. The right hand rule predicts this if edge effects are ignored. Moving counter electrodes does not affect patterns.

Vertical position and PDMS depth

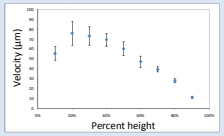

Relative bead velocity vs % height in the cell showing a maximum velocity around 25%, where it is closer to the electrode providing the force.

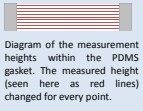
Diagram of the measurement heights within the PDMS gasket. The measured height (seen here as red lines) changed for every point.

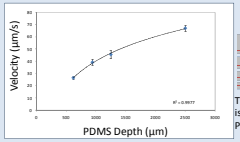

Relative bead velocity vs PDMS depth at a single height showing the trend becoming less steep as the height increases because the no-slip boundary at the ceiling moves away and therefore resistance to fluid flow diminishes

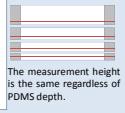
The measurement height is the same regardless of PDMS depth.

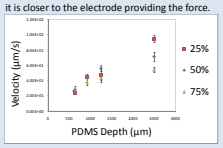

Bead velocity vs PDMS depth at varying heights showing that the curved trend does not change based on the measurement height.

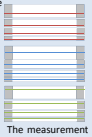
The measurement height is a percentage of total depth.

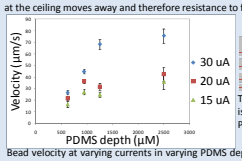

Bead velocity at varying currents in varying PDMS depths showing that the curved trend does not change based on differing currents.

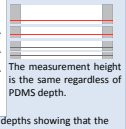
The measurement height is the same regardless of PDMS depth.

Result:
The velocity changes both as a function of the vertical location in the cell, and the depth of the cell. This is consistent with studies done in the perpendicular magnetic field.

Conclusions

• The velocity of the beads does not change over time.
•There is a linear relationship between current and velocity, proving that ion flux (**j**) is related to current (**i**).
•The solution goes around the electrodes instead of up and back over the top. The four circulations are attractive for mixing on a small scale.
•The velocity of the beads varies through the height of the solution, reaching a peak at around 25%.
•Deeper cells have higher velocities because the no slip boundaries at the walls are further away, so resistance to flow is lessened.
•These results add to the fluid manipulation toolkit that MHD has to offer.

Acknowledgements

We thank the Fritsch research group, Vishal Sahore for chip fabrication, and the National Science Foundation for financial support through grant CHE-0719097 and NSF/REU CHE-0861505.

Configuration and Geometry of the RWALP15 Transmembrane Peptide in a Lipid Bilayer

Jared O. Kafader, Nicholas Gleason, and Roger E. Koeppe II

Department of Chemistry and Biochemistry, University of Arkansas, Fayetteville, AR, 72701

Abstract

Membrane proteins along with their fundamental peptide-lipid interactions are some of the least understood areas of biochemistry. To answer some of these questions, RWALP15, a short model transmembrane peptide, was synthesized with isotopically labeled residues through solid-phase peptide synthesis and analyzed with ^{2}H solid-state NMR in various lipid membrane environments such as DLPC (C12:0), DMPC (C14:0), and DOPC (C18:1Δ9c). The Geometric Analysis of Labeled Alanines (GALA) method was used to determine the orientation of RWALP15 in each lipid bilayer. Synthesis confirmation of RWALP15 was determined through MALDI-TOF mass spectrometry and peptide purification was performed by HPLC. The results procured from the NMR tests state that the RWALP15 peptide does in fact have a defined orientation in each of the DLPC, DMPC, and DOPC lipid bilayers. It has been observed that the RWALP15 peptide does contain an α-helix structure in each lipid system, though immensely diminished in DOPC. Fluorescence data suggests that the anchoring tryptophans in all DMPC, DLPC, and DOPC lipids are located around the lipid/water interface. The observed quadrupolar splittings from ^{2}H NMR along with the GALA analysis indicate the tilt of RWALP15 to be ~7° in DLPC and DMPC bilayers. It is surprising to observe a transmembrane orientation of the RWALP15 peptide in DMPC considering its hydrophobic length to be significantly shorter than the bilayer thickness.

RWALP15 Model
Ac-GRWLALALALALWRA-amide

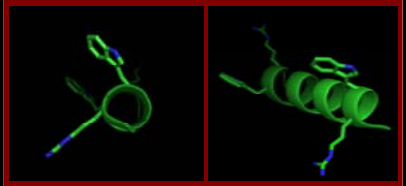

with underlined residue being deuterated

Labeling

Each peptide synthesized had two corresponding deuterium labels, with one label being 50% and the other 100%. With deuterium labels are at these specific ratios, it is generally possible to match the labels with their corresponding intensities.

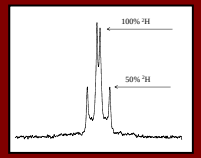

NMR Sample Preparation

A lipid/peptide mixture was mixed and then put under a vacuum line for 48 hours (a). The peptide/lipid mixture was then placed evenly on 40 glass slides (b). The glass plates were hydrated, placed in a cuvette, and sealed (c). The cuvette was then heated at 40° C in a dark area for at least 48 hours (d). The sample, once aligned in the bilayer, was run at both the β = 90° position (parallel position) and the β = 0° position (perpendicular position).

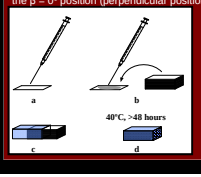

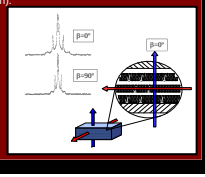

Mass Spectrometry

Mass spectrometry confirmed that the peptide produced during the solid-phase peptide synthesis was in fact the RWALP15 peptide plus the mass of the deuterium labels.

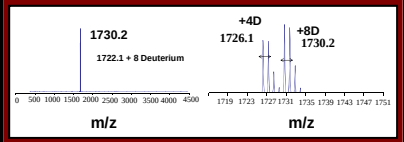

HPLC

The HPLC results confirmed that RWALP15 was present in large quantities, but was further purified to remove impurities.

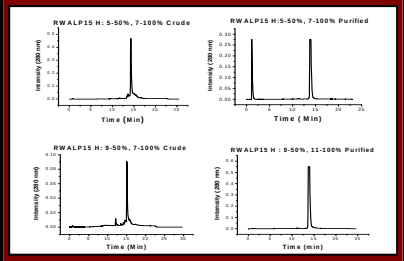

Circular Dichroism and Fluorescence

The CD results illustrated that RWALP15 resides in a α-helix configuration in all lipids. But a much smaller amount of helical character exists in DOPC, the longest of the lipids.

The fluorescence data indicates that Trp residues in RWALP15 are likely found at the membrane interfacial region in all DLPC, DMPC, and DOPC bilayers. This suggests a transmembrane orientation, but would require confirmation.

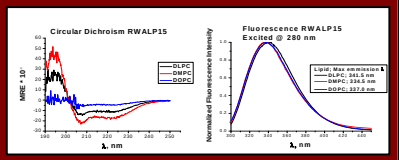

^{31}P NMR

All oriented samples were first analyzed with ^{31}P NMR to ensure a well oriented bilayer before running 2H NMR experiments. At β = 0° an aligned sample should have a single peak around 25 ppm and at β = 90° the aligned sample should have a peak around -25 ppm.

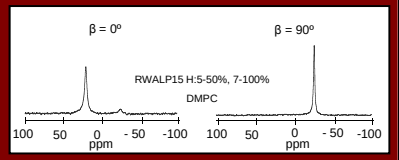

^{2}H Solid-State NMR

RWALP15 was placed in the lipids DLPC, DMPC, and DOPC, which have a hydrophobic thickness of 19.5, 23, and 27 Å respectively. Distinct splittings were seen in every DLPC, DMPC, and DOPC, implying that RWALP15 has defined orientations in all lipids. Side chain hydrogens are represented by strong peaks, with backbone hydrogens visible as well.

Ala - 5 - 50% **Ala - 7 - 100%**

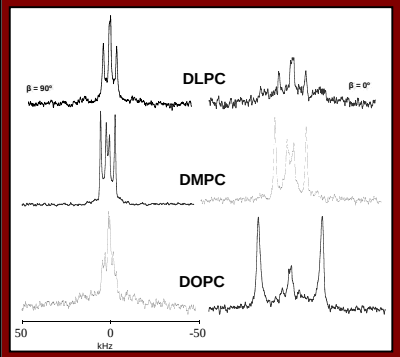

Ala - 9 - 50% **Ala - 11 - 100%**

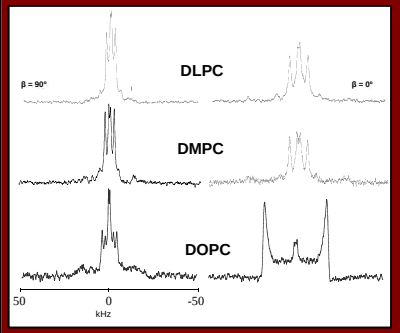

^{2}H Solid-State NMR Splittings

Lipid	DLPC			DMPC			DOPC		
Ala-C_β	β=0°	β=90°	*Average*	β=0°	β=90°	*Average*	β=0°	β=90°	*Average*
5 (50%)	1.9	0.7	1.7	3.8	1.9	3.8			
7 (100%)	16.3	8.1	16.3	17.3	8.4	17.1	Unable to assign		
9 (50%)	1.3	0.6	1.3	2.1	0.9	2.0			
11(100%)	10.5	5.1	10.3	10.1	5.0	10.1			

* All splittings in kHz (β=0° and twice the β=90° splittings were used to determine the "Average")

^{2}H NMR and GALA Theory

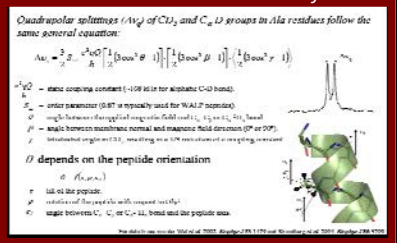

GALA Analysis

The experimental data (shown with dots) was collected through ^{2}H solid-state NMR and best fit according to the $\Delta\nu_Q$ equation. A best fit curve is shown with the solid line.

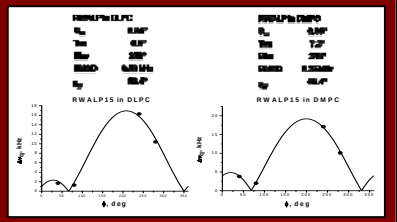

Future Plans

- Shorten the hydrophobic core of the RWALP15 peptide. A leucine and/or alanine would be removed to produce RWALP13 in order to determine if the sequence is short enough to not span the lipid bilayer.
- Removal of arginine residues in RWALP15 leaving only the tryptophan as anchors.
- Antimicrobial assay tests can be performed on these peptides to observe if they possess any antimicrobial activity.

Conclusions

- RWALP15 in DLPC, DMPC, and DOPC has defined orientations in or on the respective lipid bilayer.
- There is a decrease in α-helical content for RWALP15 in DLPC and DOPC lipids.
- It is unusual that fluorescence data for DOPC to have data points between those of DLPC and DMPC when DOPC has the thickest membrane.
- ^{2}H solid state NMR splitting have been obtained in DOPC, establishing the speculation that RWALP15 might be transmembrane in this specific lipid.

References and Acknowledgements

[redacted]

Acknowledgements

Vitaly Vostrikov
Johanna M. Froyd-Rankenberg
Dr. Denise V. Greathouse

Funding

NSF

Degradation of GDP to form Apo Cdc42 wt.

Erika Russell[1,2], Paul Adams[2]

1. Bethune-Cookman University , Chemistry Department

2. Department of Chemistry and Biochemistry, University of Arkansas

Abstract:

The goal of the summer research project was to examine possible new ways to liberate GDP from the protein of interest Cdc42Hs. With apo-Cdc42Hs, there will be a better understanding of the structure of Cdc42Hs which could potentially reveal insights on GDP dissociations and how this leads to cell proliferation.

Introduction:

Cdc42 wt has 178 amino acids and is one of the first identified human oncogenic proteins—mutants of Cdc42 wt account for nearly 30% of all cancer cells[3] . The Ras family is a group of related proteins that are involved in cellular signal transduction. As a member of the Ras family of GTP-binding proteins Cdc42 wt aids in cellular transformation and cell growth via increased rates of GTP to GDP cycling[5]. When Cdc42 wt is bound to GTP it is active and will remain in this state until a GTP-ase activating protein causes it to hydrolyze the phosphate group body to an inactive GDP state. To return to the active state Guanine nucleotide exchange factors (GEFs) catalyze the exchange for bound GDP to GTP. This is significant because a regulatory protein, dbl, has the ability to stimulate the exchange for GDP to GTP in Cdc42 wt either by increasing the rate of cycling between GTP and GDP, or by a deficiency in GTPase activity which can lead to cell proliferation and transformation. Additionally, Cdc42 wt has a high affinity for dbl when it is in a nucleotide free state—thus the goal of the summer research project is determine new ways to liberate GDP from Cdc42 wt in order to begin to study the molecular details of this form of the protein. One of the new approaches included the potential exploitation of a chromatographic matrix with an affinity for proteins with a well-defined nucleotide binding site.

Figure 1: Cdc42Hs-GDP[4]

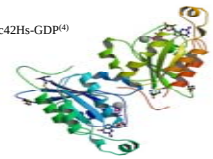

Materials and Methods:

Two different experiments were attempted to try to accomplish the same goal, the generation of apo-Cdc42Hs. A flow chart diagram of what we wanted to accomplish can be seen below.

I. Experiment 1

A. Control Experiment

1. Control protein Pyruvate Kinase + Cibracon Sepharose

↓ Pyruvate Kinase-Cibracon Sepharose

↓ NaCl + 30mM Tris-HCl Buffer + Pyruvate Kinase

↓ Pyruvate Kinase off of column (Figure 1)

B. Experiment

1. Cdc42Hs → Purify (Ni affinity column)

↓ Urea (to unfold) + Buffer (6M urea, 20mM Tris, pH 7.5, 25° C, 100mM NaCl, 10mM Na_2EDTA)

↓ Dialyze

↓ GDP + Unfolded Cdc42Hs

↓ Refold Cdc42Hs

↓ Apo-Cdc42Hs

↓ Cibracon-Sepharose

II. Experiment

A. Control

1. Mant-GDP +Buffer (64mM Tris-HCl, pH 7.6, 1mM EDTA, .5mM DTE, 1mM NaN_3)

↓ Dry Alkaline Phospatase Beads + Mant-GDP-Buffer

↓ Fluorescence

B. Experiment

1. GDP-Cdc42Hs → Purify

↓ Pure GDP-Cdc42Hs

↓ GTP + Buffer(32mM Tris-HCl, 200mM $(NH_4)_2SO_4$ .5mM NaN_3, pH 8) + Alkaline Phosphatase

↓ GTP-Cdc42Hs + guanosine

↓ Phosphodierterase

↓ Cdc42Hs

↓ Cibracon-Sepharose

In Experiment 1, the goal was to unfold Cdc42Hs using a buffer containing Urea, and to refold without GDP. To begin parameters were established using a control proteins Pyruvate Kinase and a Cibracon-Sepharose Column. The protein was selected because it possesses a dinucleotide fold and because of this it should bind well to the Cibracon blue dye. This is believed because Cibracon Blue dye is covalently attached to the Sepharose matrix, and can be used to have a greater affinity for the binding sites of proteins with a dinucleotide fold like Pyruvate Kinase and Glutamine Synthetase. This is important to try because if it works then we can also try to bind Cdc42 wt to exploit potential binding affinity of Cibracon Blue.

In Experiment 2, to create apo-Cdc42Hs. GDP was exchanged for GMPPCP. Alkaline Phosphatase reduced GDP to guanosine, (which can be monitored on the FPLC) and after a full GDP-GMPPCP exchange is believed to have occurred phosphodiesterase will be added to degrade GMPPCP and leaving Cdc42Hs nucleotide free. Subsequently, Cdc42Hs can then be added to the Cibracon-Sepharose column.

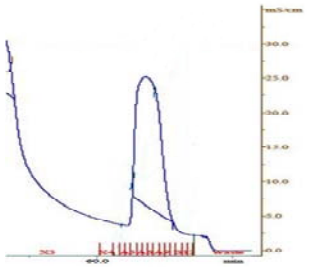

Figure 2: Chromatograph of purified Cdc42Hs wt.

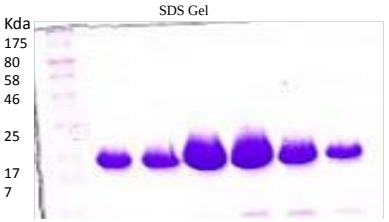

Figure 3: Gel electrophoresis confirmed pure Cdc42 wt. The samples were collected from the fractions that correspond to the peak in figure 2.

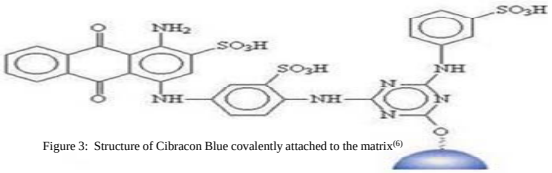

Figure 3: Structure of Cibracon Blue covalently attached to the matrix[6]

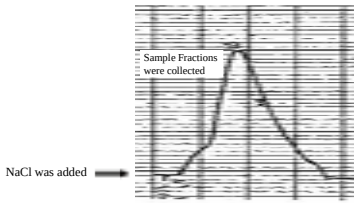

Figure 4: Chromatograph of Pyruvate Kinase from Cibracon Sepharose column Sample fractions were collected and tested using gel electrophoresis, however we did not see any bands at 25Kda (molecular weight of pyruvate kinase) so we could not confirm that this is the protein, however, some experimental error could be involved.

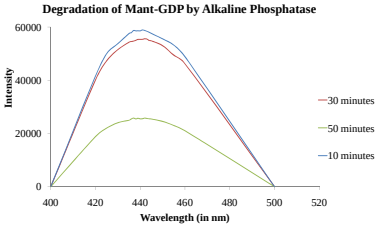

Figure 6 (right): Alkaline Phosphatase was added to Mant-GDP buffer. The reaction was observed over 2 hour period of time—taking readings (200µM of Mant-GDP buffer and 800µM buffer) every 20 minutes using the fluorometer. The intensity decreases as GDP is degraded by Alkaline Phosphatase.

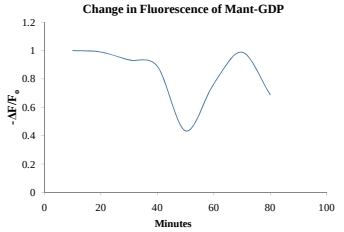

Figure 7 (left) is a continuation of figure 6. Here ΔF is the change in fluorescence relative to the initial fluorescence, where the initial value is the 10 minute reading and the final value is the 80 minute reading.

Conclusion:

In Figure 6, for the first 50 minutes the intensity steadily decreases starting at 60,000 and dropping to 25,000—after 50 minutes the intensity fluctuates indicating that GDP was completely degraded after about 50 minutes . However, we were unable to repeat experiments to establish a trend in the potential noise after 50 minutes or if another excited state process was being exploited from an emission stand point. From this information there is reason to believe that because Alkaline Phosphatase degrades the fluorescent analogue of GDP then it should also degrade bound GDP in Cdc42Hs.

Acknowledgements & References

Funding provided by NSF-REU CHE0861505 and NIH-5K01CA113753 to P.D.A.

3. Bos, J.L Ras Oncogenes in Human Cancer. *Cancer Res.* 1989, 49, 4682-468

4. Demerdash O.N.A; Daily M.D; Mitchell J.C *PLoS Computational Biology* 2009, 5(10):e1000531ff

5. Zhang J.; Matthews R. C. Ligand Binding Is the Principal Determinant of Stability for the p21H-ras Protein. *Biochem.* 1998, *37*, 14881-14890.

6. Lowe, C.R.; Pearson, J.C. Affinity Chromatography on immobilized dyes. *Methods Enzymol* 1984,104, 97–113.

A Kinetic Study of Cytochrome c and Cytochrome c Oxidase

Maria Willaims Texas Southern University, Houston, Texas
Dr. Lois Geren, Marilyn Davis , Dr. Francis Millett, & Dr. Jeffrey Havens, University of Arkansas, Fayetteville

Introduction

Electron-transfer reactions play an essential role in a biological processes such as mitochondrial respiration. Cytochrome c and cytochrome c oxidase are two major components of the electron transport system.

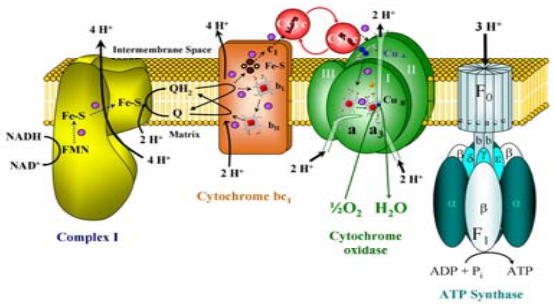

The basis of my experiment is to study the reaction of cytochrome c with cytochrome oxidase using site-directed mutagenesis and steady-state kinetics. The goal was to characterize the electrostatic interaction between cytochrome c and cytochrome oxidase. The mutants that were expressed in this project were E89T/E90K and E89T/E90Q. These mutants replace the native negative charge on glutamic acid 90 [E90] of with a neutral charge, glutamine [Q], or a positive charge, lysine [K]. By gathering data from the kinetic experiments, we will be able to determine if the mutations had an effect on the reaction between cytochrome c and cytochrome c oxidase. Steady-state kinetics reactions generally display saturation kinetics at sufficiently high cytochrome c concentrations and often obey Michaelis-Menten kinetics with a Michaelis constant, K_m, and a maximum velocity, V_{max}.

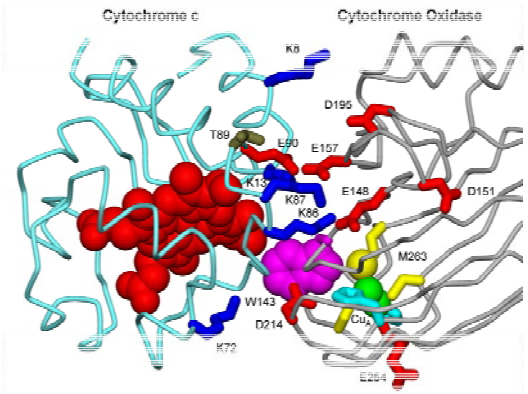

Experimental Procedures

The mutants that were used in the experiment are labeled as E89T/E90Q and E89T/E90K. The mutants were expressed in XL21BE3 native E.coli cells using plasmid DNA strands with the selected mutations which will grow and express. The mutants were expressed in rich broth for a forty-eight hour period and were spun down in the centrifuge to get the protein into solution. Once all of the rich broth is gone the cells were lysed and the protein purified. The purification process included ammonium sulfate precepitation, size exclusion chromatography, and high pressure liquid chromatography (HPLC) using a cation exchange column. The protein was highly pure after the HPLC. The protein still had a high concentration of salt, so it was exchanged with 5 mM sodium phosphate pH 7, using a centrifuge concentrator. The protein was then used for the kinetic studies. The kinetics were started by measuring out .08705 grams of sodium dithionite and 5 milliliters of water to make .1M of solution which is made anaerobic. The stock solution of oxidase was diluted by a 1:100 ratio, so 3 uL of oxidase was diluted with 300 uL of buffer. The buffer was 5 mM PI/100 mM NaCl .01% LM pH 7 at 25 C. For each experiment, a concentration of cytochrome c was placed in 500 uL of buffer and degassed. The concentration was then measured on the degassed sample and on average 3 to 5 uL of sodium dithionite was added to the sample to fully reduce cytochrome c. The spectra was checked again to see if cytochrome c was fully reduced. Once this had happened, the top is opened to check to see if the spectra remained stable. Then the required amount of oxidase was added to the sample and the rate of oxidation of cytochrome c was measured at 550 nm in the spectrometer. This was repeated many times to obtain data for the experiment.

Results

7/15 Human Cyt C	
V_{max}= 4.76	
Concentration µM	
1.13	0.678
3.38	0.792
4.8	1.62
8.2	2.6
18.2	2.61

7/15 E89T/E90Q	
V_{max}= 2.74	
Concentration µM	Rate sec -1
3.6	0.876
8.34	1.25
10.5	1.44
14.2	1.92
22	1.81

7/15 E89T/E90K	
V_{max}= 2.04	
Concentration µM	Rate sec -1
2.2	0.831
5.4	0.894
12.3	1.62
16.4	0.918
25	1.29

7/16 Human Cyt C	
V_{max}= 3.20	
Concentration µM	Rate sec -1
1	0.756
2	2.03
3.4	1.42
5	2.39
8.7	1.3
13.4	2.01
17.9	1.52

7/16 E89T/E90K	
V_{max}= 2.48	
Concentration µM	Rate sec -1
1.33	0.7
1.9	0.576
4.9.12	1.26
9.12	1.48
12.33	2
18	1.72

7/16 E89T/E90Q	
Concentration µM	Rate sec -1
1.88	0.346
3.85	1.39
6	1.64
8.3	1.61
12.9	1.62
16.22	2

Discussion

The goal of our experiments was to determine the effect of replacing the native negative charge of the glutamic acid [E] of position 90 of cytochrome c with a neutral charge, glutamine [Q] and a positive charge lysine, [K]. The E98T/E90Q mutant expressed well and that allowed us to collect a large amount of protein for kinetic experiments. The E89T/E90K mutant did not express well but we did obtain enough for the kinetic experiments.

The reaction of cytochrome c with cytochrome oxidase obeyed first-order kinetics at all concentration of cytochrome c. The results of my experiments were that at lower cytochrome c concentration, the first-order rate constant was larger, and at higher cytochrome c concentration the rate constant became smaller. The experiments were conducted on two days consecutive days. Over the two day period we were able to gather data to plot on graphs but the 07/16 E89T/E90Q data was too scattered to plot. The objective in plotting the points is a trend line to get values for the V_{max} .

In summary, the V_{max} of both the E89T/E90Q and E89T/E90K mutants was smaller than that of wild-type cytochrome c, indicating that residue 90 plays a role in the interaction between cytochrome c and cytochrome oxidase.

Conclusion

The V_{max} for both the E89T/E90Q and E89T/E90K mutants are smaller that of the Human cytochrome c wild type. The E89T/E90Q mutant values is faster than the E89T/E90K due to faster reaction rates.

References

1. Siletsky SA, Han D, Brand S, Morgan JE, Fabian M, Geren L, Millett F, Durham B, Konstantinov AA, Gennis RB.
Biochim Biophys Acta. 2006 Sept-Oct; 1757 (9-10); 1122-32..
2. Gray, HB, Winkler, JR, Biochim. Biophys. Acta, (2010),
dio. 10.1016/j.bbabio.2010.04.441 (epub ahead of print)

Acknowledgments

NSF Research Experience for Undergraduates
Dr. David Paul, University of Arkansas, Fayetteville, Arkansas
Dr. Francis Millett, Dr. Lois Geren, Dr. Jeffrey Havens, & Marilyn Davis
Houston Louis Stokes Alliance for Minority Participants (H-LSAMP), Texas Southern University

Canoe Trip
Buffalo River, Arkansas

Meeting in Miniature

Eric Berget

Jean-Marie Charles

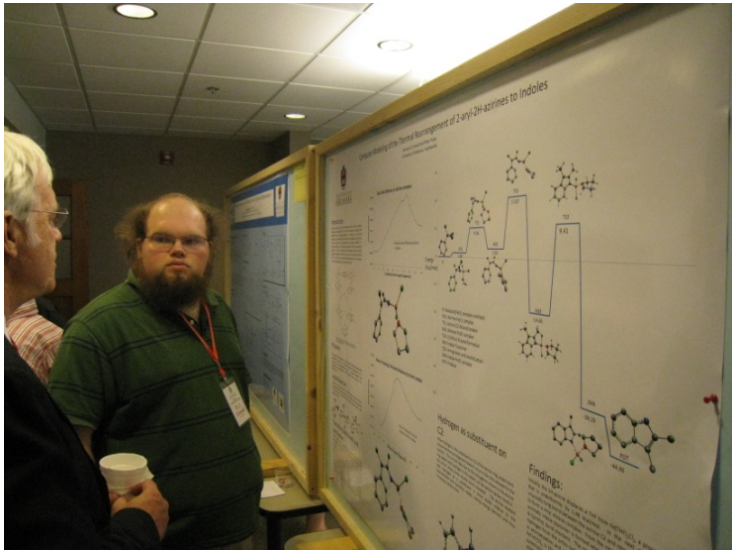

Vernon (D.J.) Crowell

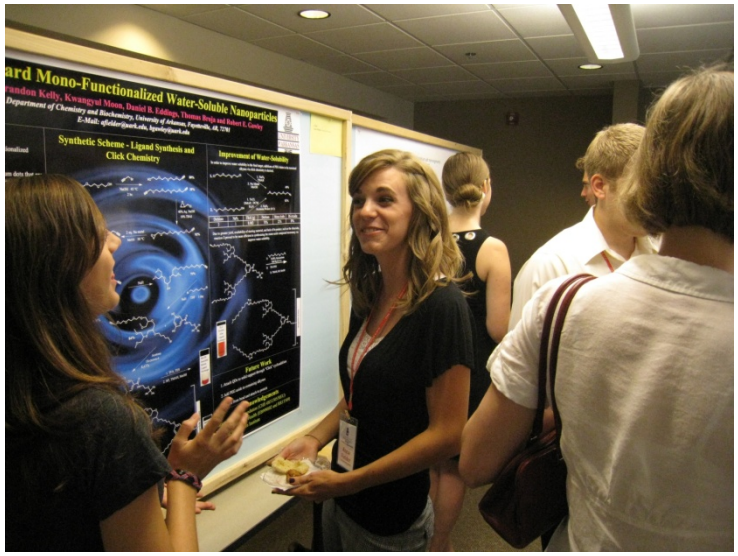

Anna Fielder

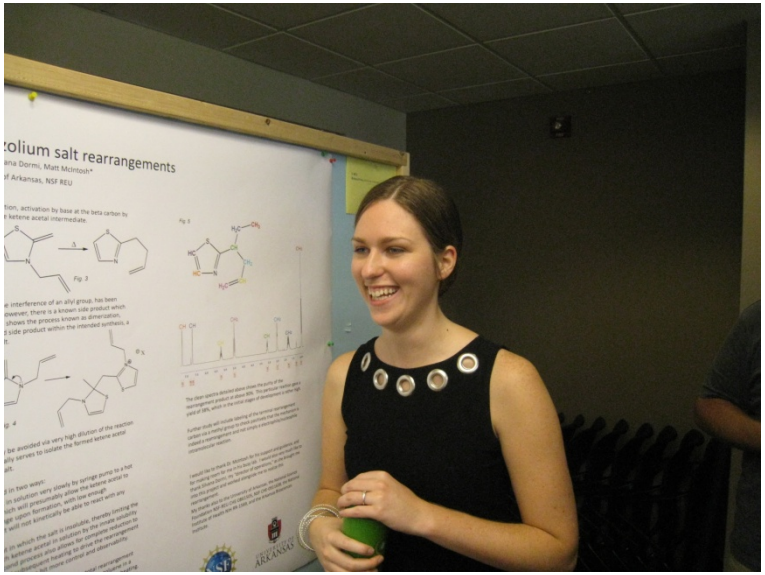

Rebecca Foos

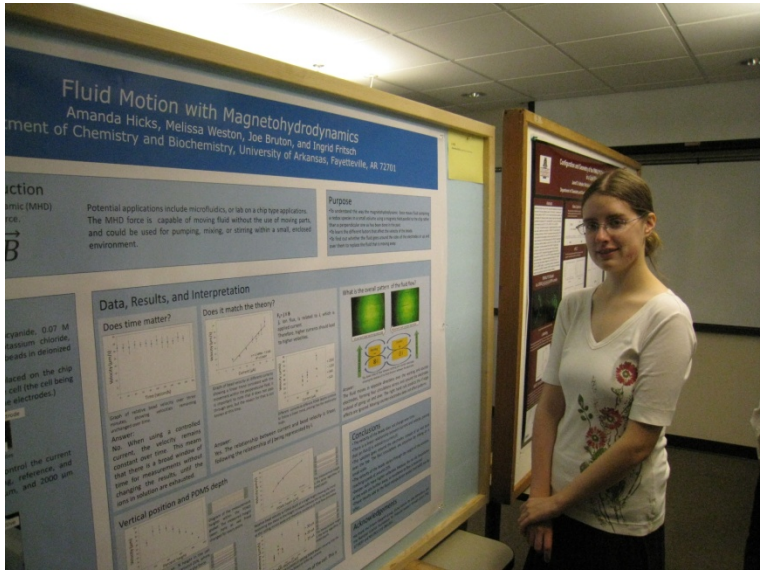

Amanda Hicks

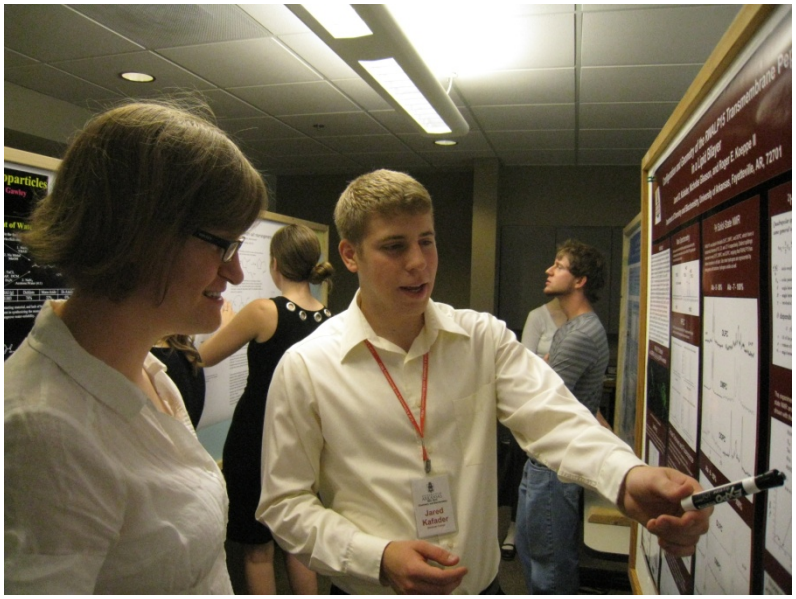

Jared Kafader

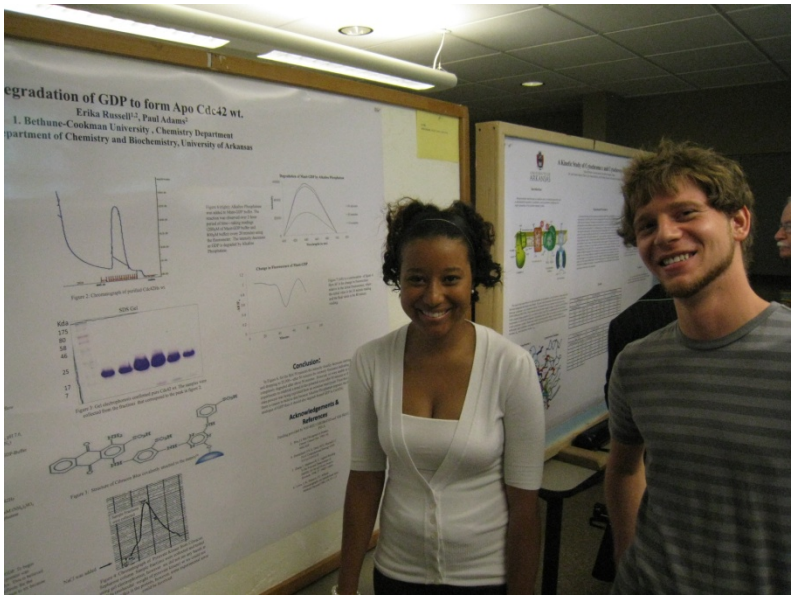

Erika Russell

Maria Williams

Jordan Bird (INBRE), Ines Pinto, Jordan Walters (INBRE)

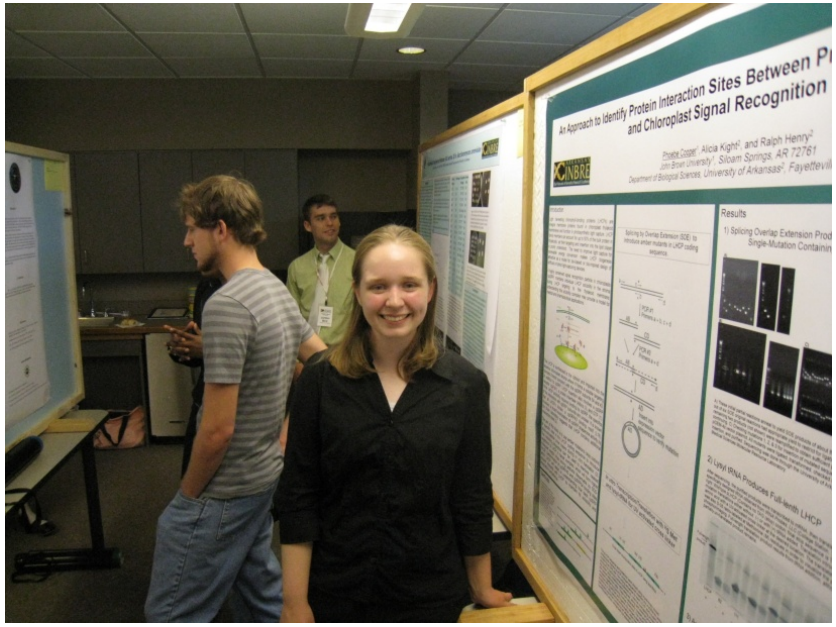

Phoebe Cooper (INBRE)

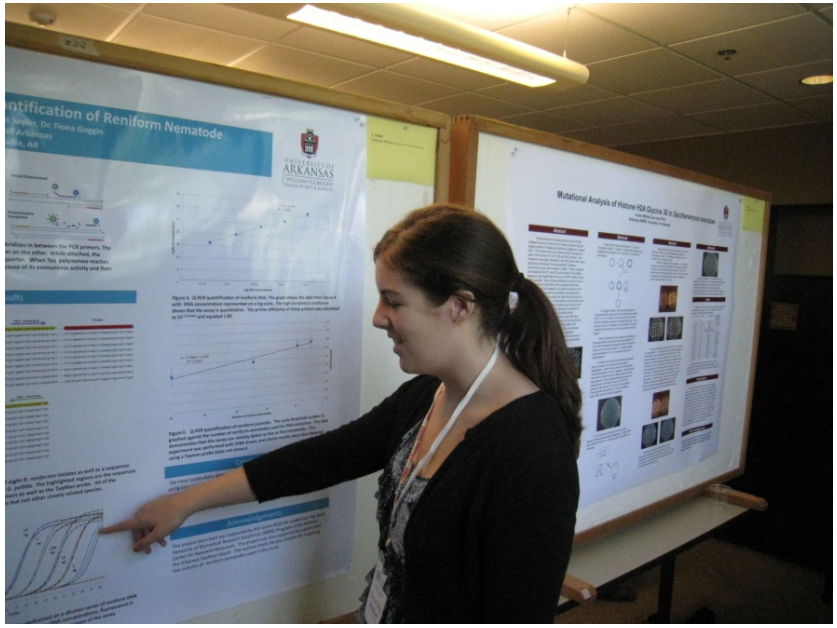

Courtney Walker (INBRE)


STATE
CHAMPIONS